

Progressive-Scale Boundary Blackbox Attack via Projective Gradient Estimation

Jiawei Zhang^{*1} Linyi Li^{*2} Huichen Li² Xiaolu Zhang³ Shuang Yang⁴ Bo Li²

Abstract

Boundary based blackbox attack has been recognized as practical and effective, given that an attacker only needs to access the final model prediction. However, the query efficiency of it is in general high especially for high dimensional image data. In this paper, we show that such efficiency highly depends on the scale at which the attack is applied, and attacking at the optimal scale significantly improves the efficiency. In particular, we propose a theoretical framework to analyze and show three key characteristics to improve the query efficiency. We prove that there exists an *optimal* scale for projective gradient estimation. Our framework also explains the satisfactory performance achieved by existing boundary blackbox attacks. Based on our theoretical framework, we propose **Progressive-Scale enabled projective Boundary Attack (PSBA)** to improve the query efficiency via progressive scaling techniques. In particular, we employ Progressive-GAN to optimize the scale of projections, which we call PSBA-PGAN. We evaluate our approach on both spatial and frequency scales. Extensive experiments on MNIST, CIFAR-10, CelebA, and ImageNet against different models including a real-world face recognition API show that PSBA-PGAN significantly outperforms existing baseline attacks in terms of query efficiency and attack success rate. We also observe relatively stable optimal scales for different models and datasets. The code is publicly available at <https://github.com/AI-secure/PSBA>.

1. Introduction

Blackbox attacks against machine learning (ML) models have raised great concerns recently given the wide application of ML (Krizhevsky et al., 2009; He et al., 2016; Vaswani et al., 2017). Among these blackbox attacks, boundary blackbox attack (Brendel et al., 2018; Chen et al., 2020) has shown to be effective. However, it usually requires a large number of queries against the target model given the high-dimensional search space. Recent research shows that it is possible to sample the queries from a lower dimensional sampling space first and project them back to the original space for gradient estimation to reduce the query complexity (Li et al., 2020a; 2021). These observations raise additional questions: *What is the “optimal” projection subspace that we can sample from? How effective such projective attack would be? What is the query complexity for such projective gradient estimation approach?* To answer these questions, in this paper we analyze the general Projective Boundary blackbox Attack framework (PBA), for which only the decision boundary information (i.e. label) is revealed, and propose Progressive-Scale enabled projective Boundary blackbox Attack (PSBA) to gradually search for the optimal sampling space, which can boost the query efficiency of PBA both theoretically and empirically.

The overall pipeline of PSBA and the corresponding analysis framework are shown in Fig. 1, where an attacker starts with a *source image* and manipulate it to be “visually close” with a *target image* while preserving its label and therefore fool a ML model via *progressive-scale* based projective gradient estimation. In particular, an attacker first conducts binary search to find a boundary point based on the source image; then samples several perturbation vectors from a low-dimensional sampling space and project them back to the *projection subspace* via a projection function f to estimate the gradient. Finally, the attacker will move along the estimated gradient direction to construct the adversarial instance. The main goal of PSBA is to search for the optimal *projection subspace* for attack efficiency and effectiveness purpose, and we explore such optimal projection subspace both theoretically and empirically.

Theoretically, we develop a *general framework* to analyze the query efficiency of gradient estimation for PBA. With the

^{*}Equal contribution ¹Zhejiang University, China (work done during remote internship at UIUC) ²UIUC, USA ³Ant Financial, China ⁴Alibaba Group US, USA. Correspondence to: Linyi Li <linyi2@illinois.edu>, Bo Li <lbo@illinois.edu>.

framework, we 1) provide the expectation and concentration bounds for cosine similarity between the estimated and true gradients based on nonlinear projection functions, while previous work only considers identical projection (Chen et al., 2020) or orthogonal sampling (Li et al., 2020a; 2021); 2) discover several key characteristics that contribute to tighter gradient estimation, including small dimensionality of the projection subspace, large projected length of the true gradient onto the projection subspace, and high sensitivity on the projected true gradient direction; 3) analyze the trade-off between small dimensionality and large projected length, and prove the existence of an optimal subspace dimensionality, i.e., an optimal scale; 4) prove that choosing a subspace with large projected length of true gradient as the projection subspace can improve the query efficiency of gradient estimation. This framework not only provides theoretical justification for existing PBAs (Brendel et al., 2018; Chen et al., 2020; Li et al., 2020a; 2021), but also enables the design of more efficient blackbox attacks, where the proposed PSBA is an example.

Inspired by our theoretical analysis, we design PSBA to progressively search for the optimal scale to perform projective gradient estimation for boundary blackbox attacks. We first consider the spatial scale (i.e., resolution of images), and apply PSBA to search over different spatial scales. We then extend PSBA to the frequency scale (i.e., threshold of low-pass filter) and spectrum scale (i.e., dimensionality of PCA). In particular, as a demonstration, we instantiate PSBA with Progressive-GAN (PGAN), and we conduct extensive experiments to 1) justify our theoretical analysis on key characteristics that contribute to tighter gradient estimation and 2) show that PSBA-PGAN *consistently and significantly* outperforms existing boundary attacks such as HSJA (Chen et al., 2020), QEBA (Li et al., 2020a), NonLinear-BA (Li et al., 2021), EA (Dong et al., 2019), and Sign-OPT (Cheng et al., 2019a) on various datasets including MNIST (LeCun et al., 1998), CIFAR-10 (Krizhevsky et al., 2009), CelebA (Liu et al., 2015), and ImageNet (Deng et al., 2009) against different models including a real-world face recognition API.

Technical Contributions. In this paper, we take the *first* step towards exploring the impacts of different projection scales of projection space in boundary blackbox attacks. We make contributions on both theoretical and empirical fronts.

- We propose the first theoretical framework to analyze boundary blackbox attacks with general projection functions. Using this framework, we derive tight expectation and concentration bounds for the cosine similarity between estimated and true gradients.
- We characterize the key characteristics and trade-offs for a good projective gradient estimator. In particular, we theoretically prove the existence of the optimal scale of the projection space.

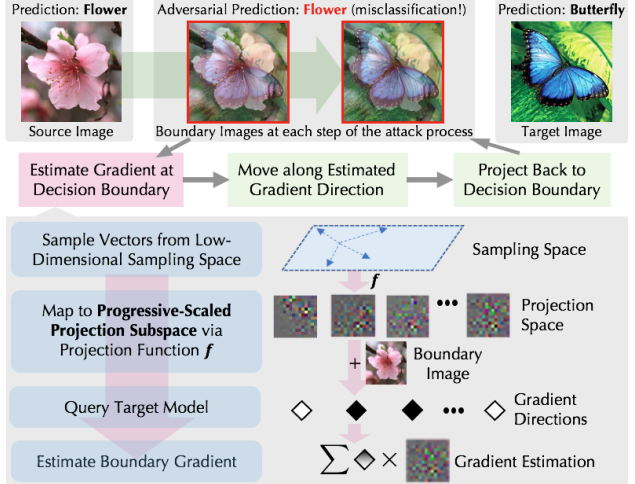


Figure 1. An overview of the progressive-scale boundary blackbox attack (PSBA) via projective gradient estimation.

- We propose Progressive-Scale based projective Boundary Attack (PSBA) via progressively searching for the optimal scale in a self-adaptive way under spatial, frequency, and spectrum scales.
- We instantiate PSBA by PGAN for empirical evaluation. Extensive experiments show that PSBA-PGAN outperforms the state-of-the-art boundary attacks on MNIST, CIFAR-10, CelebA, and ImageNet against different blackbox models and a real-world face recognition API.

Related Work. Adversarial attacks against ML have been conducted to explore the vulnerabilities of learning models and therefore improve their robustness (Szegedy et al., 2013; Kurakin et al., 2016). Most existing attacks (Goodfellow et al., 2014; Madry et al., 2018) assume the white-box setting, where the attacker has full access to the target model including its structure and weights. However, in practice, such as commercial face recognition APIs (MEGVII, 2020c), we cannot access the full model. Thus, several blackbox attacks have been proposed, which mainly fall into three categories: transfer-based, query-based, and hybrid blackbox attacks: 1) The *transfer-based attacks* usually train a surrogate model, attack the surrogate model using white-box attacks, and exploit the adversarial transferability (Papernot et al., 2016; Tramèr et al., 2017) to use the generated adversarial examples to attack the blackbox model. 2) The *query-based attacks* can be further divided into score-based and decision-based. The *score-based attacks* assume that we know the confidence score of the target model’s prediction and therefore estimate the gradient based on the prediction scores (Chen et al., 2017; Bhagoji et al., 2018; Tu et al., 2019; Ilyas et al., 2018; Cheng et al., 2019b; Chen et al., 2017; Li et al., 2020b). The *decision-based attacks* assume that we only know the final decision itself which is more practical, such as the boundary attack (Brendel et al., 2018),

EA (Dong et al., 2019) and Sign-OPT (Cheng et al., 2019a). HSJA (Chen et al., 2020) extends the boundary attack by adopting a sampling-based gradient estimation component to guide the search direction. Later on, QEBA (Li et al., 2020a) and NonLinear-BA (Li et al., 2021) are proposed to use a projection function to sample from a lower dimensional space to improve the sampling efficiency. Our work focuses on decision-based attacks. Specifically, our work systematically studies the projective gradient estimation for boundary attacks and reveals that *progressive-scale enabled projection* could improve the query efficiency both theoretically and empirically. 3) The *hybrid attacks* usually train one or multiple surrogate models and leverage the gradient information (Guo et al., 2019; Tashiro et al., 2020) or adversarial examples (Suya et al., 2020) to guide the generation of queries for the target model.

Progressive scaling has long been an effective methodology for different tasks, such as pyramidal-structured objection detection (Lin et al., 2017; Zhang et al., 2020), high-resolution generative neural networks (Karras et al., 2018; Zhang & Khoreva, 2019; Wu et al., 2020), and deep feature extraction (Cai et al., 2016; Ma et al., 2020). In this work, we aim to explore whether it is possible to progressively conduct queries from different subspaces (e.g., spatial and frequency subspaces) against a blackbox machine learning model to perform query efficient blackbox attacks.

2. Preliminaries

In this section, we introduce the related notations for our projective gradient estimation. Let $[n]$ denote the set $\{1, 2, \dots, n\}$. For arbitrary two vectors a and b , let $\langle a, b \rangle$ and $\cos\langle a, b \rangle$ denote their dot product and cosine similarity respectively. For a matrix $\mathbf{W} \in \mathbb{R}^{n \times m}$ and a vector $v \in \mathbb{R}^n$, we denote its projection on $\text{span}(\mathbf{W})$ by $\text{proj}_{\mathbf{W}} v$.¹ Without loss of generality, we focus on the adversarial attack on an image classifier $G : \mathbb{R}^n \rightarrow \mathbb{R}^C$ where C is the number of classes. For given $x \in \mathbb{R}^n$, G predicts the label with highest confidence: $\arg \max_{i \in [C]} G(x)_i$. As for the *threat model*, we consider the practical setting where only the *decision* of the classification model G is accessible for attackers.

Following the literature (Chen et al., 2020; Li et al., 2020a), we define difference function $S(\cdot)$ and sign function $\phi(\cdot)$.

Definition 1. Let label y_0 be model G 's prediction for input x^* . For the targeted attack, the adversarial target is $y' \in [C]$. Define the difference function $S_{x^*} : \mathbb{R}^n \rightarrow \mathbb{R}$ as below:

$$S_{x^*}(x) := \begin{cases} \max_{y \in [C]: y \neq y_0} G(x)_y - G(x)_{y_0}, & (\text{untargeted attack}) \\ G(x)_{y'} - \max_{y \in [C]: y \neq y'} G(x)_y. & (\text{targeted attack}) \end{cases}$$

¹From linear algebra, $\text{proj}_{\mathbf{W}} v = \mathbf{W}(\mathbf{W}^\top \mathbf{W})^{-1} \mathbf{W}^\top v$.

The function $\phi_{x^*} : \mathbb{R}^n \rightarrow \{\pm 1\}$ is the sign function of S_{x^*} :

$$\phi_{x^*}(x) := \begin{cases} +1 & \text{if } S_{x^*}(x) > 0, \\ -1 & \text{otherwise.} \end{cases}$$

When there is no ambiguity, we may abbreviate them as $S(x)$ and $\phi(x)$ respectively. For a target image x^* , the attacker crafts an image x , ensuring that the difference function $S_{x^*}(x) \geq 0$ to perform a success attack while minimizing the distance $\|x - x^*\|_2$.

We call x a *boundary point* if $S_{x^*}(x) = 0$. We assume that S_{x^*} is β_S -smooth. Formally, for any $x, z \in \mathbb{R}^n$,

$$\frac{\|\nabla S_{x^*}(x) - \nabla S_{x^*}(z)\|_2}{\|x - z\|_2} \leq \beta_S. \quad (1)$$

Note that we can only query the value of ϕ_{x^*} instead of S_{x^*} according to the threat model. In boundary attack, we estimate the gradient of S by querying ϕ .

We generalize existing gradient estimators for boundary attack in a projective form. Suppose we have a projection $\mathbf{f} : \mathbb{R}^m \rightarrow \mathbb{R}^n$, where $m \leq n$. This projection can be obtained in various ways, such as PCA (Li et al., 2020a), VAE (Li et al., 2021), or just an identical projection (Chen et al., 2020). Similar to Eq. (1), we assume \mathbf{f} is β_f -smooth². With the projection, given an input x_t that is at or close to the boundary of S_{x^*} , with pre-determined step size δ_t , we can estimate gradient $\nabla S_{x^*}(x_t)$ as such:

Definition 2 (Boundary Gradient Estimator). On $x_t \in \mathbb{R}^n$, with pre-determined step size δ_t , let $\{u_b\}_{b=1}^B$ be B vectors that are uniformly sampled from the m -dimensional unit sphere S^{m-1} . The gradient $\nabla S_{x^*}(x_t)$ is estimated by

$$\widetilde{\nabla S_{x^*, \delta_t}}(x_t) := \frac{1}{B} \sum_{b=1}^B \phi_{x^*}(x_t + \Delta \mathbf{f}(\delta_t u_b)) \Delta \mathbf{f}(\delta_t u_b), \quad (2)$$

where $\Delta \mathbf{f}(x) := \mathbf{f}(x) - \mathbf{f}(0)$. When there is no ambiguity, we may omit subscript x^* or δ_t . Note that each query of ϕ_{x^*} is a query to the blackbox model, so computing $\widetilde{\nabla S}(x_t)$ requires B queries to the blackbox model.

As previous work shows, the expected cosine similarity between the estimated and true gradients can be bounded. For example, with *identical* projection \mathbf{f} (Chen et al., 2020),

$$\cos\langle \widetilde{\nabla S}(x_t), \nabla S(x_t) \rangle \geq 1 - \frac{9\beta_S^2 \delta_t^2 n^2}{8\|\nabla S(x_t)\|_2^2}. \quad (3)$$

Definition 3 (Sampling Space and Projection Space). For the given projection $\mathbf{f} : \mathbb{R}^m \rightarrow \mathbb{R}^n$. We call the domain $\text{dom}(\mathbf{f}) = \mathbb{R}^m$ the *sampling space*, and the subspace consisting of projected images the *projection subspace*.

²For any non-differentiable point of S_{x^*} or \mathbf{f} , the assumption generalizes to any Clarke's generalized gradient (Clarke et al., 2008). For simplicity, we assume S_{x^*} and \mathbf{f} are differentiable hereinafter. The $\|\cdot\|_2$ operator stands for the ℓ_2 norm for vector ∇S and the spectral norm for Jacobian matrix $\nabla \mathbf{f}$.

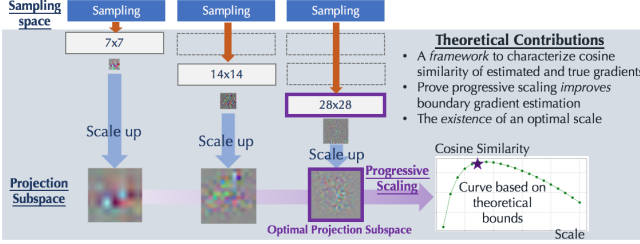


Figure 2. PSBA with progressive scaling on spatial domain.

Remark. The definition reflects the sample-and-project process in gradient estimation. The projection subspace is a subspace of the original input space \mathbb{R}^n . Typically, the step size δ_t is small, and $\Delta \mathbf{f}(\delta u) \approx \nabla \mathbf{f}(0) \cdot (\delta u)$ by linear approximation. Therefore, we can view \mathbf{f} as a non-singular linear projection where m is the dimensionality of the projection subspace.

3. Progressive-Scale Blackbox Attack: PSBA

In this section we will introduce the general pipeline of proposed **Progressive-Scale projective Boundary Attack (PSBA)**, followed by detailed analysis of it in Section 4. On the high level, PSBA progressively increases the scale of *projection subspace* where the perturbation vectors will be chosen from, until it reaches the “optimal” scale as shown in Figure 2. The scales are sampled from domains such as spatial, frequency, and spectral domain. At each scale, PSBA is composed of two stages: *training stage* and *attack stage*.

At the *training stage*, we train a generative model M (e.g., GAN), with gradient images obtained from any model. The input space of M is a low-dimensional space (m). For instance, from the spatial domain, we can sample from different resolutions such as 7×7 , 14×14 , and 28×28 . Then we leverage M to project the sampled vectors back to the original space with interpolation. These projected images form the *projection subspace*.

At the *attack stage*, we adapt the boundary attack pipeline, and first select a source image \hat{x}_0 (drawn from images from the adversarial target class). In each iteration t , the attack reduces the distance from current adversarial sample x_t to the target image x^* via three steps: (1) binary search for the boundary point x_t where $S_{x^*}(x_t) = 0$ on the line connecting \hat{x}_{t-1} and x^* , with pre-determined precision threshold θ ; (2) estimate the gradient at x_t using the boundary gradient estimator (Definition 2) with step size δ_t ; (3) normalize the estimated gradient, and perform a step of gradient ascent to get \hat{x}_t . Note that in (1), the binary search for boundary point requires $\mathcal{O}(\log 1/\theta)$ queries to the blackbox model, and in (2), the gradient estimation requires B samples and queries to the blackbox model. In Section 4 we will analyze the relation between B and the quality of estimated gradients in terms of cosine similarity.

We select the optimal scale for projection subspace based on a validation set. If with current scale, after 1,000 queries, the average distance to the target image x^* is smaller than that of the previous scale, we try a new increased scale. Otherwise, i.e., the average distance is larger than that of the previous one, we select the previous scale as the optimal scale, and use it as the scale of projection subspace. This process can be viewed as climbing to find the maximum point on the curve in Fig. 2 from left to right. Detailed pseudocode can be found in Appendix D.4.

In particular, we mainly consider different scales in the spatial, frequency, and spectrum domains. For spatial domain, M on the progressively grown scale (i.e., resolution) can be effectively trained via Progressive-GAN. The frequency scales correspond to thresholds for the low-pass frequency filter, and the spectrum scales correspond to dimensionalities of PCA. For frequency and spectrum, M can be trained on full-scale and trimmed to fit in the required lower scale as discussed in Section 4.2.

4. Analysis of Gradient Estimation

In this section, we analyze the similarity between the estimated and true gradients for general projective boundary attack frameworks. These attacks all follow Definition 2 to estimate the gradient. Our goal is to improve the gradient similarity while reducing the number of queries (B).

In Section 4.1, we present cosine similarity bounds between the estimated and true gradients for the gradient estimator with general **nonlinear projection function**, and analyze the key characteristics that improve such gradient estimation. In Section 4.2, we analyze the **bounds of cosine similarity** when the output of projection \mathbf{f} is constrained on selected projection subspace. We show how constraining on a representative subspace improves gradient estimation compared with performing gradient estimation on the original space, which explains why PSBA outperforms existing methods.

4.1. General Cosine Similarity Bounds

Let $\nabla \mathbf{f}(0) \in \mathbb{R}^{n \times m}$ be the Jacobian matrix of the projection \mathbf{f} at the origin. Throughout the paper, we assume that $\nabla \mathbf{f}(0)$ has full-rank since $\nabla \mathbf{f}$ is non-singular in general case. We further assume that there exists a column vector $\nabla \mathbf{f}(0)_{:,c}$ that is *aligned with* the projected true gradient $\text{proj}_{\nabla \mathbf{f}(0)} \nabla S(x_t)$, and other column vectors are orthogonal to it. Formally, there exists $c \in [m]$, such that $\nabla \mathbf{f}(0)_{:,c} = k \text{proj}_{\nabla \mathbf{f}(0)} \nabla S(x_t)$ with $k \neq 0$, and for any $i \neq c$, $\langle \nabla \mathbf{f}(0)_{:,i}, \nabla \mathbf{f}(0)_{:,c} \rangle = 0$. This assumption guarantees that the projection model \mathbf{f} produces *no* directional sampling bias for true gradient estimation (Lemma A.3) following the standard setting. We remark that since vectors tend to be orthogonal to each other in high-dimensional

case (Fiers, 2018), this assumption holds with higher confidence in high-dimensional cases. In Section 5.2, we empirically verify this assumption.

Lemma 4.1 (∇f Decomposition). *Under the above assumption, there exists a singular value decomposition of $\nabla f(0) = U\Sigma V^\top$ such that*

$$U_{:,1} = \text{proj}_{\nabla f(0)} \nabla S(x_t) / \|\text{proj}_{\nabla f(0)} \nabla S(x_t)\|_2$$

$$\text{or } U_{:,1} = -\text{proj}_{\nabla f(0)} \nabla S(x_t) / \|\text{proj}_{\nabla f(0)} \nabla S(x_t)\|_2$$

where $U \in \mathbb{R}^{n \times n}$, $V \in \mathbb{R}^{m \times m}$ are orthogonal matrices; $\Sigma = \text{diag}(\alpha_1, \alpha_2, \dots, \alpha_m) \in \mathbb{R}_{\geq 0}^{n \times m}$ is a rectangular diagonal matrix with $\alpha_1 > 0$. Denote $\max_{i \in [m]} \alpha_i$ as α_{\max} .

The proof can be found in Appendix A.3. Compared with the standard SVD decomposition, now the first column vector of U can be fixed to the normalized projected true gradient vector or its opposite.

Definition of Sensitivity. In Lemma 4.1, for projection f , we can view the resulting α_1 as the *sensitivity* of the projection model on the (projected) true gradient direction; and $\{\alpha_i\}_{i=2}^m$ as the *sensitivity* of the projection model on directions orthogonal to the true-gradient. With higher sensitivity on projected true gradient direction (α_1) and smaller sensitivity on other orthogonal directions ($\{\alpha_i\}_{i=2}^m$), the gradient estimation becomes better as we will show later.

MAIN THEOREMS

Here we will present our main theorems for the expectation (Theorem 1) and concentration bound (Theorem 2) of cosine similarity between the estimated and true gradients.

Theorem 1 (Expected cosine similarity). *The difference function S and the projection f are as defined before. For a point x_t that is θ -close to the boundary, i.e., there exists $\theta' \in [-\theta, \theta]$ such that $S(x_t + \theta' S(x_t)) / \|\nabla S(x_t)\|_2 = 0$, let estimated gradient $\widetilde{\nabla S}(x_t)$ be as computed by Definition 2 with step size δ and sampling size B . Over the randomness of the sampled vectors $\{u_b\}_{b=1}^B$,*

$$\cos\langle \mathbb{E} \widetilde{\nabla S}(x_t), \nabla S(x_t) \rangle \geq \frac{\|\text{proj}_{\nabla f(0)} \nabla S(x_t)\|_2}{\|\nabla S(x_t)\|_2} \cdot \left(1 - \frac{(m-1)^2 \delta^2}{8\alpha_1^2} \left(\frac{\delta \gamma^2}{\alpha_1} + \frac{\gamma}{\alpha_1} \sqrt{\frac{\sum_{i=2}^m \alpha_i^2}{m-1}} + \frac{1.58\beta_f}{\sqrt{m-1}} \right)^2 + \frac{\gamma\theta}{\alpha_1\delta} \cdot \frac{\|\nabla S(x_t)\|_2}{\|\text{proj}_{\nabla f(0)} \nabla S(x_t)\|_2} \right),$$

where

$$\gamma := \beta_f + \frac{\beta_S (\max_{i \in [m]} \alpha_i + 1/2\delta\beta_f)^2 + \beta_S \theta^2 / \delta^2}{\|\text{proj}_{\nabla f(0)} \nabla S(x_t)\|_2}. \quad (4)$$

Proof Sketch. The high-level idea is using Taylor expansion with Lagrange remainder to control both the first-order and

higher-order errors, and plug the error terms into the distribution of dot product between $\nabla S(x_t)$ and $\nabla f(0) \cdot u_b$. This dot product follows a linearly transformed Beta distribution (Chen et al., 2020). The error terms are separately controlled for the projected gradient direction (i.e., direction of $\text{proj}_{\nabla f(0)} \nabla S(x_t)$) and other orthogonal directions. Then the controlled directional errors are combined as an ℓ_2 -bounded error vector. The complete proof is deferred to Appendix A.6. \square

Remark. This bound characterizes the expected cosine similarity of the boundary gradient estimator. For an identical projection f , if x_t is exactly the boundary point, i.e., $S(x_t) = 0$, from the theorem we get

$$\cos\langle \mathbb{E} \widetilde{\nabla S}(x_t), \nabla S(x_t) \rangle \geq 1 - \frac{(n-1)^2 \delta^2 \beta_S^2}{2\|\nabla S(x_t)\|_2^2},$$

where we leverage the fact that $\delta = O(1/n)$ is usually small. This bound is of the same order as the previous work (Chen et al., 2020) shown in Eq. (3), while containing a tighter constant $1/2$ instead of $9/8$.

Suppose both the difference function S and projection f are linear, i.e., $\beta_S = \beta_f = 0$, then we have $\cos\langle \mathbb{E} \widetilde{\nabla S}(x_t), \nabla S(x_t) \rangle \geq \frac{\|\text{proj}_{\nabla f(0)} \nabla S(x_t)\|_2}{\|\nabla S(x_t)\|_2}$. From Lemma A.1, this is the optimal cosine similarity obtainable with the projection f . Furthermore, for identical projection, $\cos\langle \mathbb{E} \widetilde{\nabla S}(x_t), \nabla S(x_t) \rangle \geq 1$, which verifies the optimality of our bound over existing work (Li et al., 2020a; 2021).

Theorem 2 (Concentration of cosine similarity). *Under the same setting as Theorem 1, over the randomness of the sampled vector $\{u_b\}_{b=1}^B$, with probability $1 - p$,*

$$\cos\langle \widetilde{\nabla S}(x_t), \nabla S(x_t) \rangle \geq \frac{\|\text{proj}_{\nabla f(0)} \nabla S(x_t)\|_2}{\|\nabla S(x_t)\|_2} \cdot \left(1 - \frac{(m-1)^2 \delta^2}{8\alpha_1^2} \left(\frac{\delta \gamma^2}{\alpha_1} + \frac{\gamma}{\alpha_1} \sqrt{\frac{\sum_{i=2}^m \alpha_i^2}{m-1}} + \frac{1.58\beta_f}{\sqrt{m-1}} \right)^2 + \frac{\gamma\theta}{\alpha_1\delta} \cdot \frac{\|\nabla S(x_t)\|_2}{\|\text{proj}_{\nabla f(0)} \nabla S(x_t)\|_2} + \frac{\frac{1}{\delta} \sqrt{\sum_{i=1}^m \alpha_i^2} \cdot \sqrt{\frac{2}{B} \ln(\frac{m}{p})}}{\sqrt{m-1}} \right)^2,$$

where γ is as defined in Eq. (4).

Proof Sketch. Each u_b is sampled independently, and on each axis the samples are averaged. Therefore, we apply Hoeffding's inequality on each axis, and use the union bound to bound the total ℓ_2 length of the error vector. We propagate this extra error term throughout the proof of Theorem 1. The detail proof is in Appendix A.7. \square

Remark. This is the *first* concentration bound for the boundary gradient estimator to our best knowledge. From it we quantitatively learn how increasing the number of queries B increases the precision of the estimator, while the expectation bound cannot reflect it directly.

We note that the above two theorems are general—they provide finer-grained bounds for *all* existing boundary blackbox attacks, e.g., (Chen et al., 2020; Li et al., 2021; 2020a), and the proposed PSBA, thus these bounds provide a principled framework to analyze boundary blackbox attacks. Next, based on this framework we will (1) discover key characteristics that affect the query efficiency of gradient estimation; (2) explain why some existing attacks are more efficient than others; (3) show why PSBA improves upon these attacks.

KEY CHARACTERISTICS OF PROJECTIVE GRADIENT ESTIMATION

Based on these two main theorems, we draw several observations for key characteristics that would help improve the gradient estimator. For simplification, we will leverage the big- \mathcal{O} notation for the above expectation and concentration bounds (Theorems 1 and 2), as shown in Fig. 3. Compared with the expectation bound, the concentration bound adds a “sampling error term” that makes the bound hold with probability at least $1 - p$. In Fig. 3, we label different terms in different colors to represent the key characteristics as optimization goals of a good gradient estimator:

- (1) *Reduce the dimensionality m for the projection subspace*: To increase the cosine similarity, we can reduce the dimensionality m .
- (2) *Increase the projected length of true gradient on the projection subspace*: To increase the cosine similarity, we can increase the brown term $\|\text{proj}_{\nabla f(0)} \nabla S(x_t)\|_2$, which is the projected length of true gradient on the projection subspace of f .
- (3) *Improve the sensitivity on the true gradient direction*: According to Lemma 4.1, α_1 is the sensitivity for the true gradient direction, and α_i for $i \neq 1$ is the sensitivity for orthogonal directions. To increase the cosine similarity, we can increase the blue term α_1 , or reduce the green term $\frac{\sum_{i=2}^m \alpha_i^2}{m-1}$ and α_{\max}^4 . In Section 5.2, we empirically verify that PGAN achieves this, where α_1^2 is consistently and significantly larger than $\frac{\sum_{i=2}^m \alpha_i^2}{m-1}$, and therefore we leverage PGAN in our implementation. Note that for identical projection (Chen et al., 2020) or orthogonal projection (Li et al., 2020a), all α_i ’s are equal. The performance gain in NonLinearBA (Li et al., 2021) can be explained by this characteristic.

We illustrate these key characteristics in Appendix B. Other factors that can improve the cosine similarity are also revealed, such as smaller step size δ , and larger sampling (i.e., query) numbers B . However, they directly come at the cost of more queries as discussed in (Chen et al., 2020).

To improve the precision and query efficiency of the gradient estimation, next we consider how to optimize the estimator on the above characteristics, especially (1) and (2), given that (3) can be achieved by a PGAN-based projection.

Trade-Off on Dimensionality. From Fig. 3, we observe an apparent trade-off between Key Characteristics (1) and (2): when reducing the dimensionality m of the projection subspace (goal (1)), the preserved gradient information $\|\text{proj}_{\nabla f(0)} \nabla S(x_t)\|_2$ in this m -dimensional linear subspace $\nabla f(0)$ becomes less, which opposes goal (2). To make a tradeoff between (1) and (2), based on above observation, there exists an optimal dimensionality m for the projection, and this dimensionality depends on how much true gradient information the projection subspace can preserve.

4.2. Optimize via Selecting Projection Subspaces

To circumvent the intrinsic trade-off, instead of hoping that the end-to-end trained f can capture much true gradient information in its linear subspace $\nabla f(0)$, we can actively constrain the projection f on a representative subspace.

Here we focus on the linear subspace which can be represented by a linear combination of a set of basis, since the small step size δ of gradient estimator implies that only the local geometry matters and the local geometry of general subspace can be sufficiently approximated in first-order by linear subspace. Concretely, we select an m -dimensional linear subspace $V \subseteq \mathbb{R}^n$. Then, we train the projection f on V , i.e., $\text{im}(f) \subseteq V$. Finally, we estimate the gradient with this f as: $u \in \mathbb{R}^m \xrightarrow{f} \Delta f(\delta u) \in V \subseteq \mathbb{R}^n$, where $\dim(V) = m$. Interchangeably, we call m , the dimensionality of V , as *scale*, since it reflects the scale of the projection subspace V as we will show later.

Now we can analyze the cosine similarity of this new workflow. Since the image of projection f is in V , and $\text{rank}(\nabla f(0)) = \dim(V) = m$, we have $\text{span}(\nabla f(0)) = V$ and $\|\text{proj}_{\nabla f(0)} \nabla S(x_t)\|_2 / \|\text{proj}_V \nabla S(x_t)\|_2 = 1$. Plugging this into the above theorems and deriving from simple geometry (details in Lemma A.1), we find that the cosine similarity bound for subspace-constrained f is of the same form as in Fig. 3, with all $\|\text{proj}_{\nabla f(0)} \nabla S(x_t)\|_2^2$ replaced by $\|\text{proj}_V \nabla S(x_t)\|_2^2$.

Selected Subspace Improves Gradient Estimation. The formulation in Fig. 3 reveals that as long as we select an m -dimensional linear subspace V that preserves more gradient information $\|\text{proj}_V \nabla S(x_t)\|_2$ than the unconstrained projection model $\|\text{proj}_{\nabla f(0)} \nabla S(x_t)\|_2$, the estimated gradient would have higher cosine similarity. We empirically find that the low-frequency subspace³ satisfies such condition (Section 5.2): for real-world images, the gradient information of classifiers is highly concentrated on low-frequency domain. This is also cross-validated in the literature (Yin et al., 2019). We illustrate this analysis along with curves from numerical experiments in Fig. 4.

³Low-frequency subspace in DCT basis is a linear subspace.

$$\cos\langle \widetilde{\nabla S}(x_t), \nabla S(x_t) \rangle \geq \frac{\|\text{proj}_{\nabla f(0)} \nabla S(x_t)\|_2}{\|\nabla S(x_t)\|_2} \cdot \left(1 - \mathcal{O} \left(m^2 \cdot \frac{\sum_{i=2}^m \alpha_i^2}{m-1} \left(\underbrace{\frac{\delta^2 \beta_f^2}{\alpha_1^4} + \frac{\alpha_{\max}^4}{\alpha_1^4}}_{\text{expectation}} \cdot \frac{\delta^2 \beta_S^2}{\|\text{proj}_{\nabla f(0)} \nabla S(x_t)\|_2^2} + \underbrace{\frac{\ln(m/p)}{B \alpha_1^2}}_{\text{sampling error}} \right) \right) \right)$$

Figure 3. Cosine similarity bound in big- \mathcal{O} notation. The “expectation” reflects the expectation bound in Theorem 1. The “sampling error” is the additional term in Theorem 2 that makes the bound hold with probability at least $1 - p$. When projection \mathbf{f} is constrained in selected linear subspace V (see Section 4.2), the bound has the same form with all $\|\text{proj}_{\nabla f(0)} \nabla S(x_t)\|_2^2$ replaced by $\|\text{proj}_V \nabla S(x_t)\|_2^2$.

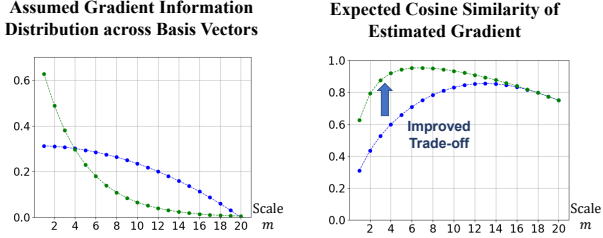


Figure 4. An illustration of why selected subspace improves the gradient estimation. **Left:** we assume a quadratic distribution of gradient information for \mathbf{f} ’s basis (blue curve) and a more concentrated exponential distribution for frequency basis (green curve). **Right:** the corresponding expected cosine similarity is numerically computed with settings $n = 20$, $\beta_S = 0.5$, $\beta_f = 0$, $\alpha_i = 1$, $\delta = m^{-1}$. The improved trade-off w.r.t. scale is revealed.

Recall that in PSBA, we train \mathbf{f} on a smaller spatial scale and scale up its output, which is equivalent to constraining \mathbf{f} on the low-frequency subspace. Since this subspace is more representative than the subspace $\nabla \mathbf{f}(0)$ of end-to-end trained \mathbf{f} , theoretically PSBA can estimate gradient with higher cosine similarity within fewer queries.

Existence of Optimal Scale. From Fig. 3, we find that the trade-off between Key Characteristics (1) and (2) in Section 4.1 still exists for selected subspace in general. Now it transforms to the existence of an optimal scale. This is revealed by the green curve in Fig. 4. For spatial and frequency scales, across different images from the same dataset and model, the coefficients of gradient information on the frequency basis vector tend to be very stable, as Section 5.2 shows. It implies that $\|\text{proj}_V \nabla S(x_t)\|_2$ in Fig. 3 across different images tend to be stable, and the optimal scales for gradient estimation tend to be stable too. Therefore, we can search for the optimal scale with a validation dataset.

5. Experimental Evaluation

With the established general framework of leveraging progressive scaling to improve attack efficiency, in this section, we take PGAN as an instantiation and conduct extensive experiments to 1) verify our theoretical analysis; 2) show that PSBA outperforms existing blackbox attacks by a significantly large margin. We also present some additional interesting findings.

5.1. Experimental Setup

Target Models. We use both offline models and a commercial online API as target models. For offline models, following (Li et al., 2020a; 2021), pretrained ResNet-18 on MNIST, CIFAR-10, CelebA and ImageNet are utilized. We also evaluate model ResNeXt50_32×4d (Xie et al., 2017) to demonstrate the generalization ability. On datasets MNIST and CIFAR-10, we scale up the input images to 224×224 by bilinear interpolation to help explore the influence of different scales. On CelebA, the target model is fine-tuned to perform the binary classification on the attribute ‘Mouth.Slightly.Open’. The benign performance of target models is shown in Appendix C.2. For the commercial online API, the ‘Compare’ API (MEGVII, 2020a) from MEGVII Face++ which determines whether the faces from two images belong to the same person is used as the target model. The compared images are chosen from CelebA. The rationale of selecting these classification tasks and a detailed description of target models are discussed in Appendix C.

Training Procedure of PGAN. PGAN is trained to generate gradient images of reference models with small resolution until reaching convergence, and then new layers will be added to double the output scale. The PGAN training details could be found in Appendix D.2 and reference models’ performance are shown in Appendix D.3. For simplicity, we will denote ‘PGAN28’ as the attack using the output of PGAN with scale 28×28 .

Implementation. We follow the description in Section 3 to implement PSBA. Compared to other common attacks, we additionally train PGAN and use an additional validation set of ten images to search for the optimal scale. More implementation details are shown in Appendices D.4 and D.5.

Baselines. We consider six state-of-the-art decision-based attacks as the baselines. Among our baselines, **QEBA** (Li et al., 2020a) and **NLBA** (Li et al., 2021) utilize dimension reduction to sample from low-dimensional space, while the **Sign-OPT** (Cheng et al., 2020) and **HSJA** (Chen et al., 2020) apply direct Monte-Carlo sampling for gradient estimation. **EA** (Dong et al., 2019) adopts evolution algorithm to perform the attack. Note that we directly select the optimal scale for EA to compare under its optimal case. In Appendix E.4 we compare with **RayS** attack (Chen & Gu, 2020).

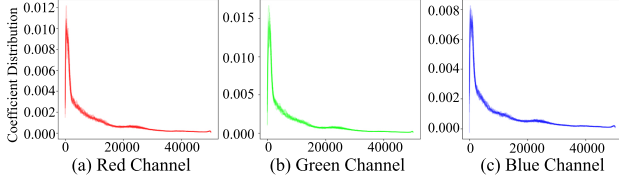


Figure 5. The long tail distribution of the coefficients of gradients generated from 10 images on the validation set of CIFAR-10 and represented on DCT basis for each channel.

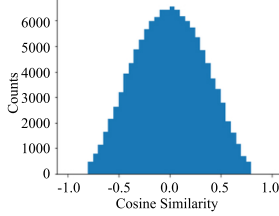


Figure 6. Pairwise cosine similarity of $\nabla f(0)$ column vectors.

Evaluation Metrics. We adopt the standard evaluation metrics: 1) the Mean Squared Error (MSE) between the optimized adversarial examples and target image under different queries (this process will guarantee 100% attack success rate); 2) attack success rate at a specific MSE perturbation bound when the query number is constrained. Note that the conversion between MSE and ℓ_2 metrics are straightforward and order-preserving.

5.2. Verification of Theoretical Findings

Low Frequency Concentration. In order to verify the hypothesis of low frequency concentration, we randomly sample 10 gradient vectors calculated on ResNet-18 model for CIFAR-10 dataset. The gradients are normalized and transformed with DCT basis for each channel. As shown in Fig. 5, the x -axis shows the DCT basis from low to high frequency, and y -axis represents the corresponding coefficients denoised by the Savitzky-Golay filter. The three curves denote the three color channels respectively. The figures show stable long tail distribution across various images, and this implies the benefit of selecting the low-frequency subspace as the projection subspace in gradient estimation, as well as the existence of a stable optimal scale for the same dataset and target model, providing strong evidence for the discussion in Section 4.2. In addition, we draw a graph in a more statistical sense in Appendix E.6.

High Sensitivity on Gradient Direction. As shown in Appendix E.7, for trained PGAN, we compare the sensitivity (Lemma 4.1) for the projected true gradient direction, α_1^2 , and the averaged sensitivity for other orthogonal directions, $\sum_{i=2}^m \alpha_i^2 / (m-1)$. On all datasets, α_1^2 is significantly larger than $\sum_{i=2}^m \alpha_i^2 / (m-1)$, which implies that trained PGAN achieves higher sensitivity on the true gradient direction. This is exactly the goal (3) in Section 4.1. In contrast, the identical (Chen et al., 2020) and orthogonal projection (Li et al., 2020a) have identical directional sensitivity.

To what extent does orthogonality assumption hold. Here, we compute $\nabla f(0)$ of PSBA on ImageNet at the optimal scale and then cluster the similar column vectors (those with cosine similarity > 0.8 or < -0.8) since they contribute to the sensitivity of one direction. Next, we compute the pairwise cosine similarity between clusters. The histogram of clusters based on their cosine similarity is shown in Fig. 6. As we can see, the histogram concentrates at 0, i.e., orthogonal pairs are most frequent. We also remark that recent orthogonal training can also enforce the assumption (Huang et al., 2020).

5.3. Attack Performance Evaluation

In this section, we show that the optimal scale indeed exists and our method PSBA-PGAN outperforms other state-of-the-art baselines in terms of attack effectiveness and efficiency. In addition, by selecting the optimal scale, PSBA-PGAN can also successfully and efficiently attack the online commercial face recognition API. Here, we randomly select 50 pairs of source and target images from validation set that are predicted by the target model as different classes for both offline attack and online attack and the selections of other hyperparameters are shown in Appendix E.1.

Offline Attack. The attack performance of different approaches in terms of the perturbation magnitude (MSE) between the adversarial and target image is shown in Fig. 7 (a)-(c). As we can see from Row 1, PSBA-PGAN effectively decrease the MSE when the number of queries is small and outperforms all baselines. Detailed comparisons on the gradient cosine similarity are in Appendix E.5. From Row 2 we can see that, interestingly, the optimal scale found by PSBA-PGAN across four datasets is consistently 28×28 .

In Table 1, we show the attack success rate when the query number is constrained by 2K. This is because we can not easily generate a large number of queries (e.g., exceeding 2K) for attacking one image, and our PSBA is designed to be a query efficient attack with fast convergence speed. We can see that PSBA indeed significantly outperforms other methods when attacking Face++ API under small query budgets. On the other hand, when the query budgets get bigger, most of the methods would converge and attack successfully, then the comparison under this circumstance is not quite useful. We leave the results with large query number constraints in Appendix E.3. Besides, we also compare our method with RayS attack (Chen & Gu, 2020) in Appendix E.4. Detailed discussions on the computation time and resource consumption are in Appendix E.2, and the visualized results for other target models and ImageNet are in Appendix E.3.

Online Attack. To demonstrate the generalization and practicality of PSBA-PGAN, we perform it against a real-world online commercial API as shown in Fig. 7 (d). Although the PGAN used here is trained on ImageNet, PSBA-PGAN

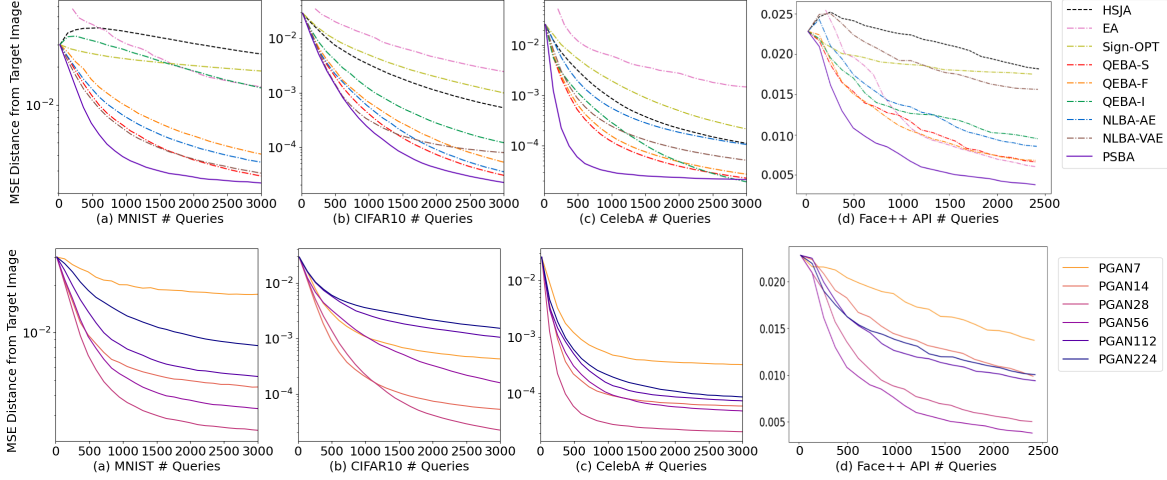


Figure 7. Row 1: Perturbation magnitude (MSE) w.r.t. query numbers for attacks on diverse datasets/models. **Row 2:** Perturbation magnitude when choosing different scales as the projection subspaces. The target model in (a)-(c) is ResNet-18, and an online commercial API in (d).

Table 1. Comparison of the attack success rate for different attacks at query number 2K (the perturbation magnitude under MSE for each dataset are: MNIST: $5e-3$; CIFAR10: $5e-4$; CelebA: $1e-4$; ImageNet: $1e-2$).

Data	Model	# Queries = 2K								
		HSJA	EA	Sign-OPT	QEBA-S	QEBA-F	QEBA-I	NLBA-AE	NLBA-VAE	PSBA
MNIST	ResNet	2%	6%	2%	60%	42%	4%	46%	58%	78%
	ResNeXt	4%	4%	6%	76%	66%	16%	70%	80%	88%
CIFAR10	ResNet	26%	10%	10%	82%	70%	58%	76%	82%	94%
	ResNeXt	32%	0%	18%	88%	72%	64%	90%	90%	90%
CelebA	ResNet	20%	8%	2%	80%	70%	72%	20%	46%	90%
	ResNeXt	24%	6%	6%	60%	56%	72%	20%	38%	88%
ImageNet	ResNet	24%	24%	6%	54%	52%	46%	44%	28%	54%
	ResNeXt	20%	22%	16%	40%	38%	36%	28%	26%	42%

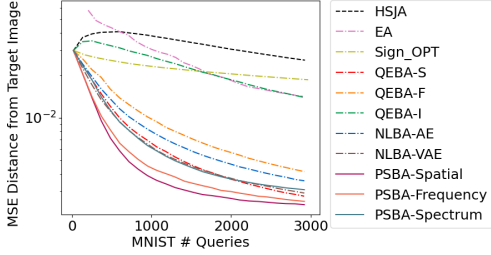


Figure 8. Perturbation magnitude (MSE) under different number of queries on MNIST for PSBA sampling from spatial, frequency, and spectrum domains.

still outperforms other baselines and interestingly, it adopts the optimal scale as 56×56 .

Frequency and Spectrum Domains. In addition to the spatial domain, we also evaluate PSBA on frequency and spectrum domains. The results are shown in Fig. 8. PSBA outperforms other baselines. Detailed implementations and other ablation studies are included in Appendix E.8.

Additional Findings. (1) In Appendix E.7, we deliberately adjust the sensitivity on different directions $\{\alpha_i\}_{i=1}^m$ for given projection f to study the correlation between sensitivity and empirical attack performance. The results conform

to our theoretical findings (goal (3) in Section 4.1). (2) We empirically study the optimal scale across model structures and show that different models have their own preference, which we believe will lead to interesting future directions. More details can be found in Appendix E.9.

6. Conclusion

In this paper, we propose PSBA, a progressive-scale blackbox attack via projective gradient estimation. We propose a general theoretical framework to analyze existing projective gradient estimators, show key characteristics for improvement, and justify why PSBA outperforms other blackbox attacks. Extensive experiments verify our theoretical findings and show that PSBA outperforms existing blackbox attacks significantly against various target models including a real-world face recognition API.

Acknowledgements

We thank the anonymous reviewers for valuable feedback. This work is partially supported by NSF grant No.1910100, NSF CNS 20-46726 CAR, and Amazon Research Award.

References

- Bhagoji, A. N., He, W., Li, B., and Song, D. Practical black-box attacks on deep neural networks using efficient query mechanisms. In *European Conference on Computer Vision*, pp. 158–174. Springer, 2018.
- Brendel, W., Rauber, J., and Bethge, M. Decision-based adversarial attacks: Reliable attacks against black-box machine learning models. In *International Conference on Learning Representations*, 2018.
- Cai, Z., Fan, Q., Feris, R. S., and Vasconcelos, N. A unified multi-scale deep convolutional neural network for fast object detection. In *European conference on computer vision*, pp. 354–370. Springer, 2016.
- Chen, J. and Gu, Q. Rays: A ray searching method for hard-label adversarial attack. In *Proceedings of the 26th ACM SIGKDD International Conference on Knowledge Discovery & Data Mining*, pp. 1739–1747, 2020.
- Chen, J., Jordan, M. I., and Wainwright, M. J. Hop-skipjumpattack: A query-efficient decision-based attack. In *2020 IEEE symposium on security and privacy (SP)*, pp. 1277–1294. IEEE, 2020.
- Chen, P.-Y., Zhang, H., Sharma, Y., Yi, J., and Hsieh, C.-J. Zoo: Zeroth order optimization based black-box attacks to deep neural networks without training substitute models. In *Proceedings of the 10th ACM Workshop on Artificial Intelligence and Security*, pp. 15–26, 2017.
- Cheng, M., Singh, S., Chen, P. H., Chen, P.-Y., Liu, S., and Hsieh, C.-J. Sign-opt: A query-efficient hard-label adversarial attack. In *International Conference on Learning Representations*, 2019a.
- Cheng, M., Singh, S., Chen, P., Chen, P.-Y., Liu, S., and Hsieh, C.-J. Sign-opt: A query-efficient hard-label adversarial attack, 2020.
- Cheng, S., Dong, Y., Pang, T., Su, H., and Zhu, J. Improving black-box adversarial attacks with a transfer-based prior. In *Advances in Neural Information Processing Systems*, pp. 10932–10942, 2019b.
- Clarke, F. H., Ledyaev, Y. S., Stern, R. J., and Wolenski, P. R. *Nonsmooth analysis and control theory*, volume 178. Springer Science & Business Media, 2008.
- Deng, J., Dong, W., Socher, R., Li, L.-J., Li, K., and Fei-Fei, L. ImageNet: A Large-Scale Hierarchical Image Database. In *CVPR09*, 2009.
- Dong, Y., Su, H., Wu, B., Li, Z., Liu, W., Zhang, T., and Zhu, J. Efficient decision-based black-box adversarial attacks on face recognition. In *Proceedings of the IEEE/CVF Conference on Computer Vision and Pattern Recognition*, pp. 7714–7722, 2019.
- Fiers, T. Why are randomly drawn vectors nearly perpendicular in high dimensions. Mathematics Stack Exchange, 2018. URL <https://math.stackexchange.com/q/995678>. URL: <https://math.stackexchange.com/q/995678> (version: 2018-05-15).
- Goodfellow, I. J., Shlens, J., and Szegedy, C. Explaining and harnessing adversarial examples. *arXiv preprint arXiv:1412.6572*, 2014.
- Guo, Y., Yan, Z., and Zhang, C. Subspace attack: Exploiting promising subspaces for query-efficient black-box attacks. In Wallach, H., Larochelle, H., Beygelzimer, A., d’Alché-Buc, F., Fox, E., and Garnett, R. (eds.), *Advances in Neural Information Processing Systems*, volume 32. Curran Associates, Inc., 2019.
- He, K., Zhang, X., Ren, S., and Sun, J. Deep residual learning for image recognition, 2015a.
- He, K., Zhang, X., Ren, S., and Sun, J. Delving deep into rectifiers: Surpassing human-level performance on imagenet classification, 2015b.
- He, K., Zhang, X., Ren, S., and Sun, J. Deep residual learning for image recognition. In *Proceedings of the IEEE conference on computer vision and pattern recognition*, pp. 770–778, 2016.
- Huang, G., Liu, Z., van der Maaten, L., and Weinberger, K. Q. Densely connected convolutional networks, 2018.
- Huang, L., Liu, L., Zhu, F., Wan, D., Yuan, Z., Li, B., and Shao, L. Controllable orthogonalization in training dnns. In *Proceedings of the IEEE/CVF Conference on Computer Vision and Pattern Recognition*, pp. 6429–6438, 2020.
- Ilyas, A., Engstrom, L., Athalye, A., and Lin, J. Black-box adversarial attacks with limited queries and information. In *International Conference on Machine Learning*, pp. 2137–2146, 2018.
- Karras, T., Aila, T., Laine, S., and Lehtinen, J. Progressive growing of gans for improved quality, stability, and variation, 2018.
- Krizhevsky, A., Hinton, G., et al. *Learning multiple layers of features from tiny images*. Citeseer, 2009.
- Kurakin, A., Goodfellow, I., and Bengio, S. Adversarial examples in the physical world. *arXiv preprint arXiv:1607.02533*, 2016.
- LeCun, Y., Bottou, L., Bengio, Y., and Haffner, P. Gradient-based learning applied to document recognition. *Proceedings of the IEEE*, 86(11):2278–2324, 1998.

- Li, H., Xu, X., Zhang, X., Yang, S., and Li, B. Qeba: Query-efficient boundary-based blackbox attack. In *Proceedings of the IEEE/CVF Conference on Computer Vision and Pattern Recognition (CVPR)*, June 2020a.
- Li, H., Li, L., Xu, X., Zhang, X., Yang, S., and Li, B. Nonlinear gradient estimation for query efficient blackbox attack. In *Proceedings of 24th International Conference on Artificial Intelligence and Statistics*, 2021.
- Li, J., Ji, R., Liu, H., Liu, J., Zhong, B., Deng, C., and Tian, Q. Projection & probability-driven black-box attack. In *Proceedings of the IEEE/CVF Conference on Computer Vision and Pattern Recognition*, pp. 362–371, 2020b.
- Lin, T.-Y., Dollár, P., Girshick, R., He, K., Hariharan, B., and Belongie, S. Feature pyramid networks for object detection. In *Proceedings of the IEEE conference on computer vision and pattern recognition*, pp. 2117–2125, 2017.
- Liu, Z., Luo, P., Wang, X., and Tang, X. Deep learning face attributes in the wild. In *Proceedings of International Conference on Computer Vision (ICCV)*, December 2015.
- Ma, W., Wu, Y., Cen, F., and Wang, G. Mdfn: Multi-scale deep feature learning network for object detection. *Pattern Recognition*, 100:107149, 2020.
- Madry, A., Makelov, A., Schmidt, L., Tsipras, D., and Vladu, A. Towards deep learning models resistant to adversarial attacks. In *International Conference on Learning Representations*, 2018.
- MEGVII. Face++ facial recognition ‘compare’ API documentation. <https://console.faceplusplus.com/documents/5679308>, 2020a.
- MEGVII. Face++ facial recognition ‘compare’ API query URL. <https://api-us.faceplusplus.com/facepp/v3/compare>, 2020b.
- MEGVII. Face++. <https://www.faceplusplus.com/>, 2020c.
- Papernot, N., McDaniel, P., and Goodfellow, I. Transferability in machine learning: from phenomena to black-box attacks using adversarial samples. *arXiv preprint arXiv:1605.07277*, 2016.
- PyTorch. Torchvision.models. <https://pytorch.org/docs/stable/torchvision/models.html>, 2020.
- Research, F. Pytorch GAN zoo. https://github.com/facebookresearch/pytorch_GAN_zoo, 2020.
- Simonyan, K. and Zisserman, A. Very deep convolutional networks for large-scale image recognition, 2015.
- Suya, F., Chi, J., Evans, D., and Tian, Y. Hybrid batch attacks: Finding black-box adversarial examples with limited queries. In *29th {USENIX} Security Symposium ({USENIX} Security 20)*, pp. 1327–1344, 2020.
- Szegedy, C., Zaremba, W., Sutskever, I., Bruna, J., Erhan, D., Goodfellow, I., and Fergus, R. Intriguing properties of neural networks. *arXiv preprint arXiv:1312.6199*, 2013.
- Szegedy, C., Liu, W., Jia, Y., Sermanet, P., Reed, S., Anguelov, D., Erhan, D., Vanhoucke, V., and Rabinovich, A. Going deeper with convolutions, 2014.
- Tashiro, Y., Song, Y., and Ermon, S. Diversity can be transferred: Output diversification for white-and black-box attacks. *Advances in Neural Information Processing Systems*, 33, 2020.
- Tramèr, F., Papernot, N., Goodfellow, I., Boneh, D., and McDaniel, P. The space of transferable adversarial examples. *arXiv preprint arXiv:1704.03453*, 2017.
- Tu, C.-C., Ting, P., Chen, P.-Y., Liu, S., Zhang, H., Yi, J., Hsieh, C.-J., and Cheng, S.-M. Autozoom: Autoencoder-based zeroth order optimization method for attacking black-box neural networks. In *Proceedings of the AAAI Conference on Artificial Intelligence*, volume 33, pp. 742–749, 2019.
- Tu, C.-C., Ting, P., Chen, P.-Y., Liu, S., Zhang, H., Yi, J., Hsieh, C.-J., and Cheng, S.-M. Autozoom: Autoencoder-based zeroth order optimization method for attacking black-box neural networks, 2020.
- Vaswani, A., Shazeer, N., Parmar, N., Uszkoreit, J., Jones, L., Gomez, A. N., Kaiser, L., and Polosukhin, I. Attention is all you need. In *NIPS*, 2017.
- Wu, R., Zhang, G., Lu, S., and Chen, T. Cascade ef-gan: Progressive facial expression editing with local focuses. In *Proceedings of the IEEE/CVF Conference on Computer Vision and Pattern Recognition*, pp. 5021–5030, 2020.
- Xie, S., Girshick, R., Dollár, P., Tu, Z., and He, K. Aggregated residual transformations for deep neural networks, 2017.
- Yang, G., Duan, T., Hu, E., Salman, H., Razenshteyn, I., and Li, J. Randomized smoothing of all shapes and sizes. In *International Conference on Machine Learning*, 2020.
- Yin, D., Gontijo Lopes, R., Shlens, J., Cubuk, E. D., and Gilmer, J. A fourier perspective on model robustness in computer vision. *Advances in Neural Information Processing Systems*, 32:13276–13286, 2019.

Zagoruyko, S. and Komodakis, N. Wide residual networks, 2017.

Zhang, D. and Khoreva, A. Progressive augmentation of gans. In *Advances in Neural Information Processing Systems*, pp. 6249–6259, 2019.

Zhang, J., Xie, Z., Sun, J., Zou, X., and Wang, J. A cascaded r-cnn with multiscale attention and imbalanced samples for traffic sign detection. *IEEE Access*, 8:29742–29754, 2020.

Supplementary Material for Progressive-Scale Blackbox Attack via Projective Gradient Estimation

Jiawei Zhang^{*1} Linyi Li^{*2} Huichen Li² Xiaolu Zhang³ Shuang Yang⁴ Bo Li²

In Appendix A, we show a summary of our theoretical results, compare it with related work, and demonstrate the complete proofs. In Appendix B, we visualize the key characteristics for improving the gradient estimator, and formally justify the existence of the optimal scale. In Appendix C, we show how the target models, i.e., the models we attacked in the experiments, are prepared. In Appendix D, we include more details about our PSBA-PGAN, such as the architecture and training of the projection model, the detailed algorithmic description of the progressive scaling procedure, and the implementation details. In Appendix E, we show additional quantitative experimental results and ablation studies. Finally, in Appendix F, we randomly sample a few original and attacked image pairs to demonstrate the efficiency of our attack compared with other baselines.

A. Theorems and Proofs

This appendix contains a discussion and comparison of theoretical results and all omitted mathematical proofs.

A.1. An outline of Main Theoretical Results

We summarize our main theoretical results—the lower bound of cosine similarity between the estimated gradient and the true gradient, in Table 2.

In the table:

- “Expectation” indicates the bound of the expected cosine similarity;
- “Concentration” indicates the bound of the cosine similarity that holds with probability at least $1 - p$;
- “At Boundary” indicates the case where the estimated point is an exact boundary point, i.e., $S_{x^*}(x) = 0$;
- “Approaching Boundary” indicates the general case where the estimated point is away from the decision boundary within a small distance θ (measured along the true gradient direction).

“At Boundary” is actually a special case of “Approaching Boundary” with $\theta = 0$. In the main text, we only present Theorems 1 and 2 that are for the general case, i.e., “Approaching Boundary” case.

Table 2. A brief summary of the cosine similarity bounds for the boundary gradient estimator in Section 4.1.

	Expectation	Concentration
At Boundary	Theorem 3	Theorem 4
Approaching Boundary	Theorem 1	Theorem 2

A.2. Comparison of Theoretical Results

We compare our theoretical results with existing work in Table 3. Note that it is better to have fewer assumptions and be applicable to more scenarios. As one can observe, our theoretical result is among the most general ones. Furthermore, as discussed in Section 4.1, ours is also among the tightest ones. From these tightest bounds, under general assumptions, we are able to discover the key characteristics and the existence of the optimal scale. The coarse bounds from the previous work cannot reflect these properties.

Table 3. A brief comparison of the cosine similarity bounds for the boundary gradient estimator in our work with existing work.

	Scenario				Assumption				
	At Boundary		Approaching Boundary		Sampling	Projection			
	Expectation	Concentration	Expectation	Concentration	Orthogonal	Identical	Linear	Orthogonal	No Bias
HSJA (Chen et al., 2020)	✓		✓			✓	✓	✓	✓
QEBA (Li et al., 2020a)	✓				✓		✓	✓	✓
NonLinear-BA (Li et al., 2021)	✓				✓				
Ours	✓	✓	✓	✓					✓

A.3. Proof of Lemma 4.1

Lemma 4.1 (∇f Decomposition). *Under the assumption in Section 4.1, there exists a singular value decomposition of $\nabla f(0) = U\Sigma V^\top$ such that*

$$U_{:,1} = \text{proj}_{\nabla f(0)} \nabla S(x_t) / \|\nabla S(x_t)\|_2 \text{ or } U_{:,1} = -\text{proj}_{\nabla f(0)} \nabla S(x_t) / \|\nabla S(x_t)\|_2$$

where $U \in \mathbb{R}^{n \times n}$ and $V \in \mathbb{R}^{m \times m}$ are orthogonal matrices; $\Sigma = \text{diag}(\alpha_1, \alpha_2, \dots, \alpha_m) \in \mathbb{R}_{\geq 0}^{n \times m}$ is a rectangular diagonal matrix with $\alpha_1 > 0$.

Proof of Lemma 4.1. For simplicity, we define $M := \nabla f(0)$. According to the assumption, there exists a column vector $M_{:,c}$ that is not orthogonal with the gradient direction $\nabla S(x_t)$. If $c \neq 1$, we define $T := [e_c \ e_2 \ \dots \ e_{c-1} \ e_1 \ e_{c+1} \ \dots \ e_m]$; otherwise, we let $T := I_m$. Here, $e_i \in \mathbb{R}^m$ is a standard basis vector, i.e., it satisfies $(e_i)_i = 1$ and $(e_i)_j = 0$ for any $j \neq i$. As the result,

$$M = [M_{:,c} \ M_{:,2} \ M_{:,3} \ \dots \ M_{:,c-1} \ M_{:,1} \ M_{:,c+1} \ \dots \ M_{:,m}]T := M'T.$$

Here $M_{:,i}$ stands for the i -th column vector of M . M' just exchanges the first column vector with the c -th column vector of M . According to the assumption in Section 4.1, $M'_{:,1}$ is aligned with $\text{proj}_M \nabla S(x_t)$, and for $i \geq 2$, we have $\langle M'_{:,i}, M'_{:,1} \rangle = 0$.

Now, we apply QR decomposition to M' via Gram-Schmidt Process, which yields $M' = U'R$, where $U' \in \mathbb{R}^{n \times n}$ is an orthogonal matrix, and $R \in \mathbb{R}^{n \times m}$ is an upper-triangular matrix. We are going to show two interesting properties of U' and R : 1) $U'_{:,1} = \frac{\text{proj}_M \nabla S(x_t)}{\|\text{proj}_M \nabla S(x_t)\|_2}$ or $U'_{:,1} = -\frac{\text{proj}_M \nabla S(x_t)}{\|\text{proj}_M \nabla S(x_t)\|_2}$; and 2) R can be written as $\begin{bmatrix} \alpha_1 & 0 \\ 0 & R' \end{bmatrix}$ where $\alpha_1 > 0$ and R' is an upper-triangular matrix. The first property is apparent, since in Gram-Schmidt Process, we always have $U'_{:,1} = M'_{:,1} / \|M'_{:,1}\|_2$. Thus, it is equal to $\pm \nabla \text{proj}_M S(x_t) / \|\text{proj}_M \nabla S(x_t)\|_2$. For the second property, according to the definition of the process, $(R)_{1,i} = \langle M'_{:,1}, M'_{:,i} \rangle = 0$. Meanwhile, $\alpha_1 = \|M'_{:,1}\|_2^2 > 0$ since $M'_{:,1}$ aligns with $\nabla S(x_t)$ and it is non-zero.

We apply SVD decomposition to the sub-matrix $R' \in \mathbb{R}^{(n-1) \times (m-1)}$: $R' := S'\Sigma'W'^\top$. Here, $S' \in \mathbb{R}^{(n-1) \times (n-1)}$ and $W' \in \mathbb{R}^{(m-1) \times (m-1)}$ are orthogonal matrices, while $\Sigma' \in \mathbb{R}^{(n-1) \times (m-1)}$ is a triangular diagonal matrix. Therefore, R can be decomposed as such:

$$R = \begin{bmatrix} \alpha_1 & 0 \\ 0 & R' \end{bmatrix} = \overbrace{\begin{bmatrix} 1 & 0 \\ 0 & S' \end{bmatrix}}^S \overbrace{\begin{bmatrix} \alpha_1 & 0 \\ 0 & \Sigma' \end{bmatrix}}^\Sigma \overbrace{\begin{bmatrix} 1 & 0 \\ 0 & W'^\top \end{bmatrix}}^{W'^\top}.$$

It is easy to observe that $\Sigma = \text{diag}(\alpha_1, \alpha_2, \dots, \alpha_m)$ is a rectangular diagonal matrix with $\alpha_1 > 0$, and V is an orthogonal matrix. Notice that

$$\begin{aligned} \nabla f(0) &= M = M'T = U'RT = U'S\Sigma W'^\top T \\ &= \begin{bmatrix} | & | & \dots & | \\ U'_{:,1} & U'_{:,2} & \dots & U'_{:,m} \\ | & | & \dots & | \end{bmatrix} \begin{bmatrix} 1 & 0 \\ 0 & S' \end{bmatrix} \Sigma W'^\top T \\ &= \underbrace{\begin{bmatrix} U'_{:,1} & U'_{:,2:m} S' \end{bmatrix}}_U \underbrace{\Sigma W'^\top T}_{V^\top}. \end{aligned}$$

We have already shown $U'_{:,1} = \frac{\text{proj}_{\nabla f(0)} \nabla S(x_t)}{\|\text{proj}_{\nabla f(0)} \nabla S(x_t)\|_2}$ or $U'_{:,1} = -\frac{\text{proj}_{\nabla f(0)} \nabla S(x_t)}{\|\text{proj}_{\nabla f(0)} \nabla S(x_t)\|_2}$. To finish the proof, we only need to verify that U and V are orthogonal matrices. Since U' and S' are both orthogonal matrices, the $U'_{:,2:m} S'$ is a semi-orthogonal

matrix (the column vectors are unitary and orthogonal). Furthermore, $U'_{:,1} \perp \text{span}(U'_{:,2:m})$ because U' is an orthogonal matrix. Thus, $U'_{:,1} \perp \text{span}(U'_{:,2:m}S')$. As the result, U is an orthogonal matrix. For V , $V^T V = W^T T T^T W = I_m$ so it is an orthogonal matrix. \square

A.4. Warmup: Expectation Bound at Boundary

As a warm-up, we begin with the special case where the point is exactly the boundary point.

The proof of the following theorems require the following lemma.

Lemma A.1 (Cosine Similarity in Projected Subspace). *Let $W \in \mathbb{R}^{n \times m}$ be a matrix. The vector $w \in \mathbb{R}^n$ is in $\text{span}(W)$, and the vector $v \in \mathbb{R}^n$ has non-zero projection in $\text{span}(W)$, i.e., $\text{proj}_W v \neq 0$. Then,*

$$\cos\langle w, v \rangle = \cos\langle w, \text{proj}_W v \rangle \cdot \frac{\|\text{proj}_W v\|_2}{\|v\|_2}. \quad (5)$$

Proof of Lemma A.1. The lemma can be illustrated by simple geometry. To be rigorous, here we give an algebraic proof.

$$\cos\langle w, v \rangle = \frac{\langle w, v \rangle}{\|w\|_2 \|v\|_2} = \frac{\langle w, v \rangle}{\|w\|_2 \|\text{proj}_W v\|_2} \cdot \frac{\|\text{proj}_W v\|_2}{\|v\|_2}.$$

We notice that $w \in \text{span}(W)$, and $v = \text{proj}_W v + (v - \text{proj}_W v)$ where $(v - \text{proj}_W v)$ is orthogonal to w . Thus,

$$\langle w, v \rangle = \langle w, \text{proj}_W v \rangle.$$

So

$$\cos\langle w, v \rangle = \cos\langle w, \text{proj}_W v \rangle \cdot \frac{\|\text{proj}_W v\|_2}{\|v\|_2}.$$

\square

Remark. The lemma reveals that for any vector w in $\text{span}(W)$, the maximum possible cosine similarity between w and v is $\|\text{proj}_W v\|_2 / \|v\|_2$. This is achieved by setting $w = k \cdot \text{proj}_W v$.

Theorem 3 (Expected cosine similarity; at boundary). *The difference function S and the projection \mathbf{f} are as defined before. For a boundary point x_t such that $S(x_t) = 0$, let estimated gradient $\widetilde{\nabla S}(x_t)$ be as computed by Definition 2 with step size δ and sampling size B . Over the randomness of the sampled vectors $\{u_b\}_{b=1}^B$,*

$$\cos\langle \mathbb{E} \widetilde{\nabla S}(x_t), \nabla S(x_t) \rangle \geq \frac{\|\text{proj}_{\nabla \mathbf{f}(0)} \nabla S(x_t)\|_2}{\|\nabla S(x_t)\|_2} \cdot \left(1 - \frac{(m-1)^2 \delta^2}{8\alpha_1^2} \left(\frac{\delta \gamma^2}{\alpha_1} + \frac{\gamma}{\alpha_1} \sqrt{\frac{\sum_{i=2}^m \alpha_i^2}{m-1}} + \sqrt{\frac{1}{m-1}} 1.58 \beta_{\mathbf{f}} \right)^2 \right), \quad (6)$$

where

$$\gamma := \beta_{\mathbf{f}} + \frac{\beta_S (\max_{i \in [m]} \alpha_i + 1/2\delta\beta_{\mathbf{f}})^2}{\|\text{proj}_{\nabla \mathbf{f}(0)} \nabla S(x_t)\|_2}. \quad (7)$$

Proof of Theorem 3. We begin with an important lemma.

Lemma A.2. *We let*

$$w := \frac{1}{2} \delta \left(\beta_{\mathbf{f}} \|\nabla S(x_t)\|_2 + \beta_S \left(\|\nabla \mathbf{f}(0)\|_2 + \frac{1}{2} \delta \beta_{\mathbf{f}} \right)^2 \right). \quad (8)$$

On the point x_t such that $S(x_t) = 0$, for any $\delta > 0$ and unit vector $u \in \mathbb{R}^n$,

$$\begin{aligned} \langle \nabla S(x_t), \nabla \mathbf{f}(0) \cdot u \rangle > w &\implies \phi(x_t + \Delta \mathbf{f}(\delta u)) = 1, \\ \langle \nabla S(x_t), \nabla \mathbf{f}(0) \cdot u \rangle < -w &\implies \phi(x_t + \Delta \mathbf{f}(\delta u)) = -1. \end{aligned}$$

Proof of Lemma A.2. We prove the lemma by Taylor expansion and the smoothness condition on S and \mathbf{f} . First, from Taylor expansion on function $\Delta \mathbf{f}(\delta u)$ at the origin,

$$\Delta \mathbf{f}(\delta u) = \mathbf{f}(\delta u) - \mathbf{f}(0) = \nabla \mathbf{f}(0) \cdot (\delta u) + 1/2(\delta u)^\top \nabla^2 \mathbf{f}(\xi)(\delta u), \quad (9)$$

where ξ is a point on the segment between the origin and (δu) . Since \mathbf{f} is $\beta_{\mathbf{f}}$ -smooth, $\|1/2(\delta u)^\top \nabla^2 \mathbf{f}(\xi)(\delta u)\|_2 \leq 1/2\beta_{\mathbf{f}}\delta^2$. Thus,

$$\langle \nabla S(x_t), \Delta \mathbf{f}(\delta u) \rangle \in \delta \langle \nabla S(x_t), \nabla \mathbf{f}(0) \cdot u \rangle \pm 1/2\delta^2 \|\nabla S(x_t)\|_2 \beta_{\mathbf{f}}.$$

Also we have

$$\|\Delta \mathbf{f}(\delta u)\|_2 \leq \|\nabla \mathbf{f}(0) \cdot (\delta u)\|_2 + \|1/2(\delta u)^\top \nabla^2 \mathbf{f}(\xi)(\delta u)\|_2 \leq \delta \|\nabla \mathbf{f}(0)\|_2 + 1/2\beta_{\mathbf{f}}\delta^2.$$

Easily seen, this also applies to any point ξ' between the origin and (δu) . Now, we apply Taylor expansion on function $S(x_t + \Delta \mathbf{f}(\delta u))$ at point x_t , and get

$$\begin{aligned} S(x_t + \Delta \mathbf{f}(\delta u)) &= \overbrace{S(x_t)}^0 + \langle \nabla S(x_t), \Delta \mathbf{f}(\delta u) \rangle + 1/2(\Delta \mathbf{f}(\xi'))^\top \nabla^2 S(x_t)(\Delta \mathbf{f}(\xi')) \\ &\in \delta \langle \nabla S(x_t), \nabla \mathbf{f}(0) \cdot u \rangle \pm 1/2\delta^2 \|\nabla S(x_t)\|_2 \beta_{\mathbf{f}} \pm 1/2\beta_S (\delta \|\nabla \mathbf{f}(0)\|_2 + 1/2\beta_{\mathbf{f}}\delta^2)^2 \\ &= \delta \left(\langle \nabla S(x_t), \nabla \mathbf{f}(0) \cdot u \rangle \pm 1/2\delta \left(\|\nabla S(x_t)\|_2 \beta_{\mathbf{f}} + \beta_S (\|\nabla \mathbf{f}(0)\|_2 + 1/2\delta\beta_{\mathbf{f}})^2 \right) \right) \\ &= \delta (\langle \nabla S(x_t), \nabla \mathbf{f}(0) \cdot u \rangle \pm w). \end{aligned}$$

Since the step size $\delta > 0$,

$$\begin{aligned} \langle \nabla S(x_t), \nabla \mathbf{f}(0) \cdot u \rangle > w &\implies S(x_t + \Delta \mathbf{f}(\delta u)) > 0, \\ \langle \nabla S(x_t), \nabla \mathbf{f}(0) \cdot u \rangle < -w &\implies S(x_t + \Delta \mathbf{f}(\delta u)) < 0. \end{aligned}$$

Observing that ϕ is the sign function of S according to Definition 1, we conclude the proof. \square

Remark. This lemma shows the connection between the value of sign function and the direction alignment between $\nabla \mathbf{f}(0) \cdot u$ and the true gradient.

Then, we study the distribution of $\nabla \mathbf{f}(0) \cdot u$.

Lemma A.3.

$$\langle \nabla S(x_t), \nabla \mathbf{f}(0) \cdot u \rangle \sim \alpha_1 \|\text{proj}_{\nabla \mathbf{f}(0)} \nabla S(x_t)\|_2 \left(2\text{Beta}\left(\frac{m-1}{2}, \frac{m-1}{2}\right) - 1 \right). \quad (10)$$

Meanwhile, for any $c \in [-\|\nabla S(x_t)\|_2, \|\nabla S(x_t)\|_2]$,

$$\mathbb{E}[\nabla \mathbf{f}(0) \cdot u \mid \langle \nabla S(x_t), \nabla \mathbf{f}(0) \cdot u \rangle = c] = c \frac{\text{proj}_{\nabla \mathbf{f}(0)} \nabla S(x_t)}{\|\text{proj}_{\nabla \mathbf{f}(0)} \nabla S(x_t)\|_2^2}. \quad (11)$$

Proof of Lemma A.3. According to Lemma 4.1, $\nabla \mathbf{f}(0) = \mathbf{U}\Sigma\mathbf{V}^\top$. Since \mathbf{V} is an orthonormal basis of \mathbb{R}^m , and u is uniformly sampled from the uniform sphere S^{m-1} , we let $v = \mathbf{V}^\top u$ and $v \sim \text{Unif}(S^{m-1})$ too. Then,

$$\begin{aligned} \langle \nabla S(x_t), \nabla \mathbf{f}(0) \cdot u \rangle &= \langle \nabla S(x_t), \mathbf{U}\Sigma v \rangle = \left\langle \nabla S(x_t), \sum_{i=1}^m \alpha_i v_i \mathbf{U}_{:,i} \right\rangle \\ &= \alpha_1 v_1 \|\text{proj}_{\nabla \mathbf{f}(0)} \nabla S(x_t)\|_2 \left\langle \frac{\text{proj}_{\nabla \mathbf{f}(0)} \nabla S(x_t)}{\|\text{proj}_{\nabla \mathbf{f}(0)} \nabla S(x_t)\|_2}, \mathbf{U}_{:,1} \right\rangle \stackrel{(*)}{=} \pm \alpha_1 v_1 \|\text{proj}_{\nabla \mathbf{f}(0)} \nabla S(x_t)\|_2, \end{aligned} \quad (12)$$

where $(*)$ follows from \mathbf{U} is an orthogonal basis with $\mathbf{U}_{:,1} = \pm \nabla \text{proj}_{\nabla \mathbf{f}(0)} S(x_t) / \|\text{proj}_{\nabla \mathbf{f}(0)} \nabla S(x_t)\|_2$ as Lemma 4.1 shows.

From (Yang et al., 2020) (Lemma I.23), $\frac{1+v_1}{2} \sim \text{Beta}\left(\frac{m-1}{2}, \frac{m-1}{2}\right)$, where $\text{Beta}(\cdot, \cdot)$ stands for the Beta distribution. As the result,

$$\alpha_1 v_1 \|\text{proj}_{\nabla \mathbf{f}(0)} \nabla S(x_t)\|_2 \sim \alpha_1 \|\text{proj}_{\nabla \mathbf{f}(0)} \nabla S(x_t)\|_2 \left(2\text{Beta}\left(\frac{m-1}{2}, \frac{m-1}{2}\right) - 1 \right).$$

Observing that this is a symmetric distribution centered at 0, we have

$$\langle \nabla S(x_t), \nabla \mathbf{f}(0) \cdot u \rangle \sim \alpha_1 \|\text{proj}_{\nabla \mathbf{f}(0)} \nabla S(x_t)\|_2 \left(2\text{Beta}\left(\frac{m-1}{2}, \frac{m-1}{2}\right) - 1 \right),$$

which proves the first part of the lemma.

For the second part, hereinafter, we condition the distribution of u on $\langle \nabla S(x_t), \nabla \mathbf{f}(0) \cdot u \rangle = c$. According to Eq. (12), the condition means that

$$v_1 = c_1 := \frac{c}{\alpha_1 \|\text{proj}_{\nabla \mathbf{f}(0)} \nabla S(x_t)\|_2} \left\langle \frac{\text{proj}_{\nabla \mathbf{f}(0)} \nabla S(x_t)}{\|\text{proj}_{\nabla \mathbf{f}(0)} \nabla S(x_t)\|_2}, \mathbf{U}_{:,1} \right\rangle.$$

Here we define the constant c_1 . Since $v \sim \text{Unif}(S^{m-1})$, it means that under this condition, $v' = (v_2, v_3, \dots, v_m)$ is uniformly sampled from the $(m-1)$ -dimension hypersphere with radius $r = \sqrt{1 - c_1^2}$. Therefore,

$$\begin{aligned} \mathbb{E}[\nabla \mathbf{f}(0) \cdot u \mid \langle \nabla S(x_t), \nabla \mathbf{f}(0) \cdot u \rangle = c] &= \mathbb{E}[\mathbf{U} \Sigma v \mid v_1 = c_1] \\ &= \mathbb{E} \left[\alpha_1 v_1 \mathbf{U}_{:,1} + \sum_{i=2}^m \alpha_i v_i \mathbf{U}_{:,i} \mid v_1 = c_1 \right] = \alpha_1 c_1 \mathbf{U}_{:,1} + \sum_{i=2}^m \mathbb{E}[\alpha_i v_i \mathbf{U}_{:,i} \mid v_1 = c_1] \\ &= c \frac{\text{proj}_{\nabla \mathbf{f}(0)} \nabla S(x_t)}{\|\text{proj}_{\nabla \mathbf{f}(0)} \nabla S(x_t)\|_2^2} + \sum_{i=2}^m \alpha_i \mathbf{U}_{:,i} \cdot \mathbb{E}[v_i \mid v_1 = c_1]. \end{aligned} \quad (13)$$

Since under this condition, $v' = (v_2, \dots, v_m)$ is uniformly sampled from a hypersphere centered at the origin (with radius r), we have $\mathbb{E}[v_i \mid v_1 = c_1] = 0$ for $i \geq 2$ by the symmetry of Beta distribution. Thus,

$$\mathbb{E}[\nabla \mathbf{f}(0) \cdot u \mid \langle \nabla S(x_t), \nabla \mathbf{f}(0) \cdot u \rangle = c] = c \frac{\text{proj}_{\nabla \mathbf{f}(0)} \nabla S(x_t)}{\|\text{proj}_{\nabla \mathbf{f}(0)} \nabla S(x_t)\|_2^2}.$$

□

Remark. The lemma considers the distribution of sampled vector u after the transformation by \mathbf{f} approximated in the first-order. The first equation of the lemma, Eq. (10), reveals the distribution of the projection (dot product) onto the true gradient direction. The distribution is a linearly scaled Beta distribution. The second equation of the lemma, Eq. (11), reveals that the sampled vector is *unbiased* on any direction orthogonal to the true gradient, i.e., conditioned on the same projected length on the true gradient direction, the expectation of the sampled vector aligns with the projected true gradient direction without any directional bias.

According to Lemma 4.1, we write $\nabla \mathbf{f}(0) = \mathbf{U} \Sigma \mathbf{V}^\top$. For notation simplicity, we let $\widehat{\text{proj}_{\nabla \mathbf{f}(0)} \nabla S(x_t)}$ denote the normalized true gradient: $\widehat{\text{proj}_{\nabla \mathbf{f}(0)} \nabla S(x_t)} := \text{proj}_{\nabla \mathbf{f}(0)} \nabla S(x_t) / \|\text{proj}_{\nabla \mathbf{f}(0)} \nabla S(x_t)\|_2$. Furthermore, we let $s := \langle \widehat{\text{proj}_{\nabla \mathbf{f}(0)} \nabla S(x_t)}, \mathbf{U}_{:,1} \rangle \in \{\pm 1\}$ denote the sign between these two aligned vectors.

With respect to the randomness of $u \sim \text{Unif}(S^{m-1})$, we denote v to $\mathbf{V}^\top u \sim \text{Unif}(S^{m-1})$, and we define the following three events E^- , E^o , and E^+ :

$$E^- : \langle \nabla S(x_t), \nabla \mathbf{f}(0) \cdot u \rangle \in (-\infty, -w), \quad (14)$$

$$E^o : \langle \nabla S(x_t), \nabla \mathbf{f}(0) \cdot u \rangle \in [-w, +w], \quad (15)$$

$$E^+ : \langle \nabla S(x_t), \nabla \mathbf{f}(0) \cdot u \rangle \in (+w, +\infty). \quad (16)$$

From Lemma A.3, we denote p to $\Pr[E^o]$, and by the symmetry of Beta distribution, $\Pr[E^-] = \Pr[E^+] = (1-p)/2$. From Eq. (12), we know $\langle \nabla S(x_t), \nabla \mathbf{f}(0) \cdot u \rangle = \alpha_1 \|\text{proj}_{\nabla \mathbf{f}(0)} \nabla S(x_t)\|_2 v_1$. Therefore, with events E^- and E^+ , $|v_1| > \frac{w}{\alpha_1 \|\text{proj}_{\nabla \mathbf{f}(0)} \nabla S(x_t)\|_2}$ while the signs of v_1 are different between the two events; and with event E^o , $|v_1| \leq \frac{w}{\alpha_1 \|\text{proj}_{\nabla \mathbf{f}(0)} \nabla S(x_t)\|_2}$.

According to the definition of the gradient estimator in Definition 2, we have $\widehat{\nabla S}(x_t) = \mathbb{E}[\phi(x_t + \Delta \mathbf{f}(\delta u)) \Delta \mathbf{f}(\delta u)]$. According to Eq. (9), for any unit vector u ,

$$\phi(x_t + \Delta \mathbf{f}(\delta u)) \Delta \mathbf{f}(\delta u) = \phi(x_t + \Delta \mathbf{f}(\delta u)) (\delta \nabla \mathbf{f}(0) \cdot u + \xi_{\delta u}) = \delta \phi(x_t + \Delta \mathbf{f}(\delta u)) \nabla \mathbf{f}(0) \cdot u + \xi'_{\delta u}$$

where $\xi_{\delta u}$ and $\xi'_{\delta u}$ are vectors depended by δu with length $\leq 1/2\beta_f\delta^2$. Therefore,

$$\|\mathbb{E}\widetilde{\nabla S}(x_t) - \delta\mathbb{E}[\phi(x_t + \nabla \mathbf{f}(\delta u))\nabla \mathbf{f}(0) \cdot u]\|_2 \leq 1/2\beta_f\delta^2. \quad (17)$$

Now, we inspect $\mathbb{E}[\phi(x_t + \nabla \mathbf{f}(\delta u))\nabla \mathbf{f}(0) \cdot u]$:

$$\mathbb{E}[\phi(x_t + \nabla \mathbf{f}(\delta u))\nabla \mathbf{f}(0) \cdot u] = \overbrace{p\mathbb{E}[\phi(x_t + \nabla \mathbf{f}(\delta u))\nabla \mathbf{f}(0) \cdot u \mid E^o]}^{(*)} + \overbrace{\frac{1-p}{2}(\mathbb{E}[-\nabla \mathbf{f}(0) \cdot u \mid E^-] + \mathbb{E}[\nabla \mathbf{f}(0) \cdot u \mid E^+])}^{(**)}. \quad (18)$$

According to Lemma A.3 (Eq. (11)),

$$\mathbb{E}[\nabla \mathbf{f}(0) \cdot u \mid E^+] = \mathbb{E}[|v_1| \mid E^+] \alpha_1 \widehat{\text{proj}_{\nabla \mathbf{f}(0)} \nabla S}(x_t), \quad \mathbb{E}[\nabla \mathbf{f}(0) \cdot u \mid E^-] = \mathbb{E}[-|v_1| \mid E^-] \alpha_1 \widehat{\text{proj}_{\nabla \mathbf{f}(0)} \nabla S}(x_t).$$

By symmetry of Beta distribution, $\mathbb{E}[|v_1| \mid E^+] = \mathbb{E}[|v_1| \mid E^-]$, and

$$(**) = \frac{1-p}{2}(\mathbb{E}[-\nabla \mathbf{f}(0) \cdot u \mid E^-] + \mathbb{E}[\nabla \mathbf{f}(0) \cdot u \mid E^+]) = (1-p)\alpha_1 \mathbb{E}[|v_1| \mid E^+] \widehat{\text{proj}_{\nabla \mathbf{f}(0)} \nabla S}(x_t).$$

For (*), we notice that

$$\begin{aligned} \mathbb{E}[\phi(x_t + \nabla \mathbf{f}(\delta u))\nabla \mathbf{f}(0) \cdot u \mid E^o] &\stackrel{\text{Eq. 13}}{=} \mathbb{E}\left[\phi(x_t + \nabla \mathbf{f}(\delta u)) \left(\alpha_1 v_1 s \cdot \widehat{\text{proj}_{\nabla \mathbf{f}(0)} \nabla S}(x_t) + \sum_{i=2}^m \alpha_i v_i \mathbf{U}_{:,i} \right) \mid E^o\right] \\ &= \alpha_1 s \mathbb{E}[\phi(x_t + \nabla \mathbf{f}(\delta u))v_1 \mid E^o] \widehat{\text{proj}_{\nabla \mathbf{f}(0)} \nabla S}(x_t) + \sum_{i=2}^m \alpha_i \mathbb{E}[\phi(x_t + \nabla \mathbf{f}(\delta u))v_i \mid E^o] \mathbf{U}_{:,i}. \end{aligned}$$

Combining them with Eq. (18), we have

$$\begin{aligned} \mathbb{E}[\phi(x_t + \nabla \mathbf{f}(\delta u))\nabla \mathbf{f}(0) \cdot u] &= \alpha_1 (ps\mathbb{E}[\phi(x_t + \nabla \mathbf{f}(\delta u))v_1 \mid E^o] + (1-p)\mathbb{E}[|v_1| \mid E^+]) \widehat{\text{proj}_{\nabla \mathbf{f}(0)} \nabla S}(x_t) \\ &\quad + p \sum_{i=2}^m \alpha_i \mathbb{E}[\phi(x_t + \nabla \mathbf{f}(\delta u))v_i \mid E^o] \mathbf{U}_{:,i}. \end{aligned}$$

We notice that $\{\widehat{\text{proj}_{\nabla \mathbf{f}(0)} \nabla S}(x_t), \mathbf{U}_{:,2}, \dots, \mathbf{U}_{:,m}\}$ is an orthogonal basis of \mathbb{R}^n . Thus,

$$\begin{aligned} &\left\| \mathbb{E}[\phi(x_t + \nabla \mathbf{f}(\delta u))\nabla \mathbf{f}(0) \cdot u] - \alpha_1 \mathbb{E}[|v_1|] \widehat{\text{proj}_{\nabla \mathbf{f}(0)} \nabla S}(x_t) \right\|_2 \\ &= \left\| \alpha_1 (ps\mathbb{E}[\phi(x_t + \nabla \mathbf{f}(\delta u))v_1 \mid E^o] + (1-p)\mathbb{E}[|v_1| \mid E^+] - \mathbb{E}[|v_1|]) \widehat{\text{proj}_{\nabla \mathbf{f}(0)} \nabla S}(x_t) \right. \\ &\quad \left. + p \sum_{i=2}^m \alpha_i \mathbb{E}[\phi(x_t + \nabla \mathbf{f}(\delta u))v_i \mid E^o] \mathbf{U}_{:,i} \right\|_2 \\ &= \sqrt{\underbrace{\alpha_1^2 (ps\mathbb{E}[\phi(x_t + \nabla \mathbf{f}(\delta u))v_1 \mid E^o] + (1-p)\mathbb{E}[|v_1| \mid E^+] - \mathbb{E}[|v_1|])^2}_{(I)} + \underbrace{\sum_{i=2}^m \alpha_i^2 p^2 \mathbb{E}[\phi(x_t + \nabla \mathbf{f}(\delta u))v_i \mid E^o]^2}_{(II)}}. \end{aligned}$$

We bound the two terms (I) and (II) individually. For the first term, we notice that

$$\begin{aligned} &|ps\mathbb{E}[\phi(x_t + \nabla \mathbf{f}(\delta u))v_1 \mid E^o] + (1-p)\mathbb{E}[|v_1| \mid E^+] - \mathbb{E}[|v_1|]| \\ &\leq p|\mathbb{E}[\phi(x_t + \nabla \mathbf{f}(\delta u))v_1 \mid E^o]| + |(1-p)\mathbb{E}[|v_1| \mid E^+] - (1-p)\mathbb{E}[|v_1| \mid E^+]| \\ &\leq p\mathbb{E}[|v_1| \mid E^o] + p\mathbb{E}[|v_1| \mid E^o] = 2p\mathbb{E}[|v_1| \mid E^o] \leq \frac{2pw}{\alpha_1 \|\widehat{\text{proj}_{\nabla \mathbf{f}(0)} \nabla S}(x_t)\|_2}. \end{aligned}$$

For the second term, we have

$$(II) = p^2 \sum_{i=2}^m \alpha_i^2 \mathbb{E}[\phi(x_t + \nabla \mathbf{f}(\delta u))v_i \mid E^o]^2 \leq p^2 \sum_{i=2}^m \alpha_i^2 \mathbb{E}[v_i^2 \mid E^o] \leq p^2 \sum_{i=2}^m \alpha_i^2 \mathbb{E}[v_i^2 \mid E^o].$$

Since $v = (v_1, v_2, \dots, v_m)^\top$ is uniformly sampled from S^{m-1} , conditioned on every sampled v_1 , the vector $(v_2, \dots, v_m)^\top$ is uniformly sampled from the $\sqrt{1 - v_1^2} S^{m-2}$. We let $v' = (v'_2, \dots, v'_m)^\top$ be uniformly sampled from S^{m-2} . Thus, for every sampled v_1 , we always have $\mathbb{E}[v_i^2 | v_1] \leq \mathbb{E}[v_i'^2]$ because v' is sampled from a larger hypersphere. By stacking all sampled v_1 's that forms the event E^o , we have (II) $\leq p^2 \sum_{i=2}^m \alpha_i^2 \mathbb{E}[v_i'^2]$. According to (Yang et al., 2020), $\frac{1+v'_i}{2} \sim \text{Beta}(\frac{m}{2} - 1, \frac{m}{2} - 1)$, whose variance $\text{Var}\left(\frac{1+v'_i}{2}\right) = \frac{1}{4(m-1)}$. Since $\text{Var}\left(\frac{1+v'_i}{2}\right) = \mathbb{E}\left[\left(\frac{1+v'_i}{2}\right)^2\right] - \mathbb{E}\left[\frac{1+v'_i}{2}\right]^2 = \frac{1}{4} \mathbb{E}[v_i'^2]$, we have $\mathbb{E}[v_i'^2] = \frac{1}{m-1}$. Thus,

$$(II) \leq p^2 \sum_{i=2}^m \alpha_i^2 \mathbb{E}[v_i'^2] = \frac{1}{m-1} p^2 \sum_{i=2}^m \alpha_i^2.$$

As a result,

$$\|\mathbb{E}[\phi(x_t + \Delta \mathbf{f}(\delta u)) \nabla \mathbf{f}(0) \cdot u] - \alpha_1 \mathbb{E}[|v_1|] \widehat{\text{proj}_{\nabla \mathbf{f}(0)} \nabla S(x_t)}\|_2 \leq \sqrt{\frac{4p^2 w^2}{\|\text{proj}_{\nabla \mathbf{f}(0)} \nabla S(x_t)\|_2^2} + \frac{p^2 \sum_{i=2}^m \alpha_i^2}{m-1}}. \quad (19)$$

Combining Eq. (19) with Eq. (17), we have

$$\|\mathbb{E} \widetilde{\nabla S}(x_t) - \delta \alpha_1 \mathbb{E}[|v_1|] \widehat{\text{proj}_{\nabla \mathbf{f}(0)} \nabla S(x_t)}\|_2 \leq p \delta \sqrt{\frac{4w^2}{\|\text{proj}_{\nabla \mathbf{f}(0)} \nabla S(x_t)\|_2^2} + \frac{\sum_{i=2}^m \alpha_i^2}{m-1}} + \frac{1}{2} \beta_{\mathbf{f}} \delta^2. \quad (20)$$

It means

$$\begin{aligned} & \cos \langle \mathbb{E} \widetilde{\nabla S}(x_t), \text{proj}_{\nabla \mathbf{f}(0)} \nabla S(x_t) \rangle \\ &= \cos \langle \mathbb{E} \widetilde{\nabla S}(x_t), \delta \alpha_1 \mathbb{E}[|v_1|] \widehat{\text{proj}_{\nabla \mathbf{f}(0)} \nabla S(x_t)} \rangle \\ &\geq 1 - \frac{1}{2} \left(\frac{p \delta \sqrt{\frac{4w^2}{\|\text{proj}_{\nabla \mathbf{f}(0)} \nabla S(x_t)\|_2^2} + \frac{\sum_{i=2}^m \alpha_i^2}{m-1}} + \frac{1}{2} \beta_{\mathbf{f}} \delta^2}{\delta \alpha_1 \mathbb{E}[|v_1|]} \right)^2 \\ &\geq 1 - \frac{1}{2} \left(\frac{2pw}{\alpha_1 \mathbb{E}[|v_1|] \|\text{proj}_{\nabla \mathbf{f}(0)} \nabla S(x_t)\|_2} + \frac{p}{\alpha_1 \mathbb{E}[|v_1|]} \sqrt{\frac{\sum_{i=2}^m \alpha_i^2}{m-1}} + \frac{\delta \beta_{\mathbf{f}}}{2\alpha_1 \mathbb{E}[|v_1|]} \right)^2. \end{aligned} \quad (21)$$

To this point, we need to unfold p and $\mathbb{E}[|v_1|]$. From the definition of event E^o (Eq. (15)),

$$p = \Pr \left[-w/(\alpha_1 \|\text{proj}_{\nabla \mathbf{f}(0)} \nabla S(x_t)\|_2) \leq v_1 \leq w/(\alpha_1 \|\text{proj}_{\nabla \mathbf{f}(0)} \nabla S(x_t)\|_2) \right] = \Pr \left[v_1^2 \leq w^2/(\alpha_1^2 \|\text{proj}_{\nabla \mathbf{f}(0)} \nabla S(x_t)\|_2^2) \right],$$

where $v_1^2 \sim \text{Beta}(1/2, (m-1)/2)$ (Chen et al., 2020). Thus, let $B(\cdot, \cdot)$ be the Beta function,

$$p = \int_0^{\frac{w^2}{\alpha_1^2 \|\text{proj}_{\nabla \mathbf{f}(0)} \nabla S(x_t)\|_2^2}} \frac{x^{-1/2} (1-x)^{\frac{m-3}{2}}}{B(\frac{1}{2}, \frac{m-1}{2})} dx \leq \frac{2w}{B(\frac{1}{2}, \frac{m-1}{2}) \alpha_1 \|\text{proj}_{\nabla \mathbf{f}(0)} \nabla S(x_t)\|_2}. \quad (22)$$

Also, from (Li et al., 2021) (Lemma 1), we have

$$\mathbb{E}[|v_1|] = 2 \int_0^1 \frac{x(1-x^2)^{\frac{m-3}{2}}}{B(\frac{1}{2}, \frac{m-1}{2})} dx = \frac{2}{(m-1) \cdot B(\frac{1}{2}, \frac{m-1}{2})}. \quad (23)$$

Plugging them into Eq. (21):

$$\begin{aligned} & \cos \langle \mathbb{E} \widetilde{\nabla S}(x_t), \text{proj}_{\nabla \mathbf{f}(0)} \nabla S(x_t) \rangle \geq \\ & 1 - \frac{1}{2} \left(\frac{m-1}{\alpha_1^2 \|\text{proj}_{\nabla \mathbf{f}(0)} \nabla S(x_t)\|_2} \left(\frac{2w^2}{\|\text{proj}_{\nabla \mathbf{f}(0)} \nabla S(x_t)\|_2} + w \sqrt{\frac{\sum_{i=2}^m \alpha_i^2}{m-1}} \right) + \frac{\delta \beta_{\mathbf{f}} (m-1) B(\frac{1}{2}, \frac{m-1}{2})}{4\alpha_1} \right)^2. \end{aligned} \quad (24)$$

We apply Stirling's approximation with error bound to $(m-1)B(\frac{1}{2}, \frac{m-1}{2})$:

$$\sqrt{2\pi(m-1)} \leq (m-1)B\left(\frac{1}{2}, \frac{m-1}{2}\right) \leq 1.26\sqrt{2\pi(m-1)} \text{ for all } m \geq 1,$$

and plug w (Eq. (8)) in (we also replace $\|\nabla \mathbf{f}(0)\|_2$ by $\max_{i \in [m]} \alpha_i$):

$$\begin{aligned} & \cos\langle \mathbb{E} \widetilde{\nabla S}(x_t), \text{proj}_{\nabla \mathbf{f}(0)} \nabla S(x_t) \rangle \\ & \geq 1 - \frac{1}{2} \left(\frac{m-1}{\alpha_1^2 \|\text{proj}_{\nabla \mathbf{f}(0)} \nabla S(x_t)\|_2} \left(\frac{2w^2}{\|\text{proj}_{\nabla \mathbf{f}(0)} \nabla S(x_t)\|_2} + w \sqrt{\frac{\sum_{i=2}^m \alpha_i^2}{m-1}} \right) + 0.315 \sqrt{2\pi(m-1)} \frac{\delta \beta_{\mathbf{f}}}{\alpha_1} \right)^2 \\ & = 1 - \frac{(m-1)^2 \delta^2}{8\alpha_1^2} \left(\frac{\delta}{\alpha_1} \left(\frac{\beta_{\mathbf{f}} \|\text{proj}_{\nabla \mathbf{f}(0)} \nabla S(x_t)\|_2 + \beta_S (\max_{i \in [m]} \alpha_i + 1/2 \delta \beta_{\mathbf{f}})^2}{\|\text{proj}_{\nabla \mathbf{f}(0)} \nabla S(x_t)\|_2} \right)^2 \right. \\ & \quad \left. + \frac{1}{\alpha_1} \sqrt{\frac{\sum_{i=2}^m \alpha_i^2}{m-1}} \frac{\beta_{\mathbf{f}} \|\text{proj}_{\nabla \mathbf{f}(0)} \nabla S(x_t)\|_2 + \beta_S (\max_{i \in [m]} \alpha_i + 1/2 \delta \beta_{\mathbf{f}})^2}{\|\text{proj}_{\nabla \mathbf{f}(0)} \nabla S(x_t)\|_2} + 0.63 \sqrt{\frac{2\pi}{m-1}} \beta_{\mathbf{f}} \right)^2 \\ & \geq 1 - \frac{(m-1)^2 \delta^2}{8\alpha_1^2} \left(\frac{\delta \gamma^2}{\alpha_1} + \frac{\gamma}{\alpha_1} \sqrt{\frac{\sum_{i=2}^m \alpha_i^2}{m-1}} + \sqrt{\frac{1}{m-1}} 1.58 \beta_{\mathbf{f}} \right)^2. \end{aligned} \quad (25)$$

According to Lemma A.1, we have

$$\cos\langle \mathbb{E} \widetilde{\nabla S}(x_t), \nabla S(x_t) \rangle \geq \frac{\|\text{proj}_{\nabla \mathbf{f}(0)} \nabla S(x_t)\|_2}{\|\nabla S(x_t)\|_2} \cdot \left(1 - \frac{(m-1)^2 \delta^2}{8\alpha_1^2} \left(\frac{\delta \gamma^2}{\alpha_1} + \frac{\gamma}{\alpha_1} \sqrt{\frac{\sum_{i=2}^m \alpha_i^2}{m-1}} + \sqrt{\frac{1}{m-1}} 1.58 \beta_{\mathbf{f}} \right)^2 \right). \quad (26)$$

□

A.5. Warmup: Concentration Bound at Boundary

Now we consider the concentration bound for the boundary point gradient estimation.

Theorem 4 (Concentration of cosine similarity; at boundary). *Under the same setting as Theorem 3, over the randomness of the sampled vector $\{u_b\}_{i=1}^B$, with probability $1 - p$,*

$$\begin{aligned} & \cos\langle \widetilde{\nabla S}(x_t), \nabla S(x_t) \rangle \\ & \geq \frac{\|\text{proj}_{\nabla \mathbf{f}(0)} \nabla S(x_t)\|_2}{\|\nabla S(x_t)\|_2} \cdot \left(1 - \frac{(m-1)^2 \delta^2}{8\alpha_1^2} \left(\frac{\delta \gamma^2}{\alpha_1} + \frac{\gamma}{\alpha_1} \sqrt{\frac{\sum_{i=2}^m \alpha_i^2}{m-1}} + \frac{1.58 \beta_{\mathbf{f}} + \frac{1}{\delta} \sqrt{\sum_{i=1}^m \alpha_i^2} \cdot \sqrt{\frac{2}{B} \ln(\frac{m}{\epsilon})}}{\sqrt{m-1}} \right)^2 \right), \end{aligned} \quad (27)$$

where

$$\gamma := \beta_{\mathbf{f}} + \frac{\beta_S (\max_{i \in [m]} \alpha_i + 1/2 \delta \beta_{\mathbf{f}})^2}{\|\nabla S(x_t)\|_2}. \quad (28)$$

Proof of Theorem 4. The key idea for the proof is to bound the ℓ_2 distance from the estimated gradient vector to the expectation of the estimated gradient vector via concentration bounds. Then, the bound is combined to the proof of Theorem 3, concretely, Eq. (19), to derive the required result.

In the proof, to distinguish the “ p ” in probability bound from the definition in Eq. (15), we change this variable to “ ϵ ”, i.e., the bound reads “with probability $1 - \epsilon, \dots$ ”.

We note that the gradient estimator per Definition 2 is

$$\widetilde{\nabla S}(x_t) = \frac{1}{B} \sum_{b=1}^B \phi(x_t + \Delta \mathbf{f}(\delta u_b)) \Delta \mathbf{f}(\delta u_b)$$

where $u_b \sim \text{Unif}(S^{m-1})$. Thus, let $u \sim \text{Unif}(S^{m-1})$,

$$\begin{aligned} & \left\| \widetilde{\nabla S}(x_t) - \delta \mathbb{E} [\phi(x_t + \Delta \mathbf{f}(\delta u)) \nabla \mathbf{f}(0) \cdot u] \right\|_2 \\ \stackrel{(i.)}{=} & \left\| \frac{1}{B} \sum_{b=1}^B \phi(x_t + \Delta \mathbf{f}(\delta u_b)) \nabla \mathbf{f}(0) \cdot (\delta u_b) + \frac{1}{B} \sum_{b=1}^B \xi_{\delta u_b} - \delta \mathbb{E} [\phi(x_t + \Delta \mathbf{f}(\delta u)) \nabla \mathbf{f}(0) \cdot u] \right\|_2 \\ \leq & 1/2 \beta_{\mathbf{f}} \delta^2 + \delta \left\| \frac{1}{B} \sum_{b=1}^B \phi(x_t + \Delta \mathbf{f}(\delta u_b)) \nabla \mathbf{f}(0) \cdot u_b - \mathbb{E} [\phi(x_t + \Delta \mathbf{f}(\delta u)) \nabla \mathbf{f}(0) \cdot u] \right\|_2 \\ = & 1/2 \beta_{\mathbf{f}} \delta^2 + \delta \left\| \frac{1}{B} \sum_{b=1}^B \phi(x_t + \Delta \mathbf{f}(\delta u_b)) \mathbf{U} \Sigma v_b - \mathbb{E} [\phi(x_t + \Delta \mathbf{f}(\delta u)) \mathbf{U} \Sigma v] \right\|_2 \quad (\text{Lemma 4.1, } v = \mathbf{V}^\top u) \\ = & 1/2 \beta_{\mathbf{f}} \delta^2 + \delta \left\| \frac{1}{B} \sum_{b=1}^B \sum_{i=1}^m \phi(x_t + \Delta \mathbf{f}(\delta u_b)) \mathbf{U}_{:,i} \alpha_i v_{b,i} - \sum_{i=1}^m \mathbb{E} [\phi(x_t + \Delta \mathbf{f}(\delta u)) \mathbf{U}_{:,i} \alpha_i v_i] \right\|_2 \\ = & 1/2 \beta_{\mathbf{f}} \delta^2 + \delta \left\| \sum_{i=1}^m \alpha_i \mathbf{U}_{:,i} \left(\frac{1}{B} \sum_{b=1}^B \phi(x_t + \Delta \mathbf{f}(\delta u_b)) v_{b,i} - \mathbb{E} [\phi(x_t + \Delta \mathbf{f}(\delta u)) v_i] \right) \right\|_2 \\ \stackrel{(ii.)}{=} & 1/2 \beta_{\mathbf{f}} \delta^2 + \delta \sqrt{\sum_{i=1}^m \alpha_i^2 \left(\frac{1}{B} \sum_{b=1}^B \phi(x_t + \Delta \mathbf{f}(\delta u_b)) v_{b,i} - \mathbb{E} [\phi(x_t + \Delta \mathbf{f}(\delta u)) v_i] \right)^2}. \end{aligned}$$

In (i.), $\|\xi_{\delta u_b}\|_2 \leq 1/2 \beta_{\mathbf{f}} \delta^2$ from Taylor expansion as in Eq. (12). In (ii.), $\mathbf{U}_{:,i}$'s are orthogonal basis vectors.

For each i , since the $\phi(x_t + \Delta \mathbf{f}(\delta u_b)) v_{b,i}$'s for different b 's are independent, and within range $[-1, 1]$, we apply Hoeffding's inequality and yield

$$\Pr \left[\left| \frac{1}{B} \sum_{b=1}^B \phi(x_t + \Delta \mathbf{f}(\delta u_b)) v_{b,i} - \mathbb{E} [\phi(x_t + \Delta \mathbf{f}(\delta u)) v_i] \right| \leq \sqrt{\frac{2}{B} \ln \left(\frac{m}{\epsilon} \right)} \right] \geq 1 - \frac{\epsilon}{m}.$$

From union bound, with probability $1 - \epsilon$, for any $i \in [m]$, we have

$$\left| \frac{1}{B} \sum_{b=1}^B \phi(x_t + \Delta \mathbf{f}(\delta u_b)) v_{b,i} - \mathbb{E} [\phi(x_t + \Delta \mathbf{f}(\delta u)) v_i] \right| \leq \sqrt{\frac{2}{B} \ln \left(\frac{m}{\epsilon} \right)}.$$

Under this condition, we have

$$\left\| \widetilde{\nabla S}(x_t) - \delta \mathbb{E} [\phi(x_t + \Delta \mathbf{f}(\delta u)) \nabla \mathbf{f}(0) \cdot u] \right\|_2 \leq 1/2 \beta_{\mathbf{f}} \delta^2 + \delta \sqrt{\sum_{i=1}^m \alpha_i^2} \cdot \sqrt{\frac{2}{B} \ln \left(\frac{m}{\epsilon} \right)}. \quad (29)$$

Note that a tighter concentration may be achieved by replacing the Hoeffding's inequality by other tailored tail bounds for Beta-distributed v_i 's. But due to the uncertainty brought by the sign term $\phi(\cdot)$, it is challenging. On the other hand, for these i.i.d. random variable's concentration, the Hoeffding's inequality is tight in terms of orders due to central limit theorem.

Now, we combine Eq. (29) with Eq. (19) and get

$$\left\| \widetilde{\nabla S}(x_t) - \delta \alpha_1 \mathbb{E} [\|v_1\| \overline{\text{proj}_{\nabla \mathbf{f}(0)} \nabla S(x_t)}] \right\|_2 \leq p \delta \sqrt{\frac{4w^2}{\|\text{proj}_{\nabla \mathbf{f}(0)} \nabla S(x_t)\|_2^2}} + \frac{\sum_{i=2}^m \alpha_i^2}{m-1} + \delta \sqrt{\sum_{i=1}^m \alpha_i^2} \cdot \sqrt{\frac{2}{B} \ln \left(\frac{m}{\epsilon} \right)} + 1/2 \beta_{\mathbf{f}} \delta^2, \quad (30)$$

where $\widehat{\nabla S}$ is the normalized tue gradient, $p := \Pr[E^o]$, and E^o is as defined in Eq. (15). Similar as Eq. (21):

$$\cos\langle \widehat{\nabla S}(x_t), \text{proj}_{\nabla \mathbf{f}(0)} \nabla S(x_t) \rangle \geq 1 - \frac{1}{2} \left(\frac{p\delta \sqrt{\frac{4w^2}{\|\text{proj}_{\nabla \mathbf{f}(0)} \nabla S(x_t)\|_2^2} + \frac{\sum_{i=2}^m \alpha_i^2}{m-1}} + \delta \sqrt{\sum_{i=1}^m \alpha_i^2} \cdot \sqrt{\frac{2}{B} \ln\left(\frac{m}{\epsilon}\right)} + \frac{1}{2} \beta_{\mathbf{f}} \delta^2}{\delta \alpha_1 \mathbb{E}[\|v_1\|]} \right)^2.$$

Following the similar process as in the proof of Theorem 3, we get

$$\begin{aligned} & \cos\langle \widehat{\nabla S}(x_t), \nabla S(x_t) \rangle \\ & \geq \frac{\|\text{proj}_{\nabla \mathbf{f}(0)} \nabla S(x_t)\|_2}{\|\nabla S(x_t)\|_2} \cdot \left(1 - \frac{(m-1)^2 \delta^2}{8\alpha_1^2} \left(\frac{\delta \gamma^2}{\alpha_1} + \frac{\gamma}{\alpha_1} \sqrt{\frac{\sum_{i=2}^m \alpha_i^2}{m-1}} + \frac{1.58\beta_{\mathbf{f}} + \frac{1}{\delta} \sqrt{\sum_{i=1}^m \alpha_i^2} \cdot \sqrt{\frac{2}{B} \ln\left(\frac{m}{\epsilon}\right)}}{\sqrt{m-1}} \right)^2 \right). \end{aligned} \quad (31)$$

A.6. Main Result: Expectation Bound Near Boundary (Theorem 1)

Theorem 1 (Expected cosine similarity; approaching boundary). *The difference function S and the projection \mathbf{f} are as defined before. For a point x_t that is θ -close to the boundary, i.e., there exists $\theta' \in [-\theta, \theta]$ such that $S(x_t + \theta' \nabla S(x_t) / \|\nabla S(x_t)\|_2) = 0$, let estimated gradient $\widehat{\nabla S}(x_t)$ be as computed by Definition 2 with step size δ and sampling size B . Over the randomness of the sampled vectors $\{u_b\}_{b=1}^B$,*

$$\begin{aligned} \cos\langle \widehat{\nabla S}(x_t), \nabla S(x_t) \rangle & \geq \frac{\|\text{proj}_{\nabla \mathbf{f}(0)} \nabla S(x_t)\|_2}{\|\nabla S(x_t)\|_2} \cdot \\ & \left(1 - \frac{(m-1)^2 \delta^2}{8\alpha_1^2} \left(\frac{\delta \gamma^2}{\alpha_1} + \frac{\gamma}{\alpha_1} \sqrt{\frac{\sum_{i=2}^m \alpha_i^2}{m-1}} + \frac{1.58\beta_{\mathbf{f}}}{\sqrt{m-1}} + \frac{\gamma \theta}{\alpha_1 \delta} \cdot \frac{\|\nabla S(x_t)\|_2}{\|\text{proj}_{\nabla \mathbf{f}(0)} \nabla S(x_t)\|_2} \right)^2 \right), \end{aligned} \quad (32)$$

where

$$\gamma := \beta_{\mathbf{f}} + \frac{\beta_S (\max_{i \in [m]} \alpha_i + 1/2\delta\beta_{\mathbf{f}})^2 + \beta_S \theta^2 / \delta^2}{\|\text{proj}_{\nabla \mathbf{f}(0)} \nabla S(x_t)\|_2}. \quad (33)$$

Proof of Theorem 1. The high-level idea is similar to the proof of Theorem 3: we build the connection between $\langle \nabla S(x_t), \nabla \mathbf{f}(0) \cdot u \rangle$ and $\phi(x_t + \Delta \mathbf{f}(\delta u))$. Then, due to the unbiased sampling, the expectation of estimated gradient is close to the true gradient direction with bounded error.

For simplicity, from the symmetry and monotonicity, we let $\theta' = \theta$, i.e., $S(x_t + \theta \nabla S(x_t) / \|\nabla S(x_t)\|_2) = 0$.

Lemma A.4. *We let*

$$w := \frac{1}{2} \delta \left(\beta_{\mathbf{f}} \|\nabla S(x_t)\|_2 + \beta_S \left(\|\nabla \mathbf{f}(0)\|_2 + \frac{1}{2} \delta \beta_{\mathbf{f}} \right)^2 \right) + \frac{\beta_S \theta^2}{2\delta}. \quad (34)$$

On the point x_t such that $S(x_t + \theta \nabla S(x_t) / \|\nabla S(x_t)\|_2) = 0$, for any $\delta > 0$ and unit vector $u \in \mathbb{R}^n$,

$$\begin{aligned} \langle \nabla S(x_t), \nabla \mathbf{f}(0) \cdot u \rangle & > w + \frac{\theta \|\nabla S(x_t)\|_2}{\delta} \implies \phi(x_t + \Delta \mathbf{f}(\delta u)) = 1, \\ \langle \nabla S(x_t), \nabla \mathbf{f}(0) \cdot u \rangle & < -w + \frac{\theta \|\nabla S(x_t)\|_2}{\delta} \implies \phi(x_t + \Delta \mathbf{f}(\delta u)) = -1. \end{aligned}$$

Proof of Lemma A.4. We do Taylor expansion on $S(x_t + \Delta \mathbf{f}(\delta u))$ at point x_t :

$$S(x_t + \Delta \mathbf{f}(\delta u)) \in S(x_t) + \delta \left(\langle \nabla S(x_t), \nabla \mathbf{f}(0) \cdot u \rangle \pm 1/2\delta \left(\|\nabla S(x_t)\|_2 \beta_{\mathbf{f}} + \beta_S (\|\nabla \mathbf{f}(0)\|_2 + 1/2\delta\beta_{\mathbf{f}})^2 \right) \right).$$

Notice that $S(x_t + \theta \nabla S(x_t) / \|\nabla S(x_t)\|_2)$ can also be expanded at point x_t :

$$0 = S(x_t + \theta \nabla S(x_t) / \|\nabla S(x_t)\|_2) \in S(x_t) + \theta \|\nabla S(x_t)\|_2 \pm \frac{1}{2} \beta_S \theta^2,$$

i.e.,

$$S(x_t) \in -\theta \|\nabla S(x_t)\|_2 \pm \frac{1}{2} \beta_S \theta^2.$$

Therefore,

$$S(x_t + \Delta \mathbf{f}(\delta u)) \in \delta \left(\langle \nabla S(x_t), \nabla \mathbf{f}(0) \cdot u \rangle - \frac{\theta \|\nabla S(x_t)\|_2}{\delta} \pm \frac{1}{2} \delta \left(\|\nabla S(x_t)\|_2 \beta_{\mathbf{f}} + \beta_S \left(\|\nabla \mathbf{f}(0)\|_2 + \frac{1}{2} \delta \beta_{\mathbf{f}} \right)^2 \right) \pm \frac{\beta_S \theta^2}{2\delta} \right).$$

Noticing that $\phi(x_t + \Delta \mathbf{f}(\delta u)) = \text{sgn}(S(x_t + \Delta \mathbf{f}(\delta u)))$, we conclude the proof. \square

According to Lemma 4.1, we write $\Delta \mathbf{f}(0) = \mathbf{U} \Sigma \mathbf{V}^\top$. We let $\widehat{\nabla S}(x_t)$ denote the normalized true gradient: $\widehat{\nabla S}(x_t) := \nabla S(x_t) / \|\nabla S(x_t)\|_2$. Furthermore, we define $s := \langle \widehat{\nabla S}(x_t), \mathbf{U}_{:,1} \rangle \in \{\pm 1\}$, which is the sign between these two aligned vectors.

With respect to the randomness of $u \sim \text{Unif}(S^{m-1})$, we let v denote $\mathbf{V}^\top u \sim \text{Unif}(S^{m-1})$, and we define the following three events E^- , E^o , and E^+ with probability p^- , p^o and p^+ respectively:

$$E^- : \langle \nabla S(x_t), \nabla \mathbf{f}(0) \cdot u \rangle \in (-\infty, -w + \theta \|\nabla S(x_t)\|_2 / \delta), \quad p^- := \Pr[E^-] \quad (35)$$

$$E^o : \langle \nabla S(x_t), \nabla \mathbf{f}(0) \cdot u \rangle \in [-w + \theta \|\nabla S(x_t)\|_2 / \delta, +w + \theta \|\nabla S(x_t)\|_2 / \delta], \quad p^o := \Pr[E^o] \quad (36)$$

$$E^+ : \langle \nabla S(x_t), \nabla \mathbf{f}(0) \cdot u \rangle \in (+w + \theta \|\nabla S(x_t)\|_2 / \delta, +\infty). \quad p^+ := \Pr[E^+] \quad (37)$$

We notice that Lemma A.3 still holds since u is still uniformly sampled from hypersphere S^{m-1} and Lemma 4.1 still holds for $\nabla \mathbf{f}(0)$. Thus,

$$\langle \nabla S(x_t), \nabla \mathbf{f}(0) \cdot u \rangle = \alpha_1 \|\text{proj}_{\nabla \mathbf{f}(0)} \nabla S(x_t)\|_2 s v_1.$$

And with event E^o , we have

$$|v_1| \leq \frac{w}{\alpha_1 \|\text{proj}_{\nabla \mathbf{f}(0)} \nabla S(x_t)\|_2} + \frac{\theta}{\alpha_1 \delta} \cdot \frac{\|\nabla S(x_t)\|_2}{\|\text{proj}_{\nabla \mathbf{f}(0)} \nabla S(x_t)\|_2}. \quad (38)$$

Now, we can start to bound the error between expectation of estimated gradient and a scaled true gradient. As the first step, according to Eq. (17), we have

$$\|\mathbb{E} \widehat{\nabla S}(x_t) - \delta \mathbb{E}[\phi(x_t + \Delta \mathbf{f}(\delta u)) \nabla \mathbf{f}(0) \cdot u]\|_2 \leq \frac{1}{2} \beta_{\mathbf{f}} \delta^2. \quad (39)$$

Then we decompose $\mathbb{E}[\phi(x_t + \Delta \mathbf{f}(\delta u)) \nabla \mathbf{f}(0) \cdot u]$ to connect it with the (projected) true gradient:

$$\begin{aligned} & \mathbb{E}[\phi(x_t + \Delta \mathbf{f}(\delta u)) \nabla \mathbf{f}(0) \cdot u] \\ &= p^o \mathbb{E}[\phi(x_t + \Delta \mathbf{f}(\delta u)) \nabla \mathbf{f}(0) \cdot u \mid E^o] + p^+ \mathbb{E}[\nabla \mathbf{f}(0) \cdot u \mid E^+] + p^- \mathbb{E}[-\nabla \mathbf{f}(0) \cdot u \mid E^-] \\ &= p^o \sum_{i=1}^m \alpha_i \mathbb{E}[\phi(x_t + \Delta \mathbf{f}(\delta u)) v_i \mid E^o] \mathbf{U}_{:,i} + p^+ \alpha_1 \widehat{\text{proj}_{\nabla \mathbf{f}(0)} \nabla S(x_t) s \mathbb{E}[v_1 \mid E^+]} + p^- \alpha_1 \widehat{\text{proj}_{\nabla \mathbf{f}(0)} \nabla S(x_t) s \mathbb{E}[-v_1 \mid E^-]} \\ &= \alpha_1 s (p^o \mathbb{E}[\phi(x_t + \Delta \mathbf{f}(\delta u)) v_1 \mid E^o] + p^+ \mathbb{E}[v_1 \mid E^+] + p^- \mathbb{E}[-v_1 \mid E^-]) \widehat{\text{proj}_{\nabla \mathbf{f}(0)} \nabla S(x_t)} \\ & \quad + p^o \sum_{i=2}^m \alpha_i \mathbb{E}[\phi(x_t + \Delta \mathbf{f}(\delta u)) v_i \mid E^o] \mathbf{U}_{:,i}. \end{aligned} \quad (40)$$

We notice that

$$|s (p^o \mathbb{E}[\phi(x_t + \Delta \mathbf{f}(\delta u)) v_1 \mid E^o] + p^+ \mathbb{E}[v_1 \mid E^+] + p^- \mathbb{E}[-v_1 \mid E^-]) - \mathbb{E}[|v_1|]|$$

$$\begin{aligned}
 &= p^o \mathbb{E}[\phi(x_t + \Delta \mathbf{f}(\delta u))v_1 - |v_1| \mid E^o] \leq 2p^o \mathbb{E}[|v_1| \mid E^o] \\
 &\leq 2p^o \left(\frac{w}{\alpha_1 \|\text{proj}_{\nabla \mathbf{f}(0)} \nabla S(x_t)\|_2} + \frac{\theta}{\alpha_1 \delta} \cdot \frac{\|\nabla S(x_t)\|_2}{\|\text{proj}_{\nabla \mathbf{f}(0)} \nabla S(x_t)\|_2} \right). \tag{Eq. (38)}
 \end{aligned}$$

For any $i \geq 2$, we define a new vector $v' = (v'_2, v'_3, \dots, v'_m) \sim \text{Unif}(S^{m-2})$. Thus,

$$\mathbb{E}[\phi(x_t + \Delta \mathbf{f}(\delta u))v_i \mid E^o] \leq \mathbb{E}[|v_i| \mid E^o] \leq \mathbb{E}[|v'_i|].$$

Combining the above equations to Eq. (40), we get

$$\begin{aligned}
 &\left\| \mathbb{E}[\phi(x_t + \Delta \mathbf{f}(\delta u)) \nabla \mathbf{f}(0) \cdot u] - \alpha_1 \mathbb{E}[|v_1|] \widehat{\text{proj}_{\nabla \mathbf{f}(0)} \nabla S(x_t)} \right\|_2 \\
 &\leq \sqrt{4\alpha_1^2 (p^o)^2 \left(\frac{w}{\alpha_1 \|\text{proj}_{\nabla \mathbf{f}(0)} \nabla S(x_t)\|_2} + \frac{\theta}{\alpha_1 \delta} \cdot \frac{\|\nabla S(x_t)\|_2}{\|\text{proj}_{\nabla \mathbf{f}(0)} \nabla S(x_t)\|_2} \right)^2 + (p^o)^2 \sum_{i=2}^m \alpha_i^2 \mathbb{E}[|v'_i|]^2} \\
 &\leq p^o \sqrt{4\alpha_1^2 \left(\frac{w}{\alpha_1 \|\text{proj}_{\nabla \mathbf{f}(0)} \nabla S(x_t)\|_2} + \frac{\theta}{\alpha_1 \delta} \cdot \frac{\|\nabla S(x_t)\|_2}{\|\text{proj}_{\nabla \mathbf{f}(0)} \nabla S(x_t)\|_2} \right)^2 + \sum_{i=2}^m \frac{\alpha_i^2}{m-1}}. \tag{41}
 \end{aligned}$$

Combining with Eq. (39):

$$\begin{aligned}
 &\left\| \mathbb{E} \widetilde{\nabla S(x_t)} - \delta \alpha_1 \mathbb{E}[|v_1|] \widehat{\text{proj}_{\nabla \mathbf{f}(0)} \nabla S(x_t)} \right\|_2 \\
 &\leq \delta p^o \sqrt{4\alpha_1^2 \left(\frac{w}{\alpha_1 \|\text{proj}_{\nabla \mathbf{f}(0)} \nabla S(x_t)\|_2} + \frac{\theta}{\alpha_1 \delta} \cdot \frac{\|\nabla S(x_t)\|_2}{\|\text{proj}_{\nabla \mathbf{f}(0)} \nabla S(x_t)\|_2} \right)^2 + \sum_{i=2}^m \frac{\alpha_i^2}{m-1} + \frac{1}{2} \beta_{\mathbf{f}} \delta^2}. \tag{42}
 \end{aligned}$$

Thus,

$$\begin{aligned}
 &\cos \langle \mathbb{E} \widetilde{\nabla S(x_t)}, \text{proj}_{\nabla \mathbf{f}(0)} \nabla S(x_t) \rangle \\
 &\geq 1 - \frac{1}{2} \left(\frac{2p^o w}{\alpha_1 \mathbb{E}[|v_1|] \|\text{proj}_{\nabla \mathbf{f}(0)} \nabla S(x_t)\|_2} + \frac{2p^o \theta}{\alpha_1 \delta \mathbb{E}[|v_1|]} \cdot \frac{\|\nabla S(x_t)\|_2}{\|\text{proj}_{\nabla \mathbf{f}(0)} \nabla S(x_t)\|_2} + \frac{p^o}{\alpha_1 \mathbb{E}[|v_1|]} \sqrt{\frac{\sum_{i=2}^m \alpha_i^2}{m-1}} + \frac{\delta \beta_{\mathbf{f}}}{2\alpha_1 \mathbb{E}[|v_1|]} \right)^2. \tag{43}
 \end{aligned}$$

We notice that v_1 is distributed around 0 with symmetry and concentration, so

$$\begin{aligned}
 p^o &= \Pr[E^o] = \Pr \left[sv_1 \in \left[-\frac{w}{\alpha_1 \|\text{proj}_{\nabla \mathbf{f}(0)} \nabla S(x_t)\|_2} + \frac{\theta}{\alpha_1 \delta} \cdot \frac{\|\nabla S(x_t)\|_2}{\|\text{proj}_{\nabla \mathbf{f}(0)} \nabla S(x_t)\|_2}, \right. \right. \\
 &\quad \left. \left. \frac{w}{\alpha_1 \|\text{proj}_{\nabla \mathbf{f}(0)} \nabla S(x_t)\|_2} + \frac{\theta}{\alpha_1 \delta} \cdot \frac{\|\nabla S(x_t)\|_2}{\|\text{proj}_{\nabla \mathbf{f}(0)} \nabla S(x_t)\|_2} \right] \right] \\
 &\leq \Pr \left[v_1^2 \leq \frac{w^2}{\alpha_1^2 \|\text{proj}_{\nabla \mathbf{f}(0)} \nabla S(x_t)\|_2^2} \right] \stackrel{\text{Eq. 22}}{\leq} \frac{2w}{B(\frac{1}{2}, \frac{m-1}{2}) \alpha_1 \|\text{proj}_{\nabla \mathbf{f}(0)} \nabla S(x_t)\|_2}.
 \end{aligned}$$

And from Eq. (23),

$$\mathbb{E}[|v_1|] = \frac{2}{(m-1) \cdot B(\frac{1}{2}, \frac{m-1}{2})}.$$

Insert them into Eq. (43), we get

$$\begin{aligned}
 \cos \langle \mathbb{E} \widetilde{\nabla S(x_t)}, \nabla S(x_t) \rangle &\geq \frac{\|\text{proj}_{\nabla \mathbf{f}(0)} \nabla S(x_t)\|_2}{\|\nabla S(x_t)\|_2} \\
 &\quad \left(1 - \frac{(m-1)^2 \delta^2}{8\alpha_1^2} \left(\frac{\delta \gamma^2}{\alpha_1} + \frac{\gamma}{\alpha_1} \sqrt{\frac{\sum_{i=2}^m \alpha_i^2}{m-1}} + \frac{\gamma \theta}{\alpha_1 \delta} \cdot \frac{\|\nabla S(x_t)\|_2}{\|\text{proj}_{\nabla \mathbf{f}(0)} \nabla S(x_t)\|_2} + \frac{1.58 \beta_{\mathbf{f}}}{\sqrt{m-1}} \right)^2 \right), \tag{44}
 \end{aligned}$$

□

A.7. Main Result: Concentration Bound Near Boundary (Theorem 2)

Theorem 2 (Concentration of cosine similarity; approaching boundary). *Under the same setting as Theorem 1, over the randomness of the sampled vector $\{u_b\}_{b=1}^B$, with probability $1 - p$, Under the same setting as Theorem 1, over the randomness of the sampled vector $\{u_b\}_{b=1}^B$, with probability $1 - p$,*

$$\cos\langle \widetilde{\nabla S}(x_t), \nabla S(x_t) \rangle \geq \frac{\|\text{proj}_{\nabla f(0)} \nabla S(x_t)\|_2}{\|\nabla S(x_t)\|_2} \cdot \left(1 - \frac{(m-1)^2 \delta^2}{8\alpha_1^2} \left(\frac{\delta \gamma^2}{\alpha_1} + \frac{\gamma}{\alpha_1} \sqrt{\frac{\sum_{i=2}^m \alpha_i^2}{m-1}} + \frac{1.58\beta_f}{\sqrt{m-1}} + \frac{\gamma\theta}{\alpha_1\delta} \cdot \frac{\|\nabla S(x_t)\|_2}{\|\text{proj}_{\nabla f(0)} \nabla S(x_t)\|_2} + \frac{\frac{1}{\delta} \sqrt{\sum_{i=1}^m \alpha_i^2} \cdot \sqrt{\frac{2}{B} \ln(\frac{m}{p})}}{\sqrt{m-1}} \right)^2 \right), \quad (45)$$

where

$$\gamma := \beta_f + \frac{\beta_S (\max_{i \in [m]} \alpha_i + 1/2\delta\beta_f)^2 + \beta_S \theta^2 / \delta^2}{\|\text{proj}_{\nabla f(0)} \nabla S(x_t)\|_2}. \quad (46)$$

Proof of Theorem 2. The proof follows the similar way as how we extend Theorem 3 to Theorem 4.

Similar as the proof in Theorem 4, by applying Hoeffding bound, with probability $1 - \epsilon$,

$$\|\widetilde{\nabla S}(x_t) - \delta \mathbb{E}[\phi(x_t + \Delta f(\delta u)) \nabla f(0) \cdot u]\|_2 \leq 1/2\beta_f \delta^2 + \delta \sqrt{\sum_{i=1}^m \alpha_i^2} \cdot \sqrt{\frac{2}{B} \ln\left(\frac{m}{\epsilon}\right)}.$$

When this holds, combining it with Eq. (41), we get

$$\begin{aligned} & \|\widetilde{\nabla S}(x_t) - \delta \mathbb{E}[\phi(x_t + \Delta f(\delta u)) \nabla f(0) \cdot u]\|_2 \\ & \leq \frac{1}{2}\beta_f \delta^2 + \delta \sqrt{\sum_{i=1}^m \alpha_i^2} \cdot \sqrt{\frac{2}{B} \ln\left(\frac{m}{\epsilon}\right)} + \delta p^o \sqrt{4\alpha_1^2 \left(\frac{w}{\alpha_1 \|\text{proj}_{\nabla f(0)} \nabla S(x_t)\|_2} + \frac{\theta}{\alpha_1 \delta} \cdot \frac{\|\nabla S(x_t)\|_2}{\|\text{proj}_{\nabla f(0)} \nabla S(x_t)\|_2} \right)^2 + \sum_{i=2}^m \frac{\alpha_i^2}{m-1}}, \end{aligned}$$

where p^o is as defined in Eq. (36). Thus,

$$\begin{aligned} & \cos\langle \widetilde{\nabla S}(x_t), \text{proj}_{\nabla f(0)} \nabla S(x_t) \rangle \\ & \geq 1 - \frac{1}{2} \left(\frac{2p^o w}{\alpha_1 \mathbb{E}[\|v_1\|] \|\text{proj}_{\nabla f(0)} \nabla S(x_t)\|_2} + \frac{2p^o \theta}{\alpha_1 \delta \mathbb{E}[\|v_1\|]} \cdot \frac{\|\nabla S(x_t)\|_2}{\|\text{proj}_{\nabla f(0)} \nabla S(x_t)\|_2} \right. \\ & \quad \left. + \frac{p^o}{\alpha_1 \mathbb{E}[\|v_1\|]} \sqrt{\frac{\sum_{i=2}^m \alpha_i^2}{m-1}} + \frac{\delta \beta_f}{2\alpha_1 \mathbb{E}[\|v_1\|]} + \frac{\sqrt{\sum_{i=1}^m \alpha_i^2} \cdot \sqrt{\frac{2}{B} \ln\left(\frac{m}{\epsilon}\right)}}{\alpha_1 \mathbb{E}[\|v_1\|]} \right)^2 \\ & \geq 1 - \frac{(m-1)^2 \delta^2}{8\alpha_1^2} \left(\frac{\delta \gamma^2}{\alpha_1} + \frac{\gamma}{\alpha_1} \sqrt{\frac{\sum_{i=2}^m \alpha_i^2}{m-1}} + \frac{1.58\beta_f}{\sqrt{m-1}} + \frac{\gamma\theta}{\alpha_1\delta} \cdot \frac{\|\nabla S(x_t)\|_2}{\|\text{proj}_{\nabla f(0)} \nabla S(x_t)\|_2} + \frac{\frac{1}{\delta} \sqrt{\sum_{i=1}^m \alpha_i^2} \cdot \sqrt{\frac{2}{B} \ln\left(\frac{m}{\epsilon}\right)}}{\sqrt{m-1}} \right)^2. \end{aligned}$$

We conclude the proof by observing that

$$\cos\langle \widetilde{\nabla S}(x_t), \nabla S(x_t) \rangle = \frac{\|\text{proj}_{\nabla f(0)} \nabla S(x_t)\|_2}{\|\nabla S(x_t)\|_2} \cos\langle \widetilde{\nabla S}(x_t), \text{proj}_{\nabla f(0)} \nabla S(x_t) \rangle$$

from Lemma A.1. □

A.8. Bound in Big- \mathcal{O} Notation

We mainly simplify the bound in Theorems 1 and 2 by omitting the terms with smaller orders of m . In boundary attack, following HSJA (Chen et al., 2017), we set binary search precision $\theta = (m\sqrt{m})^{-1}$ and step size $\delta_t = \|x_t - x^*\|_2/m =$

$\Theta(1/m)$. Therefore, $\theta/\delta = \Theta(1/\sqrt{m})$. We first simplify γ in Theorems 1 and 2:

$$\begin{aligned}\gamma &= \beta_{\mathbf{f}} + \frac{\beta_S (\max_{i \in [m]} \alpha_i + 1/2\delta\beta_{\mathbf{f}})^2 + \beta_S \theta^2 / \delta^2}{\|\text{proj}_{\nabla \mathbf{f}(0)} \nabla S(x_t)\|_2} \\ &= \beta_{\mathbf{f}} + \frac{\beta_S (\max_{i \in [m]} \alpha_i + \Theta(\beta_{\mathbf{f}}/m))^2 + \beta_S \Theta(1/m)}{\|\text{proj}_{\nabla \mathbf{f}(0)} \nabla S(x_t)\|_2} = \beta_{\mathbf{f}} + \mathcal{O}\left(\frac{\beta_S \max_{i \in [m]} \alpha_i^2}{\|\text{proj}_{\nabla \mathbf{f}(0)} \nabla S(x_t)\|_2}\right).\end{aligned}$$

We plug in the γ into Theorem 2:

$$\begin{aligned}& \frac{\delta\gamma^2}{\alpha_1} + \frac{\gamma}{\alpha_1} \sqrt{\frac{\sum_{i=2}^m \alpha_i^2}{m-1}} + \frac{1.58\beta_{\mathbf{f}}}{\sqrt{m-1}} + \frac{\gamma\theta}{\alpha_1\delta} \cdot \frac{\|\nabla S(x_t)\|_2}{\|\text{proj}_{\nabla \mathbf{f}(0)} \nabla S(x_t)\|_2} + \frac{\frac{1}{\delta} \sqrt{\sum_{i=1}^m \alpha_i^2} \cdot \sqrt{\frac{2}{B} \ln\left(\frac{m}{p}\right)}}{\sqrt{m-1}} \\ &= \mathcal{O}\left(\frac{\beta_{\mathbf{f}}^2}{m\alpha_1}\right) + \mathcal{O}\left(\frac{\beta_S^2 \max_{i \in [m]} \alpha_i^4}{m\alpha_1 \|\text{proj}_{\nabla \mathbf{f}(0)} \nabla S(x_t)\|_2^2}\right) + \mathcal{O}\left(\frac{\beta_{\mathbf{f}}}{\alpha_1} \sqrt{\frac{\sum_{i=2}^m \alpha_i^2}{m-1}}\right) + \mathcal{O}\left(\frac{\beta_S \max_{i \in [m]} \alpha_i^2}{\alpha_1 \|\text{proj}_{\nabla \mathbf{f}(0)} \nabla S(x_t)\|_2} \sqrt{\frac{\sum_{i=2}^m \alpha_i^2}{m-1}}\right) \\ &+ \mathcal{O}\left(\frac{\beta_{\mathbf{f}}}{\sqrt{m}}\right) + \mathcal{O}\left(\frac{\beta_{\mathbf{f}} \|\nabla S(x_t)\|_2}{m\alpha_1}\right) + \mathcal{O}\left(\frac{\beta_S \max_{i \in [m]} \alpha_i^2 \|\nabla S(x_t)\|_2}{m\alpha_1 \|\text{proj}_{\nabla \mathbf{f}(0)} \nabla S(x_t)\|_2}\right) + \mathcal{O}\left(\frac{1}{\delta} \frac{\alpha_1 \sqrt{\frac{2}{B} \ln\left(\frac{m}{p}\right)}}{\sqrt{m-1}}\right) \\ &+ \mathcal{O}\left(\frac{1}{\delta} \sqrt{\frac{2}{B} \ln\left(\frac{m}{p}\right)} \cdot \sqrt{\frac{\sum_{i=2}^m \alpha_i^2}{m-1}}\right).\end{aligned}$$

We can discard all terms with negative order of m (since they will be negligible with respect to other terms when m is not too small) and get

$$\begin{aligned}& \frac{\delta\gamma^2}{\alpha_1} + \frac{\gamma}{\alpha_1} \sqrt{\frac{\sum_{i=2}^m \alpha_i^2}{m-1}} + \frac{1.58\beta_{\mathbf{f}}}{\sqrt{m-1}} + \frac{\gamma\theta}{\alpha_1\delta} \cdot \frac{\|\nabla S(x_t)\|_2}{\|\text{proj}_{\nabla \mathbf{f}(0)} \nabla S(x_t)\|_2} + \frac{\frac{1}{\delta} \sqrt{\sum_{i=1}^m \alpha_i^2} \cdot \sqrt{\frac{2}{B} \ln\left(\frac{m}{p}\right)}}{\sqrt{m-1}} \\ &= \mathcal{O}\left(\frac{\beta_{\mathbf{f}}}{\alpha_1} \sqrt{\frac{\sum_{i=2}^m \alpha_i^2}{m-1}}\right) + \mathcal{O}\left(\frac{\beta_S \max_{i \in [m]} \alpha_i^2}{\alpha_1 \|\text{proj}_{\nabla \mathbf{f}(0)} \nabla S(x_t)\|_2} \sqrt{\frac{\sum_{i=2}^m \alpha_i^2}{m-1}}\right) + \mathcal{O}\left(\frac{1}{\delta} \sqrt{\frac{2}{B} \ln\left(\frac{m}{p}\right)} \cdot \sqrt{\frac{\sum_{i=2}^m \alpha_i^2}{m-1}}\right).\end{aligned}$$

Therefore, the bound in Theorem 2 becomes:

$$\begin{aligned}& \cos\langle \mathbb{E} \widetilde{\nabla S}(x_t), \nabla S(x_t) \rangle \\ & \geq \frac{\|\text{proj}_{\nabla \mathbf{f}(0)} \nabla S(x_t)\|_2}{\|\nabla S(x_t)\|_2} \cdot \left(1 - \frac{(m-1)^2 \delta^2}{8\alpha_1^2} \left(\mathcal{O}\left(\frac{\beta_{\mathbf{f}}^2}{\alpha_1^2} \cdot \frac{\sum_{i=2}^m \alpha_i^2}{m-1}\right) + \mathcal{O}\left(\frac{\beta_S^2 \max_{i \in [m]} \alpha_i^4}{\alpha_1^2 \|\text{proj}_{\nabla \mathbf{f}(0)} \nabla S(x_t)\|_2^2} \cdot \frac{\sum_{i=2}^m \alpha_i^2}{m-1}\right) + \mathcal{O}\left(\frac{1}{\delta^2} \cdot \frac{2}{B} \ln\left(\frac{m}{p}\right) \cdot \frac{\sum_{i=2}^m \alpha_i^2}{m-1}\right) \right) \right) \\ &= \frac{\|\text{proj}_{\nabla \mathbf{f}(0)} \nabla S(x_t)\|_2}{\|\nabla S(x_t)\|_2} \cdot \left(1 - \mathcal{O}\left(m^2 \cdot \frac{\sum_{i=2}^m \alpha_i^2}{m-1} \left(\frac{\delta^2 \beta_{\mathbf{f}}^2}{\alpha_1^4} + \frac{\alpha_{\max}^4}{\alpha_1^4} \cdot \frac{\delta^2 \beta_S^2}{\|\text{proj}_{\nabla \mathbf{f}(0)} \nabla S(x_t)\|_2^2} + \frac{\ln\left(\frac{m}{p}\right)}{B\alpha_1}\right)\right)\right).\end{aligned}\quad (47)$$

It recovers the simplified bound in Fig. 3. Note the the last term $\frac{\ln(m/p)}{B\alpha_1}$ is the extra term of Theorem 2 that guarantees the $1-p$ holding probability, and discarding this term yields the version bound for the expectation bound (Theorem 1).

B. Discussion on Key Characteristics and Optimal Scale

This section illustrates the key characteristics for improving the gradient estimator, and discusses the existence of the optimal scale.

B.1. Illustration of Key Characteristics

The figure illustrates the key characteristics, or the optimization goals, for improving the projection-based gradient estimator as discussed in Section 4.1.

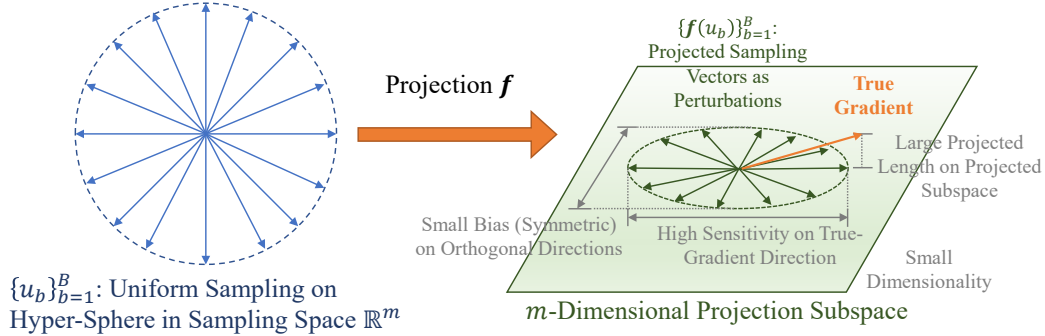


Figure 9. An illustration of key characteristics for a good projection-based gradient estimator.

B.2. Existence of Optimal Scale

As discussed in Section 4.2, the scale is mapped to the dimensionality of the projection subspace— m .

Due to the trade-off between large $\|\text{proj}_{\nabla f(0)} \nabla S(x_t)\|_2$ and small m , from Eq. (47), we can intuitively learn that for a given projection f , the optimal scale m_{opt} always exists. Now we define this formally. We first explicitly show that f relies on the dimensionality of the projection subspace. To do so, we use $f_m : \mathbb{R}^m \rightarrow \mathbb{R}^n$ instead of the general notion f . f_m can be viewed as being drawn from a pre-defined projection function family $\mathcal{F} = \{f_i : i \in [n]\}$. Then, the optimal scale m_{opt} can be then explicit expressed as such:

$$m_{\text{opt}} = \arg \max_{m \in [n]} \frac{\|\text{proj}_{\nabla f_m(0)} \nabla S(x_t)\|_2}{\|\nabla S(x_t)\|_2} \cdot \left(1 - \mathcal{O} \left(m^2 \cdot \frac{\sum_{i=2}^m \alpha_i^2}{m-1} \left(\frac{\delta^2 \beta_{f_m}^2}{\alpha_1^4} + \frac{\alpha_{\max}^4}{\alpha_1^4} \cdot \frac{\delta^2 \beta_S^2}{\|\text{proj}_{\nabla f_m(0)} \nabla S(x_t)\|_2^2} + \frac{\ln(\frac{m}{p})}{B\alpha_1} \right) \right) \right).$$

The objective function in above $\arg \max$ encodes the precise bound in Theorem 2.

A SIMPLIFIED FORM FOR LINEAR CASE

When both the projection function f_m and the difference function S are locally linear, i.e., $\beta_{f_m} = \beta_S = 0$, we can simplify the above equation as such:

$$m_{\text{opt}} = \arg \max_{m \in [n]} \frac{\|\text{proj}_{\nabla f_m(0)} \nabla S(x_t)\|_2}{\|\nabla S(x_t)\|_2} \left(1 - C m^2 \ln \left(\frac{m}{p} \right) \right),$$

where $0 < C < 1$ is a constant.

Now, the existence of optimal scale becomes more apparent. While increasing m can increase $\frac{\|\text{proj}_{\nabla f_m(0)} \nabla S(x_t)\|_2}{\|\nabla S(x_t)\|_2}$, this term has its upper bound 1. On the other hand, the $m^2 \ln(m/p)$ in the second term will also be increased, and it is unbounded. Therefore, an optimal m should be non-zero but not large, i.e., an optimal scale m_{opt} usually exists.

The optimal scale depends on the actual function family f_m and the difference function S . For common and practical cases, as shown in Fig. 4, the objective function for $\arg \max$ is usually unimodal so that the progressive scaling is guaranteed to find the optimal scale. We leave it as our future work to theoretically analyze on what cases this objective function is strictly unimodal.

C. Target Models

In this section, we introduce the target models used in the experiments including the implementation details and the target model performance.

C.1. Implementation Details

Offline Models. Following (Li et al., 2020a; 2021), the pretrained ResNet-18 models are used here as the target models. We also evaluate model ResNeXt50_32×4d (Xie et al., 2017) to demonstrate the generalization ability. For models that are

finetuned, cross entropy error is employed as the loss function and is implemented as `torch.nn.CrossEntropyLoss` in PyTorch.

For ImageNet, no finetuning is performed as the pretrained target model is just trained exactly on ImageNet. The model is loaded with PyTorch command `torchvision.models.resnet18(pretrained=True)` or `torchvision.models.resnext50_32x4d(pretrained=True)` following the documentation (PyTorch, 2020).

For CelebA, the target model is fine-tuned to do binary classification on image attributes. Among the 40 binary attributes associated with each image, the top-5 balanced attributes are ‘Attractive’, ‘Mouth_Slightly_Open’, ‘Smiling’, ‘Wearing_Lipstick’, ‘High_Cheekbones’. Though the ‘Attractive’ attribute is the most balanced one, however, it is more subjective than objective, thus we instead choose the second attribute ‘Mouth_Slightly_Open’.

For MNIST and CIFAR-10 datasets, we first resize the original images to 224×224 by linear interpolation, then the target model is finetuned to do 10-way classification. One reason for doing interpolation is that it can provide us more spatial scales to explore. The another reason is that the linear interpolation step also makes image sizes consistent among all the tasks and experiments.

Commercial Online API. Among all the APIs provided by the Face++ platform (MEGVII, 2020c), the ‘Compare’ API (MEGVII, 2020a) which takes two images as input and returns a confidence score indicating whether they contain the faces from the same person. This is also consistent with the same online attacking in (Li et al., 2020a; 2021). In implementation during the attack process, the two image arrays with floating number values are first converted to integers and stored as jpg images on disk. Then they are encoded as base64 binary data and sent as POST request to the request URL (MEGVII, 2020b). We set the similarity threshold as 50% in the experiments following (Li et al., 2020a; 2021): when the confidence score is equal to or larger than 50%, we consider the two faces to belong to the ‘same person’, vice versa.

For source-target images that are from two different persons, the goal of the attack is to get an adversarial image that looks like the target image (has low MSE between the adversarial image and target image), but is predicted as ‘same person’ with the source image. We randomly sample 50 source-target image pairs from the CelebA dataset that are predicted as different persons by the ‘Compare’ API. Then we apply the PSBA pipeline with various perturbation vector generators for comparison.

C.2. Performance of Target Models

The benign accuracy of the target models finetuned on different datasets is shown in Table 4.

Table 4. The benign model accuracy of the target models.

Model	MNIST	CelebA	CIFAR-10	ImageNet
ResNet-18	99.55%	93.77%	88.15%	69.76%
ResNeXt50_32×4d	99.33%	94.00%	90.26%	77.62%

D. Details on PSBA-PGAN

In this section, we introduce the details of Progressive-Scale based projection models including the architecture of Progressive GAN, the training procedure, the algorithm description for progressive scaling and gradient estimation, and the implementation details.

D.1. The Architecture of Progressive GAN

Progressive GAN is a method developed by Karras et. al. (Karras et al., 2018) allowing gradually generating the image from low resolution images to high resolution images. Here, we adopt the implementation of PGAN from pytorch_GAN_zoo (Research, 2020) to help us explore the influence of different scales on attacking performance.

The `Conv2d(n_kernel, n_stride, n_pad)` here applies He’s constant (He et al., 2015b) at runtime, and for simplicity, the `LeakyReLU(negative_slope = 0.2)` is denoted as LReLU. Besides, for the generator, we actually utilize bilinear interpolation to implement ‘Unsample’ and utilize average pool to implement ‘Downsample’. Then, the detailed model network structures

for the generator and discriminator with the maximum scale 224×224 are listed in Table 5 and Table 6.

Table 5. The detailed model structure for generator in PGAN.

Generator	Act	Output shape
Latent vector	-	$9408 \times 1 \times 1$
Fully-connected	LReLU	$8192 \times 1 \times 1$
Resize	-	$512 \times 4 \times 4$
Conv(3, 1, 1)	LReLU	$512 \times 4 \times 4$
Upsample	-	$512 \times 7 \times 7$
Conv(3, 1, 1)	LReLU	$256 \times 7 \times 7$
Conv(3, 1, 1)	LReLU	$256 \times 7 \times 7$
Upsample	-	$256 \times 14 \times 14$
Conv(3, 1, 1)	LReLU	$256 \times 14 \times 14$
Conv(3, 1, 1)	LReLU	$256 \times 14 \times 14$
Upsample	-	$256 \times 28 \times 28$
Conv(3, 1, 1)	LReLU	$128 \times 28 \times 28$
Conv(3, 1, 1)	LReLU	$128 \times 28 \times 28$
Upsample	-	$128 \times 56 \times 56$
Conv(3, 1, 1)	LReLU	$64 \times 56 \times 56$
Conv(3, 1, 1)	LReLU	$64 \times 56 \times 56$
Upsample	-	$64 \times 56 \times 56$
Conv(3, 1, 1)	LReLU	$32 \times 112 \times 112$
Conv(3, 1, 1)	LReLU	$32 \times 112 \times 112$
Upsample	-	$32 \times 224 \times 224$
Conv(3, 1, 1)	LReLU	$16 \times 224 \times 224$
Conv(3, 1, 1)	LReLU	$16 \times 224 \times 224$
Conv(1, 1, 0)	Tanh	$3 \times 224 \times 224$

D.2. Projection Model Training Procedure

First, we need to prepare the datasets for PGAN training, which comprise the gradient images generated from a set of *reference models*. Generally, the reference models are assumed to have *different structures* compared with the blackbox target model. Nonetheless, attacker-trained reference models can generate accessible gradients and provide valuable information on the distribution of the target model gradients.

In our case, with the same setting as in (Li et al., 2021), there are five reference models (i.e., DenseNet-121 (Huang et al., 2018), ResNet-50 (He et al., 2015a), VGG16 (Simonyan & Zisserman, 2015), GoogleNet (Szegedy et al., 2014) and WideResNet (Zagoruyko & Komodakis, 2017)) with different backbones compared with the target model, while the implementation and training details are similar with the target model in Section C.1. The benign test accuracy results of these five reference models for MNIST, CIFAR-10 and CelebA datasets are shown in Table 7. After the reference models are trained, their gradients with respect to the training data points are generated with PyTorch automatic differentiation function with command ‘loss.backward()’. The loss is the cross entropy between the prediction scores and the ground truth labels.

For ImageNet and CelebA, we randomly sample 500,000 gradient images (100,000 per reference model) for each of ImageNet and CelebA and fix them throughout the experiments for fair comparison.

For CIFAR-10 and MNIST, there are fewer images and so we use the whole dataset and generate 250,000 gradient images for CIFAR-10 (50,000 per reference model) and 300,000 (60,000 per reference model) gradient images for MNIST.

For AE and VAE, they are directly trained on the original gradient datasets, and the training details can be found in (Li et al., 2020a). However, for PGAN, since the size of the images from original gradient datasets is 224×224 , we down-scale them by average pool first and then as the new training datasets when the PGAN is trained to build the low resolution image. Actually, this training procedure is just the same as in (Karras et al., 2018), the only difference here is the so-called images are gradient images generated from reference models instead of the real-world pictures.

Table 6. The detailed model structure for discriminator in PGAN.

Discriminator	Act	Output shape
Input image	-	$3 \times 224 \times 224$
Conv(1, 1, 0)	-	$16 \times 224 \times 224$
Conv(3, 1, 1)	LReLU	$16 \times 224 \times 224$
Conv(3, 1, 1)	LReLU	$32 \times 224 \times 224$
Downsample	-	$32 \times 112 \times 112$
Conv(3, 1, 1)	LReLU	$32 \times 112 \times 112$
Conv(3, 1, 1)	LReLU	$64 \times 112 \times 112$
Downsample	-	$64 \times 56 \times 56$
Conv(3, 1, 1)	LReLU	$64 \times 56 \times 56$
Conv(3, 1, 1)	LReLU	$128 \times 56 \times 56$
Downsample	-	$128 \times 28 \times 28$
Conv(3, 1, 1)	LReLU	$128 \times 28 \times 28$
Conv(3, 1, 1)	LReLU	$256 \times 28 \times 28$
Downsample	-	$256 \times 14 \times 14$
Conv(3, 1, 1)	LReLU	$256 \times 7 \times 7$
Conv(3, 1, 1)	LReLU	$512 \times 7 \times 7$
Downsample	-	$512 \times 4 \times 4$
Minibatch stddev	-	$513 \times 4 \times 4$
Conv(3, 1, 1)	LReLU	$512 \times 4 \times 4$
Fully-connected	LReLU	$512 \times 1 \times 1$
Fully-connected	Linear	$1 \times 1 \times 1$

D.3. Reference Model Performance

Intuitively, with well-trained reference models that perform comparatively with the target models, the attacker can get gradient images that are in a more similar distribution with the target model’s gradients for training, thus increasing the chance of an attack with higher quality. The reference model performance in terms of prediction accuracy for MNIST, CIFAR-10, CelebA and ImageNet datasets are shown in Table 7. The model performance is comparable to that of the target models.

D.4. Algorithm Description

We provide the pseudocode for the progressive-scale process with the PSBA-PGAN in Algorithm 1 (once the optimal scale determined, it will be used across all the pairs of source and target images) and for frequency reduction gradient estimation with the PGAN224 in Algorithm 2.

D.5. Attack Implementation

The goal is to generate an adversarial image that looks similar as the target image, i.e., as close as to the target image, but is predicted as the label of the target image. We fix the random seed to 0 so that the samples are consistent across different runs and various methods to ensure reproducibility and to facilitate fair comparison.

 Table 7. The benign model accuracy of the reference models on four datasets. For the dataset MNIST and CIFAR10, the images are linearly interpolated to size 224×224 ; for the dataset CelebA, the attribute is chosen as ‘mouth_slightly_open’

Dataset	DenseNet-121	ResNet-50	VGG16	GoogleNet	WideResNet
MNIST	98.99%	99.43%	99.16%	99.46%	98.59%
CIFAR10	92.73%	88.47%	92.67%	92.26%	85.19%
CelebA	93.81%	94.02%	94.13%	91.77%	93.79%
ImageNet	74.65%	76.15%	71.59%	69.78%	78.51%

Algorithm 1 The Process for Searching the Optimal Scale for PSBA-PGAN.

Input: a validation set which comprises ten pairs of source-target images, the PGANs with different output scales, access to query the decision of target model.

Output: the optimal scale for attacking the target model.

```

1:  $optimal\_scale \leftarrow 7 \times 7$ 
2:  $lowest\_distance \leftarrow \infty$ 
3: for  $s = 7 \times 7$  to  $224 \times 224$  do
4:   Take the PGAN generator with output scale  $s$  as the gradient estimator to attack the target model.
5:    $current\_distance \leftarrow$  the MSE of the the ten adversarial images to the corresponding target images after 10 step attack. The number of sampled perturbation vectors per step is set to 100.
6:   if  $current\_distance \leq lowest\_distance$  then
7:      $lowest\_distance \leftarrow current\_distance$ 
8:      $optimal\_scale \leftarrow s$ 
9:   else
10:    return  $optimal\_scale$ 
11:   end if
12: end for
13: return  $optimal\_scale$ 

```

Algorithm 2 Frequency Reduction Gradient Estimation

Input: a data point on the decision boundary $x \in \mathbb{R}^m$, nonlinear projection function f , number of random sampling B , access to query the decision of target model $\phi(\cdot) = \text{sgn}(S(\cdot))$.

Output: the approximated gradient $\widehat{\nabla} S(x_{adv}^{(t)})$.

```

1: Sample  $B$  random Gaussian vectors of the lower dimension:  $v_b \in \mathbb{R}^n$ .
2: Use PGAN224 to project the random vectors to the gradient space:  $u_b = f(v_b) \in \mathbb{R}^m$ .
3: Do DCT transformation on each channel of  $u_b$  and get the frequency representation:  $d_b = \text{DCT}(u_b)$ 
4: Save the  $k \times k$  signals on the upper left corner and set other signals to zero :  $d'_b = \text{Filter}(d_b)$ 
5: Map the signals back to the original space by Inverse DCT transformation:  $u'_b = \text{IDCT}(d'_b)$ 
6: Get query points by adding perturbation vectors with the original point on the decision boundary  $x_{adv}^{(t)} + \delta u'_b$ .
7: Monte Carlo approximation for the gradient:
   
$$\widehat{\nabla} S(x_{adv}^{(t)}) = \frac{1}{B} \sum_{b=1}^B \phi \left( x_{adv}^{(t)} + \delta u'_b \right) u'_b = \frac{1}{B} \sum_{b=1}^B \text{sgn} \left( S \left( x_{adv}^{(t)} + \delta u'_b \right) \right) u'_b$$

8: return  $\widehat{\nabla} S(x_{adv}^{(t)})$ 

```

Gradient Estimation. For convenience and precision concern, we just use $\delta_t \mathbf{f}(u_b)$ instead of the theoretical representation $\Delta \mathbf{f}(\delta_t u_b)$, i.e., $\mathbf{f}(\delta_t u_b) - \mathbf{f}(0)$ in the actual calculation of estimated gradient $\nabla \widehat{S}(x_t)$ and the $\mathbf{f}(u_b)$ is normalized here. Besides, the variance reduction balancing adopted in (Chen et al., 2020) is also applied in our gradient estimation out of the concern for the accuracy of estimation.

Offline Models. During the attack, we randomly sample source-target pairs of images from each of the corresponding datasets. We query the offline models with the sampled images to make sure both source image and target image are predicted as their ground truth labels and the labels are different so that the attack is nontrivial. For the same dataset, the results of different attack methods are reported as the average of the same 50 randomly sampled pairs.

Online API. For the online API attacks, the source-target pairs are sampled from the dataset CelebA. The results of different attack methods are also reported as the average of the same 50 randomly sampled pairs.

E. Quantitative Results

E.1. Attack Setup

We randomly select 50 pairs of source and target images from test set that are predicted by the target model as different classes for both offline attack and online attack. The goal here is to move the source image gradually to the target image under the measure of MSE while maintaining being predicted as source label by the target model. In this process, the number of sampled perturbation vectors at each step (B in Definition 2) is controlled as 100 for every gradient generator in the Monte Carlo algorithm to estimate the gradient for fairness (except EA, in which the B is set to 1). The optimal dimensions chosen on the search space for EA are shown in Table 8, and other hyper-parameters are the same with the setting in (Dong et al., 2019).

Table 8. The optimal dimension of the search space for EA on different datasets and target models.

Model	MNIST	CIFAR-10	CelebA	ImageNet
ResNet-18	$30 \times 30 \times 1$	$30 \times 30 \times 3$	$112 \times 112 \times 3$	$30 \times 30 \times 3$
ResNeXt50_32x4d	$30 \times 30 \times 1$	$45 \times 45 \times 3$	$45 \times 45 \times 3$	$45 \times 45 \times 3$

E.2. Time and Resource Consumption

The optimal scale is usually small and relatively stable for an assigned dataset as shown in Appendix E.9. Indeed, from our experimental observation, it is enough to just use 10 scr-tgt image pairs to determine the optimal scale within 10 minutes on one 2080 Ti GPU. Besides, the model is trained before we start to attack, and the optimal scale is also determined before the attack. So in fact, no matter in the training or attacking stage, the time and resource consumption are almost the same with other generative model-based attacks (Li et al., 2021; Tu et al., 2020). The PGAN training time on scale 28×28 for ImageNet is about one day with two RTX 2080 Ti GPUs and that for the scale 224×224 is about two days. We note that the PGAN training can be done offline and is one-time training for attacking different models. Besides, the averaged attack time with 10,000 queries on ImageNet of HSJA is 114.2s, and that of PSBA is 136.4s. We remark that the bulk of PSBA attack time is on the resize operation similar to the baseline QEBA-S (see (Li et al., 2020a)).

E.3. Attack Performance for Different Datasets and Target Models

The complete attack performance results for different datasets and target models are shown in Fig. 10. On complex datasets like ImageNet, the major challenge is the excessive number of categories (1,000 on ImageNet). Thus, we suspect that the geometry of model’s decision boundary is more non-smooth and complex, and therefore the general boundary attacks should be harder to improve.

The ‘successful attack’ is defined as the x_{adv} reaching some pre-defined distance threshold under the metric of MSE. Note that because the complexity of tasks and images varies between datasets, we set different MSE thresholds for the datasets. For example, ImageNet images are the most complicated so the task is most difficult, thus we set larger (looser) threshold for it. The corresponding numerical results for small query number constrains are shown in Table 9 and Table 10, the visualized attack success rates for different target models are shown in Fig. 11. Since in practice, we care about the efficiency more,

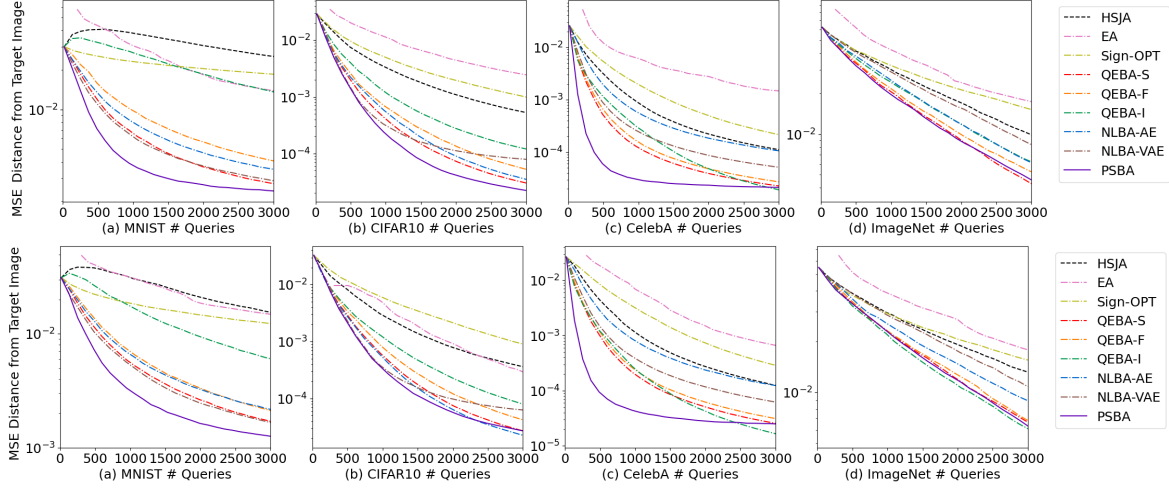


Figure 10. Perturbation magnitude (MSE) w.r.t. query numbers. Row 1: For attacks on ResNet-18; Row 2: For attacks on ResNeXt50_32 \times 4d.

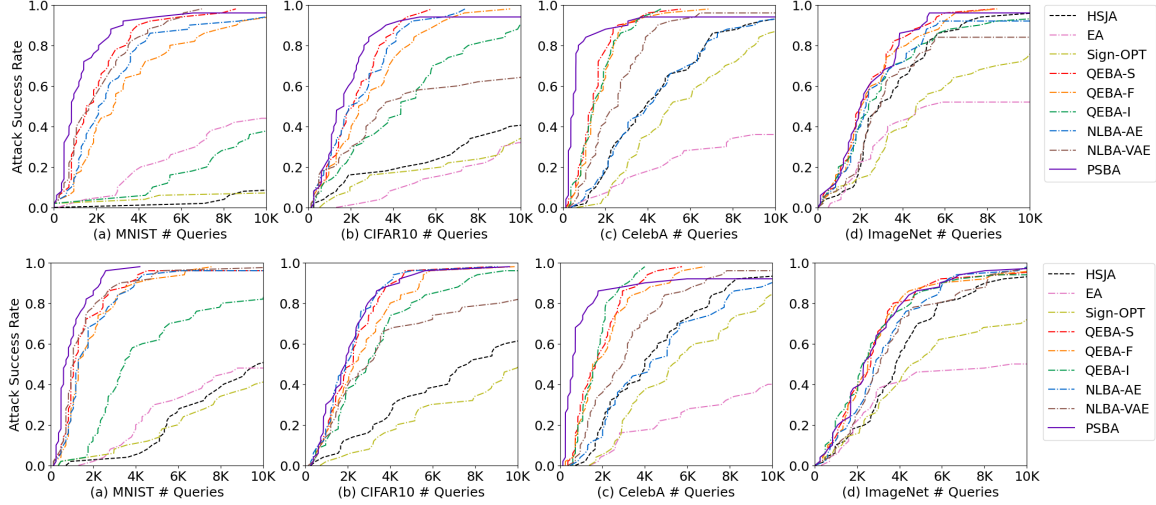


Figure 11. The attack success rate w.r.t. number of queries on four different datasets. Row 1: For attacks on ResNet-18; Row 2: For attacks on ResNeXt50_32 \times 4d.

Table 9. Comparison of the attack success rate for different attacks at query number 1K (the perturbation magnitude under MSE for each dataset are: MNIST: $5e - 3$; CIFAR10: $5e - 4$; CelebA: $1e - 4$; ImageNet: $1e - 2$).

Data	Model	# Queries = 1K								
		HSJA	EA	Sign-OPT	QEBA-S	QEBA-F	QEBA-I	NLBA-AE	NLBA-VAE	PSBA
MNIST	ResNet	2%	4%	4%	40%	18%	4%	26%	44%	64%
	ResNeXt	4%	0%	4%	44%	30%	4%	28%	50%	64%
CIFAR10	ResNet	16%	2%	14%	52%	42%	30%	50%	50%	62%
	ResNeXt	12%	0%	8%	44%	38%	30%	48%	52%	48%
CelebA	ResNet	8%	6%	2%	48%	36%	40%	10%	22%	86%
	ResNeXt	2%	0%	0%	32%	24%	22%	6%	12%	72%
ImageNet	ResNet	10%	8%	12%	22%	18%	22%	18%	10%	20%
	ResNeXt	12%	6%	10%	16%	14%	24%	14%	10%	20%

that is, we usually focus on the attack performance when the query number is small, like 1K or 2K. But we still provide the results for large query number constraints in Table 11, Table 12 and Table 13, showing that PSBA achieves the highest or comparable ASR to other approaches. Note that PSBA converges significantly faster than baselines ($\leq 3K$) (Fig.6 & 10 in paper), which leads to its high attack success rate with small number of queries. On the other hand, when large number of queries are allowed, baselines such as QEBA will eventually converge to similar result (e.g., close to 100% ASR), which

Table 10. Comparison of the attack success rate for different attacks at query number 3K (the perturbation magnitude under MSE for each dataset are: MNIST: $5e-3$; CIFAR10: $5e-4$; CelebA: $1e-4$; ImageNet: $1e-2$).

Data	Model	# Queries = 3K								
		HSJA	EA	Sign-OPT	QEBA-S	QEBA-F	QEBA-I	NLBA-AE	NLBA-VAE	PSBA
MNIST	ResNet	2%	12%	4%	80%	58%	6%	66%	76%	90%
	ResNeXt	4%	10%	10%	88%	80%	38%	82%	90%	98%
CIFAR10	ResNet	40%	34%	24%	96%	90%	74%	90%	96%	96%
	ResNeXt	50%	2%	30%	96%	90%	82%	96%	100%	96%
CelebA	ResNet	40%	16%	24%	92%	92%	88%	44%	68%	94%
	ResNeXt	38%	18%	24%	88%	78%	90%	40%	52%	90%
ImageNet	ResNet	54%	36%	30%	68%	66%	64%	64%	56%	68%
	ResNeXt	36%	38%	28%	68%	64%	64%	54%	48%	66%

 Table 11. Comparison of the attack success rate for different attacks at query number 5K (the perturbation magnitude under MSE for each dataset are: MNIST: $5e-3$; CIFAR10: $5e-4$; CelebA: $1e-4$; ImageNet: $1e-2$).

Data	Model	# Queries = 5K								
		HSJA	EA	Sign-OPT	QEBA-S	QEBA-F	QEBA-I	NLBA-AE	NLBA-VAE	PSBA
MNIST	ResNet	2%	24%	8%	94%	76%	12%	88%	90%	96%
	ResNeXt	12%	32%	14%	98%	94%	62%	96%	96%	100%
CIFAR10	ResNet	22%	12%	20%	96%	86%	54%	94%	58%	94%
	ResNeXt	36%	2%	22%	98%	86%	82%	96%	70%	94%
CelebA	ResNet	66%	24%	50%	98%	98%	100%	66%	92%	96%
	ResNeXt	62%	24%	42%	98%	90%	100%	54%	86%	92%
ImageNet	ResNet	74%	50%	54%	90%	86%	82%	84%	78%	92%
	ResNeXt	72%	48%	54%	88%	88%	86%	78%	80%	88%

 Table 12. Comparison of the attack success rate for different attacks at query number 8K (the perturbation magnitude under MSE for each dataset are: MNIST: $5e-3$; CIFAR10: $5e-4$; CelebA: $1e-4$; ImageNet: $1e-2$).

Data	Model	# Queries = 8K								
		HSJA	EA	Sign-OPT	QEBA-S	QEBA-F	QEBA-I	NLBA-AE	NLBA-VAE	PSBA
MNIST	ResNet	4%	40%	8%	98%	90%	30%	92%	100%	98%
	ResNeXt	40%	46%	36%	98%	100%	80%	98%	98%	100%
CIFAR10	ResNet	36%	22%	24%	100%	98%	82%	100%	64%	96%
	ResNeXt	54%	2%	36%	98%	98%	94%	98%	80%	98%
CelebA	ResNet	88%	36%	72%	100%	100%	100%	90%	98%	96%
	ResNeXt	90%	34%	72%	100%	100%	100%	86%	98%	94%
ImageNet	ResNet	96%	54%	70%	98%	98%	92%	94%	86%	98%
	ResNeXt	90%	48%	70%	94%	92%	94%	96%	88%	96%

again demonstrates the importance of evaluation under small query budget.

E.4. Comparison with RayS Attack

RayS attack (Chen & Gu, 2020) performs blackbox attack by enumerating gradient signs at different scales, which is an efficient attack strategy for untargeted attack under ℓ_∞ norm. While PSBA can perform both untargeted and targeted attacks, the gradient generator used in our experiments is mainly designed for the targeted attack under MSE measure, which is a more practical and tougher task. To customize our PSBA for ℓ_∞ norm bounded attack scenario, we believe some specific design for the generator is needed. But currently, even if we directly use the original PGAN generator, our method can still compete with the RayS attack when compared under the ℓ_∞ based untargeted attack scenario. The corresponding additional experiments conducted on ImageNet dataset are shown in Table 14, demonstrating that the PSBA always outperforms RayS in targeted attacks, while RayS achieves slightly better results for untargeted attack under ℓ_∞ .

Table 13. Comparison of the attack success rate for different attacks at query number 10K (the perturbation magnitude under MSE for each dataset are: MNIST: $5e-3$; CIFAR10: $5e-4$; CelebA: $1e-4$; ImageNet: $1e-2$).

Data	Model	# Queries = 10K								
		HSJA	EA	Sign-OPT	QEBA-S	QEBA-F	QEBA-I	NLBA-AE	NLBA-VAE	PSBA
MNIST	ResNet	10%	46%	8%	100%	94%	38%	96%	100%	98%
	ResNeXt	52%	50%	42%	98%	100%	84%	98%	98%	100%
CIFAR10	ResNet	42%	34%	36%	100%	100%	92%	100%	66%	96%
	ResNeXt	62%	2%	50%	100%	100%	98%	100%	82%	100%
CelebA	ResNet	94%	38%	88%	100%	100%	100%	94%	98%	96%
	ResNeXt	94%	42%	86%	100%	100%	100%	92%	98%	94%
ImageNet	ResNet	96%	54%	76%	100%	100%	94%	94%	86%	98%
	ResNeXt	94%	52%	72%	96%	96%	96%	98%	98%	98%

Table 14. Comparison of Attack Success Rate (ASR) on 100 randomly chosen ImageNet images for ResNet-18 with different perturbation thresholds ϵ and attack types (the query budget = 10000).

Attack Type	ϵ	Methods	Avg. Queries	Med. Queries	ASR (%)
Targeted Attack	0.30 (ℓ_∞)	HSJA	1909.9	853.0	45
		RayS	4677.0	4677.0	2
		PSBA	1437.7	502.0	96
	0.01 (MSE)	HSJA	3182.8	2726.0	99
		RayS	2479.0	2479.0	2
		PSBA	2460.4	1924.0	99
Untargeted Attack	0.05 (ℓ_∞)	HSJA	1782.8	595.5	88
		RayS	528.7	214.5	100
		PSBA	596.9	270.0	99
	0.0001 (MSE)	HSJA	2208.4	1305.0	92
		RayS	1798.1	625.0	83
		PSBA	1151.5	486.0	96

Since the RayS in targeted setting is not mentioned in the original paper, we have tried two ways to implement it: 1) initialize the perturbation using the same setting as that in untargeted attack; 2) initialize the perturbation using the images from the target class. The values recorded in the table are the better ones between these two ways and there may still exist a better way to do it. The other thing to note is that currently all the methods are not so powerful on ImageNet for targeted attack with the perturbation threshold ϵ set to 0.05 under ℓ_∞ norm.

E.5. Cosine Similarity Measure for Offline Models

The cosine similarity between the estimated gradient and the true gradient is a significant measure of the quality of the gradient estimation, and is highly correlated with the actual attack performance. The cosine similarity for the different boundary attack methods are shown in Fig. 12. As we can see, our approach PSBA-PGAN usually achieves higher cosine similarity especially when the number of queries is limited.

E.6. Long Tail Distribution for the Gradients Generated from Different Models on Frequency Domain

As mentioned in the Section 5.2, the gradients generated by the target model ResNet-18 tend to focus on the low-frequency region. However, this pattern actually exists on other models as well and the experiments conducted here are in a more statistical sense: first, gradients from 1,000 images are generated from these six models on different datasets respectively; then, by transforming them into frequency domain by DCT transformation, we average the absolute value of the coefficients on the corresponding basis components and smooth them by the Savitzky-Golay filter. As a result, if we draw these components from low-frequency to high-frequency on x -axis, we will see the interesting long tail distribution as shown in the Fig. 13. This extensively existed phenomenon, as justified in Section 4.2, indicates that the attack performance would be

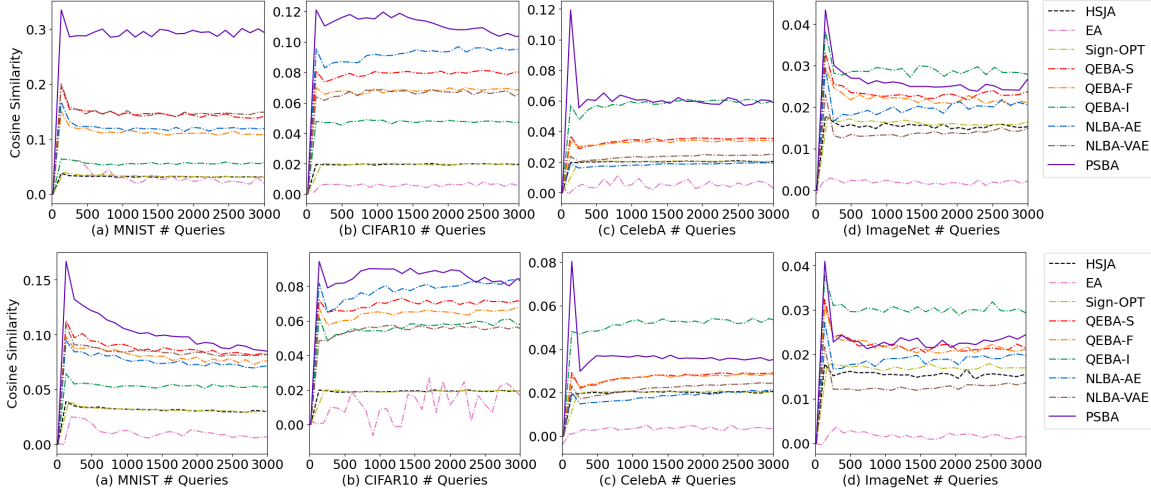


Figure 12. The cosine similarity between the estimated and true gradient w.r.t. the number of queries during attacking models on different datasets. Row 1: For attacks on ResNet-18; Row 2: For attacks on ResNeXt50_32x4d.

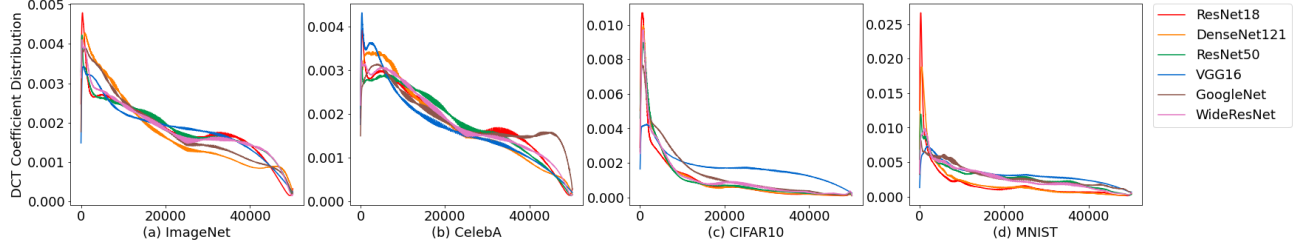


Figure 13. The long-tailed distribution for the coefficients of the gradients represented on DCT basis on different models and datasets.

improved if we just save the low-frequency part of the generated gradient images. This conjecture has already been proved by our experiments in Appendix E.8.

E.7. High Sensitivity on Gradient Direction

Hereinafter, the target model is specified to ResNet-18 for reducing the redundancy. The tendency on ResNeXt models or other models is the same, that is, the results shown below are actually decoupled with the structure of the target model.

Verification of High Sensitivity. We empirically verify that the trained PGAN has higher sensitivity on the projected true gradient as discussed in Section 5.2. The gradient estimator chosen here is the PGAN generator with the optimal scale 28×28 for each dataset. Inspired by the definition in Lemma 4.1, the value α_1^2 is approximately calculated by $\frac{1}{B} \sum_{b=1}^B \cos^2 \langle \Delta \mathbf{f}(\delta_t u_b), \text{proj}_{\nabla \mathbf{f}(0)} \nabla S(x_t) \rangle$, where the number of queries, i.e., B , is set to 10,000 instead of the original 100 for better estimation and verification. The value $\frac{\sum_{i=2}^m \alpha_i^2}{m-1}$ is then approximately calculated by $\frac{1}{B(m-1)} \sum_{b=1}^B (1 - \cos^2 \langle \Delta \mathbf{f}(\delta_t u_b), \text{proj}_{\nabla \mathbf{f}(0)} \nabla S(x_t) \rangle)$. Since the actual output scale of \mathbf{f} is 28×28 here, the ground gradient $\nabla S(x_t)$ is resized to 28×28 first (thus denoted by $\text{proj}_{\nabla \mathbf{f}(0)} \nabla S(x_t)$) and the value m is equal to $n_{\text{channel}} \times 28 \times 28$ here. All these values are averaged on 50 pairs of source-target images with 10-step attack on ResNet-18.

As shown in Fig. 14, across all four datasets, we observe that the sensitivity on the projected true gradient direction (blue bars) is significantly higher than the (averaged) sensitivity on other orthogonal directions (purple bars).

Adjust Sensitivity on Different Directions. Here, we deliberately adjust the sensitivity on different directions to show the correlation between the attack performance and sensitivity by changing the weight of the components which are orthogonal to the ground gradient. In other words, we replace the $\Delta \mathbf{f}(\delta_t u_b)$ in the original calculation of estimated gradient $\widehat{\nabla S}(x_t)$ with $\left(\frac{\langle \Delta \mathbf{f}(\delta_t u_b), \nabla S(x_t) \rangle}{\|\nabla S(x_t)\|} \nabla S(x_t) + k \left(\Delta \mathbf{f}(\delta_t u_b) - \frac{\langle \Delta \mathbf{f}(\delta_t u_b), \nabla S(x_t) \rangle}{\|\nabla S(x_t)\|} \nabla S(x_t) \right) \right)$ and then repeat the attack on the target model. Lower value of k means less weight is put on the orthogonal components. Empirically, the range of k is set between 0.96 to 1.04 and it is worth noting that when the value of k is set to 1, the new gradient estimation adopted here is

just the same with the original gradient estimation. We choose the projection ‘PGAN28’ and dataset ImageNet. As shown in Fig. 15, aligned with our theoretical analysis, lower k results in better attack performance, and vice versa.

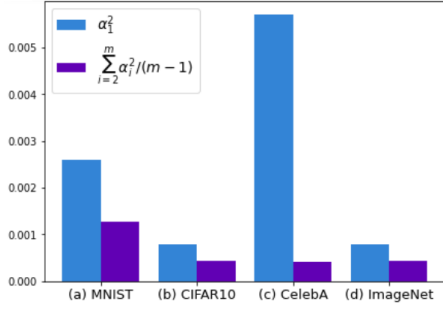


Figure 14. The α value on diverse datasets.

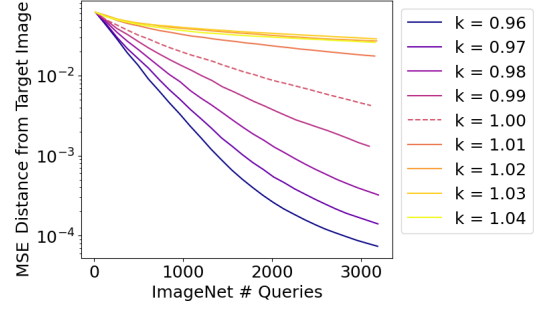


Figure 15. The perturbation magnitude w.r.t. different number of queries for different k values on ImageNet.

E.8. PSBA with Different Domains

In this subsection, we demonstrate the performance of PSBA when applied to other domains like frequency and spectrum. Since the PGAN is originally designed for spatial expansion, it would be also beneficial for us to adopt some similar training strategy to expand progressively on both frequency and spectrum domain. However, for both convenience and effectiveness, we just take PGAN224, whose attack performance is almost the worst compared to other PGAN with smaller scale, as the gradient generator in the experiments here. As a result, the attack performance on these other domains can be further improved by progressively expanding training strategy.

With this in mind, in this subsection, the main attention is concentrated on: 1) the existence of the optimal scale on both frequency and spectrum domain. 2) whether the original attack performance of PGAN224 would be improved a lot by just selecting the optimal scale on specific frequency or spectrum domain. Since the conclusions are consistent with any model, we just show the experiment results on ResNet-18 below as an instance.

Frequency Domain. As discussed in Appendix E.6, with applying the DCT transformation on the output of PGAN in 224×224 scale, the low-frequency components will be concentrated at the upper left corner, i.e., low-frequency subspace. Then, we let ‘PGAN224dk’ denote the adjusted attack process where we just save the $k \times k$ signals on the upper left corner of the frequency representation of the output of PGAN224 and transform it back to the original space by the Inverse DCT to continue the attack. In other words, we just use some low-frequency part of the original gradient images generated from PGAN224 to estimate the ground gradient and the pseudocode is also provided in Algorithm 2 for making it more clear. The final attack performance is shown in Fig. 16, and as we can see, in some cases like when the src-tgt images are sampled from MNIST, PSBA-freq even outperforms all other baselines with a simple adjustment on the output of the inherent bad gradient estimator PGAN224. The results corresponding to different choices of frequency region and their induced changes of cosine similarity are shown in Fig. 17 and Fig. 18. Besides, this simple strategy can also work well on the attack to the online API, which is shown in Fig. 19 and Fig. 20.

As we can see, even this simple ‘gating’ strategy can improve the attack performance a lot compared with original PGAN224. Though it is not as competitive as the progressive scaling in the spatial domain due to lack of projection model finetuning. Furthermore, the existence of optimal scale is pronounced.

Spectrum Domain. Here, we sample 40,000 gradient images generated from PGAN224, and then use PCA to decompose them to get 9,408 main components. It may seem to be great if we project the original gradient images generated from PGAN224 to just part of the main components, however, the computation cost is a little unacceptable, since there are a lot of dot product operations between two 150,000-dimensional vectors required. Therefore, for efficiency, the gradient images generated here are actually composed by the combination of the top- k main components among the total 9,408 components with the coefficients sampled from normal distribution. Thus, for simplicity, we denote ‘PGAN224pk’ as the attack with the combination of the top- k main components decomposed by PCA. By progressively increase the value of k , the attack performance are shown in Fig. 21. The result on different spectrum scales and corresponding changes of cosine similarity

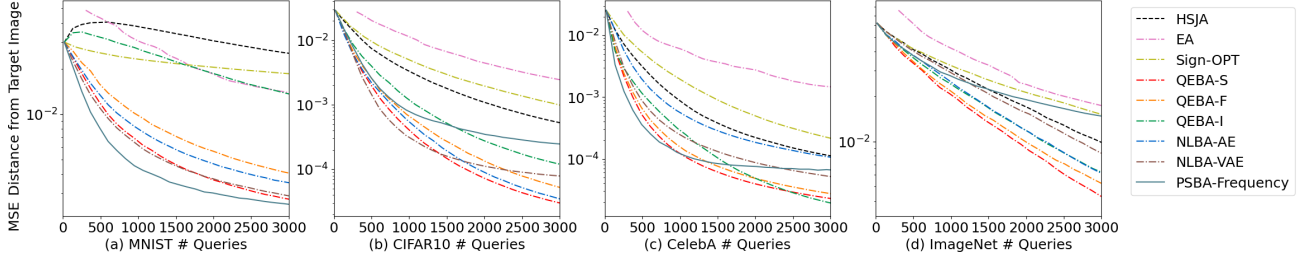


Figure 16. The perturbation magnitude w.r.t. different number of queries for different methods. The PSBA here is applied on frequency domain.

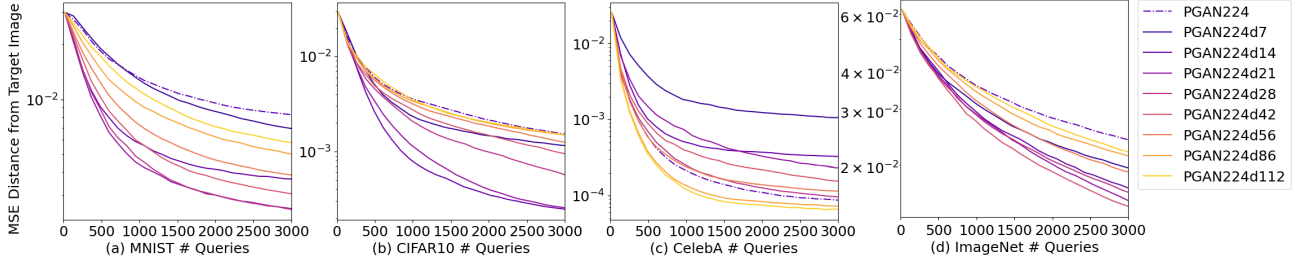


Figure 17. The perturbation magnitude w.r.t. different number of queries for different scales chosen on frequency domain.

are shown in Fig. 22 and Fig. 23. Again, we observe an apparent improvement over the original PGAN224 and the existence of the optimal scale.

E.9. Optimal Scale across Different Model Structures

One may think that the optimal scale may be influenced a lot by the specific structure of the target model. In other words, the depth of the model, the existence of the residual connection and batchnorm layer, and so on, would affect the optimal scale. However, the result as shown in Table 15 demonstrates that the optimal scale is actually stable, which is usually the small scale 28×28 .

It is our future work to look into this phenomenon and analyze the optimal properties such as stability of optimal scale. Besides, together with the improved attack performance owing to the removing of the high frequency part or the focus on the most informative spectrum of the generated images of PGAN224, it will be promising to explore the benefits brought from gradient sparsification and devise a more efficient algorithm in the future.

F. Qualitative Results

In this section, we present the qualitative results for attacking both offline models and online APIs.

F.1. Offline Models

The goal of the attack is to generate an adversarial image that looks like the target image but has the same label with source image. We report qualitative results that show how the adversarial image changes during the attack process in Figure 24, Figure 25, Figure 26, and Figure 27 for the four datasets respectively. The target model chosen here is ResNet-18. In the figures, the left-most column has two images: the source image and the target image. They are randomly sampled from the corresponding dataset. We make sure that the images in the sampled pairs have different ground truth labels (otherwise the attack is trivial). The other five columns each represents the adversarial image at certain number of queries as indicated by $\#q$ at the bottom line. In other words, all images in these five columns can successfully attack the target model. Each row represents one method as shown on the right. The d value under each image shows the MSE between the adversarial image and the target image. The smaller the d is, the better the attack is.

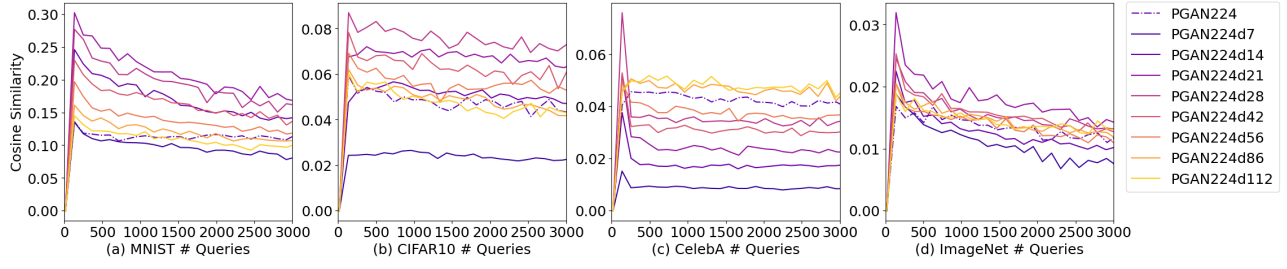


Figure 18. The cosine similarity between the estimated and true gradients for different scales chosen on frequency domain.

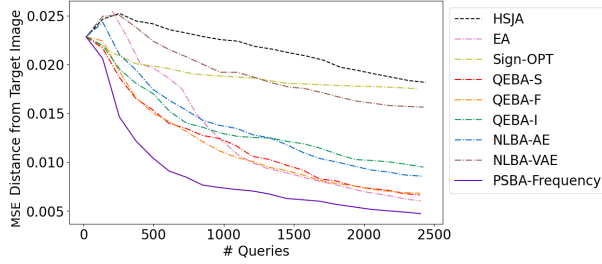


Figure 19. The perturbation magnitude w.r.t. different queries against Face++ ‘Compare’ API, the PSBA here is applied on frequency domain.

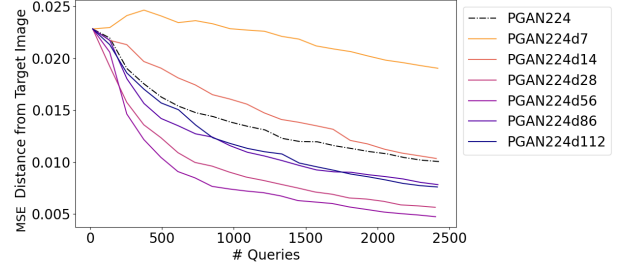


Figure 20. The perturbation magnitude w.r.t. different number of queries for different scales chosen on frequency domain against Face++ ‘Compare’ API.

F.2. Commercial Online API Attack

As discussed in Section 5, the goal is to generate an adversarial image that looks like the target image but is predicted as ‘same person’ with the source image. In this case, we want to get images that looks like the man but is actually identified as the woman. The qualitative results of attacking the online API Face++ ‘compare’ is shown in Figure 28. In the figure, the source image and target image are shown on the left-most column.

Table 15. The optimal scale across different model structures.

Model \ Dataset	MNIST	CIFAR-10	CelebA	Imagenet
ResNet-18	28×28	28×28	28×28	28×28
ResNet-34	28×28	28×28	28×28	56×56
ResNet-152	28×28	28×28	56×56	56×56
ResNext50_32x4d	28×28	28×28	28×28	56×56
Vgg11	28×28	28×28	28×28	56×56
Vgg19	28×28	28×28	28×28	56×56
Vgg11_bn	112×112	28×28	28×28	56×56
Vgg19_bn	112×112	28×28	28×28	56×56
DenseNet161	28×28	14×14	28×28	56×56

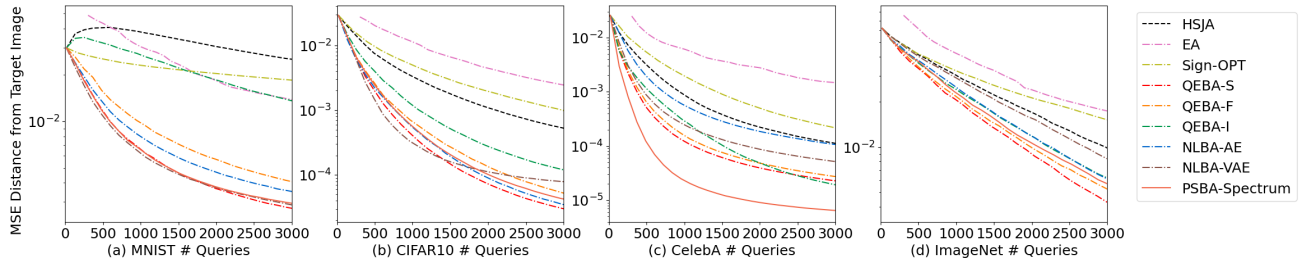


Figure 21. The perturbation magnitude w.r.t. different number of queries for different scales chosen on spectrum domain.

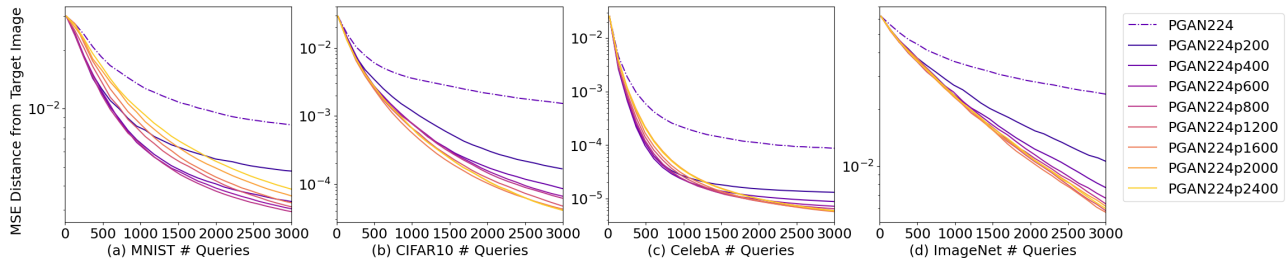


Figure 22. The perturbation magnitude w.r.t. different number of queries for different methods, the PSBA here is applied on spectrum domain.

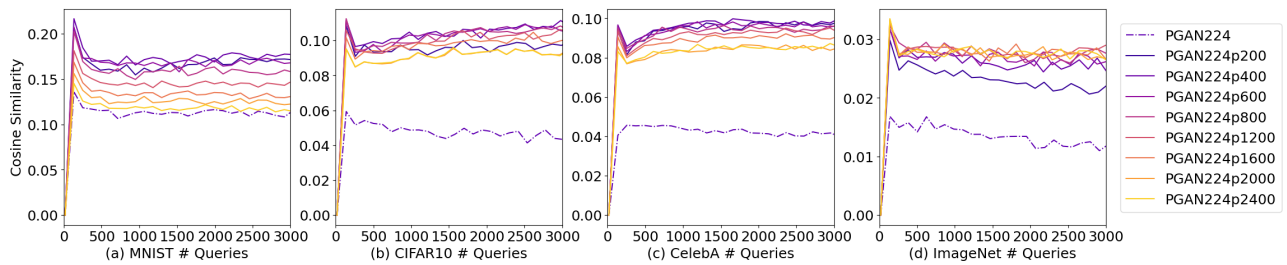


Figure 23. The cosine similarity between the estimated and true gradients for different scales chosen on spectrum domain.

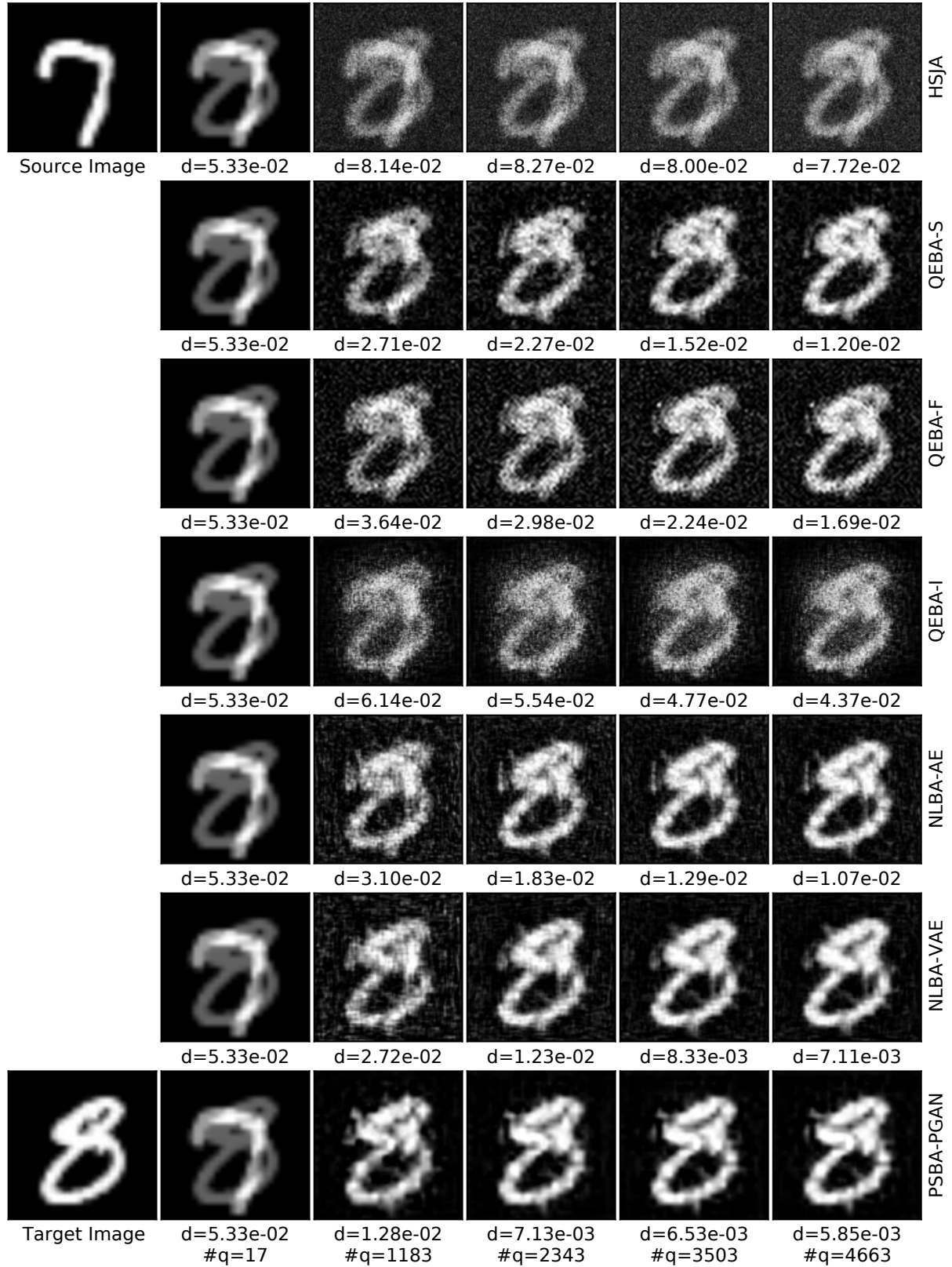


Figure 24. The qualitative case study of attacking ResNet-18 model on MNIST dataset.



Figure 25. The qualitative case study of attacking ResNet-18 model on CIFAR-10 dataset.

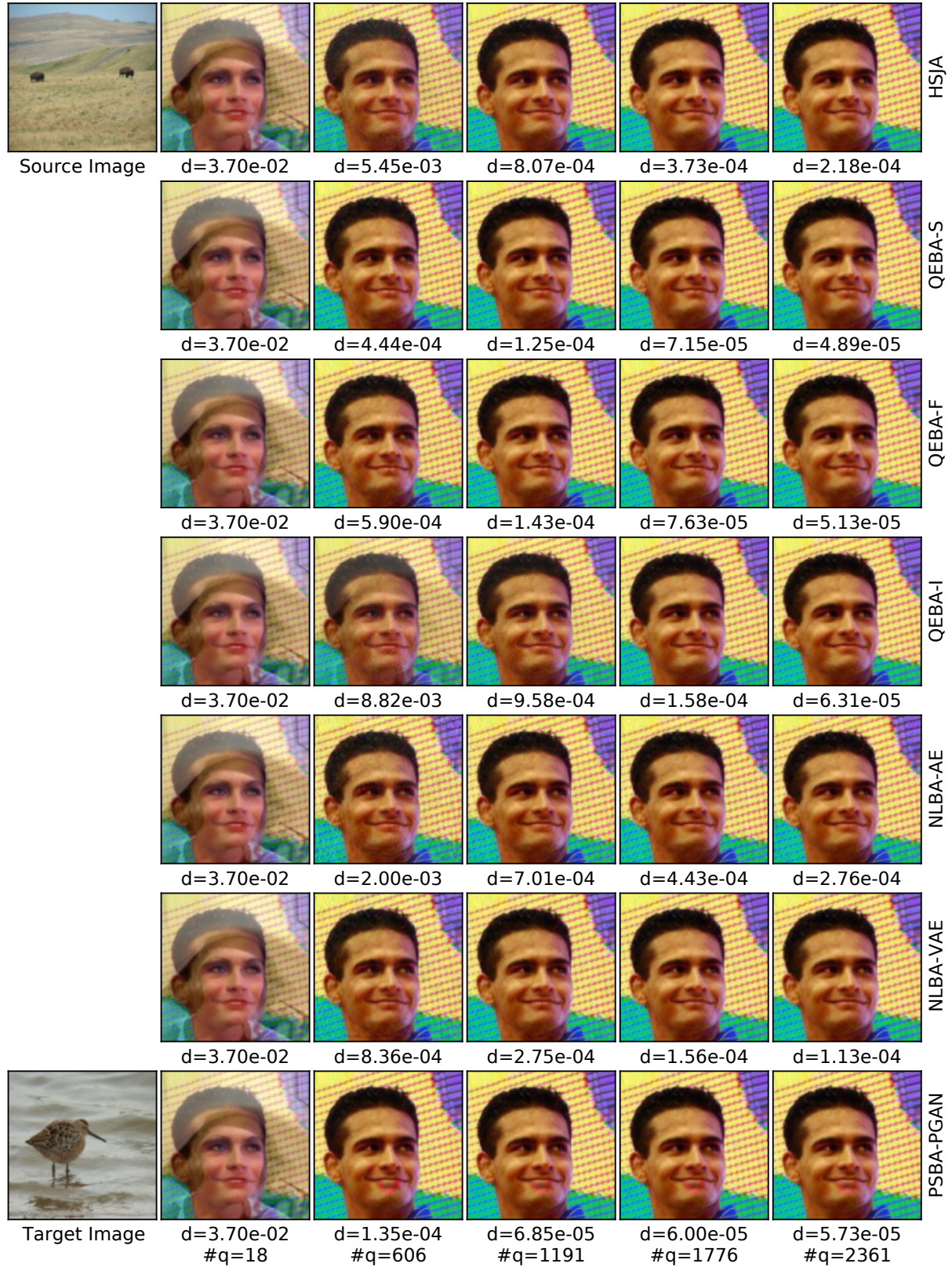


Figure 26. The qualitative case study of attacking ResNet-18 model on CelebA dataset.

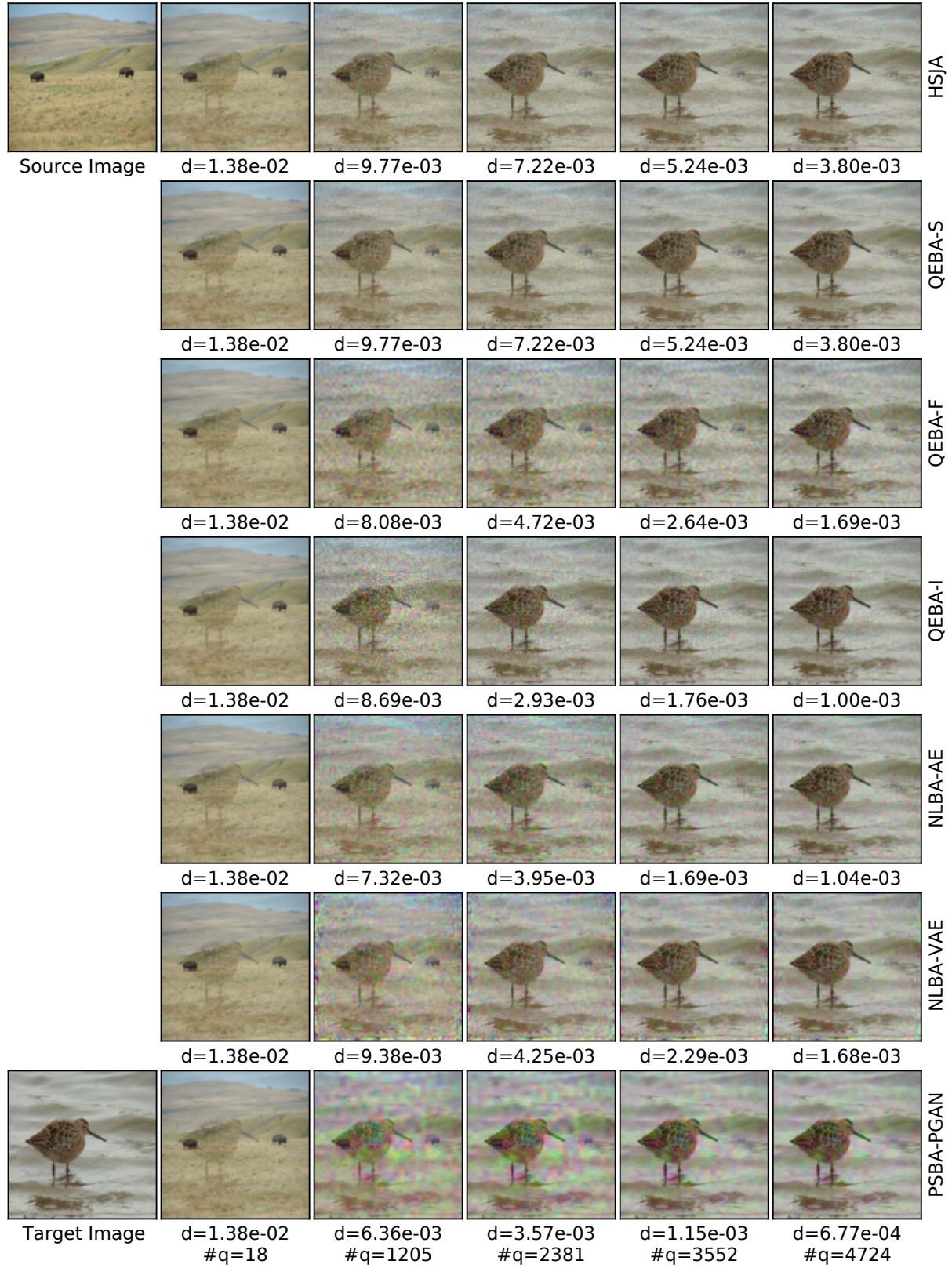


Figure 27. The qualitative case study of attacking ResNet-18 model on ImageNet dataset.

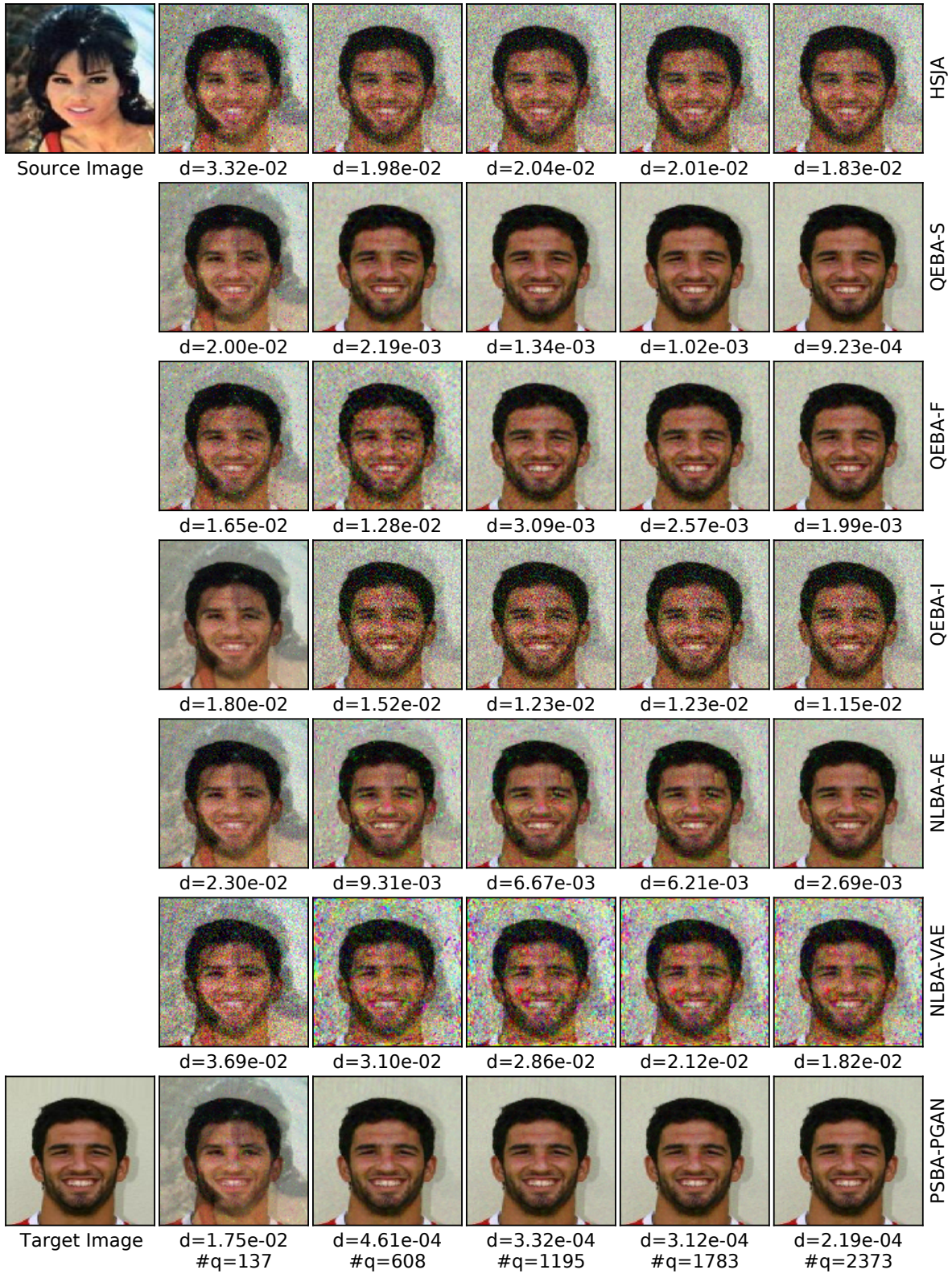


Figure 28. A case study of Face++ online API attack process. The source-target image pair is randomly sampled from CelebA dataset (ID: 019862 and 168859).